Multiple Ionization of Heavy Atoms in Super Strong Laser Fields

vorgelegt von
Dottoressa
Elena Gubbini
aus Brescia (Italien)

von der Fakultät II - Mathematik und Naturwissenschaften
der Technischen Universität Berlin
zur Erlangung des akademischen Grades

Doktorin der Naturwissenschaften
- Dr. rer. nat. -

genehmigte Dissertation

Berlin 2005
D 83

Promotionsausschuss:

Vorsitzender:	Prof. Dr. E. Sedelmayr
Berichter:	Prof. Dr. W. Sandner
Berichter:	Prof. Dr. G. Von Oppen

Tag der wissenschaftlichen Aussprache: 20.07.2005

Abstract

In this work we have presented experimental investigations on ionization dynamics for heavy atom species (Kr and Xe) exposed to super strong laser fields generated by the Ti:Sapph laser system of the Max-Born Institute. We have focused our interest on the analysis of the intensity dependent ion yields for highly charged states. In particular, the d-subshell ionization of krypton and xenon has been investigated in linearly and circularly polarized light. The experimental results have been discussed within several theoretical models. The first goal of this work was the understanding of the dominant ionization mechanisms in the intensity regime between 10^{16} and 10^{18} W/cm^2, where the highly charged states are produced. We have examined the applicability of the ADK theory, which describes the single-electron ionization process at nonrelativistic intensities, also for highly charged states. We have discussed the experimental observations by means of the semiclassical approach for the nonsequential ionization, also taking into account the influence of the relativistic effects on multiple ionization. We have shown that for the highly charged states the process proceeds purely sequentially. The ADK ionization rates strongly depend on the magnetic quantum number of the active electron. The main goal of this work is to investigate experimentally whether the initial state of the active electron influences the sequential ionization process. We have concluded that the ionic core fully relax before the next ionization sets in. Any memory of the initial magnetic quantum number is erased during ionization via a fast m-sub state-mixing process. Experiments with attosecond laser pulses, where ionization of several electrons is expected to occur within one cycle, could deliver further informations on the effective time scale at which core relaxation actually takes place. We were also interested in the measurement of intensities larger than 10^{18} W/cm^2 for which the normal procedure through the measurement of energy, pulse width and focus waist fails. In the frame of this work, the possibility to use the ionization dynamics as intensity probe has been discussed. Two methods are described, based on over-the-barrier ionization (OBI) and on the ADK theory respectively. A comparison between the results obtained by applying the two methods to our experiment has shown that the method based on the threshold intensity for over-the-barrier ionization is applicable for a coarse approximation of the peak intensity, while the ADK theory releases a good method for a determination of the relative laser intensity.

Introduction

New physics readily follows new techniques. An important milestone in atomic physics was reached with the application of the chirped-pulse amplification (CPA) to lasers [1]. This technique, which limits peak intensities during the amplification process, was already used for microwave devices and has permitted laser peak powers to increase by more than three orders of magnitude, practically overnight. In the last few years, systems which can deliver peak intensities of 10^{16} W/cm^2 at a high repetition rate (kHz) became a standard spectroscopic tool in several laboratories. The field strengths achieved by these new laser systems are competing with the atomic Coulomb forces controlling the electron dynamics, thus, opening up a fundamentally new dynamic domain in atomic and molecular physics. For the interaction of matter with such high peak power laser pulses [2, 3], new phenomena were observed that could not be described within a quantum mechanical perturbation theory. A typical example is above threshold ionization (ATI) [4, 5] where ejected electrons absorb more photons than required for ionization.

At low laser frequencies, such as for CO_2 lasers, it was found that the picture used to describe the multiphoton process was not applicable in the regime of field strengths comparable to the Coloumb field that binds the electron ($I > 10^{14}$ W/cm^2). Thus, a new approach to shed light on the ionization dynamics in this regime became necessary. The model of a quasistatic tunneling proposed by Keldysh [6] in 1965, which remained purely academic for more than two decades, could be used to interpret the atomic ionization behavior in such strong laser fields. Therein, the bound electron tunnels through the effective potential barrier composed of the atomic and the instantaneous potential of the electric field. A factor γ, called the Keldysh parameter, was introduced to define the transition between the two different ionization pictures with dependence on the laser field parameters, (in a.u., $\gamma = \omega\sqrt{2E_b}/F_0$ where E_b is the binding energy of the electron, ω and F_0 are

the frequency and the strength of the laser field respectively). If γ is higher than unity, the multiphoton process takes place. For $\gamma \ll 1$, tunneling dominates.

Today, the ionization dynamics in the laser intensity regime between 10^{14} W/cm^2 and 10^{16} W/cm^2 are well understood: the single electron ionization process can be described with a formula derived by Ammosov, Delone and Krainov (so called ADK theory) for tunnel ionization of complex atoms in an alternating electric field [7]. In this picture, multiple ionization occurs sequentially, i.e., each electron is released into the continuum by the interaction of the ionic core with the laser field. However, a strong enhancement of doubly and multiply charged ion yields, measured below the saturation intensity of single ionization [8, 9, 10, 11], has given an indication of the presence of a nonsequential ionization process which dominates the sequential one. A rescattering model [12] provides an intuitive qualitative picture of the underlying mechanism: the first electron, set free by tunnel ionization, returns to the core under the influence of the external laser electric field and collisionally dislodges a second bound electron.

Recently, a broad interest moved to the study of the atomic ionization dynamics at laser intensities between 10^{16} and 10^{18} W/cm^2. Here, the involved electron velocity during ionization process approachs the speed of light. Since $v \sim c$ at intensities higher than 2×10^{18} W/cm^2, we define this intensity regime a "quasi"-relativistic regime. A different behavior starts to appear in the dynamics of the atoms subjected to these super-high intensity pulses. For example, it is expected that the role of the rescattering mechanism for the ionization process is largely diminished for highly charged ions [13]. The first direct evidences of the suppression of nonsequential ionization were provided a few years ago [14].

So far, few experimental investigations have been performed in this super-high intensity region [13, 14, 15, 16]. Most topics related with the ionization processes of highly charged states inherent with this super-high intensity regime still need to be explored. One question concerns the applicability of the tunnelling ionization rates proposed by the ADK theory to the highly charged states. A further question is related to the production of highly charged states where the inner subshells of a multi-electron system is envolved. Here, several electrons have the same n and l but different m quantum numbers. Several questions arise immediately: is the ionization so fast that electrons remain in their initial state while they are sequentially stripped out of the core? Or do they have time to couple? If this is the case, how

does coupling influence the ionization?

In this thesis, a new contribution to the understanding of the mechanisms under the ionization dynamics in the "quasi"-relativistic regime is given. In particular we are concentrating the experimental investigation on the dynamics for heavy atomic species (Kr and Xe). Heavy atoms exposed to very strong laser fields can be ionized to charged states as high as $Z = 26$ depending on the particular binding energies of the elements under study. The electrons involved in ionization belong to inner shells that were never influenced at lower intensities before. This opens new interesting directions of research. We also aim to give an answer whether the initial state of the electrons in a complex system influences the sequential ionization process.

The thesis is organized as follows, in the first section (chapter 1 and 2), a detailed overview of the state of the art of ionization dynamics at intensities below and above 10^{16} W/cm^2 is given.

A short description of the laser and the experimental systems used for our research follows in chapter 3 and 4 respectively. In the frame of this work, an "on-line" system to clean the laser optics has been developed, as well. Because of the high intensity carried by the laser beam, on the optics surface it can happen that carbon is deposited on place of the laser beam. The cleaning system prevents any contamination and avoids time-consuming realignment of the optics.

In chapter 5, firstly we verify that sequential ionization is the dominant ionization process for highly charged states by presenting the ion yields measurements for krypton ions with $7 < Z < 11$ as a function of laser intensity. Thereafter, several effects which contribute to the suppression of nonsequential ionization are analysed by means of the semiclassical approach to the rescattering mechanism. The last section of chapter 5 is dedicated to the study of the response of $d-$shell electrons to short laser pulses. The intensity dependence of the ion yields with different charge states which correspond to the ionization of the electrons in the d-shell gives a direct information whether, on time scale, ionization is faster than a core relaxation process. The discussion is conducted on the basis of two theoretical models which give rise to a strong difference in the relative behavior of the different ion yield curves. The ion yields calculated by using ionization rates averaged over all the m substates is found to be in good agreement with the experimental data, giving a hint that the core fully relaxes between two ionization steps via a m-mixing. Two possible causes which lead to m-mixing are also proposed: the electron-electron correlation and the interplay of the orthogonal electric

and magnetic field components.

The study of ionization processes in ultra strong laser fields is not only important for the understanding of the fundamentals of atomic dynamics. It could also find an application as an instrument for laser diagnostic. In the last chapter of this work, we discussed the possibility to apply the atomic ionization dynamics to the diagnostic of TW lasers, for which standards pulse diagnostic technology does not apply since the instruments would not survive the extremely high intensity carried by such systems.

Contents

Chapter 1

Single Electron Ionization

This chapter is dedicated to an overview of the single electron ionization processes occurring in atoms subjected to intense laser fields. After a review of the different processes, particular attention will be given to the description of tunneling ionization.

1.1 Photoionization

Single photon ionization

It is known since Einstein that an atom can be photoionized by absorbing a single photon whose energy $\hbar\omega$ is higher than the binding energy E_b of the electron in the atom (see figure 1.1).

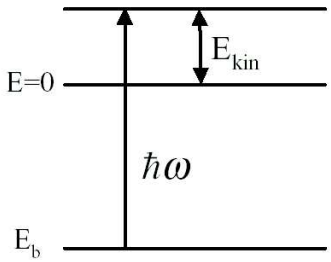

Figure 1.1: Single photon ionization. The atom ionizes through absorption of one photon whose energy $\hbar\omega$ is larger than the binding energy E_b of the active electron.

The kinetic energy that the electron acquires in the continuum is

$$E_{kin} = \hbar\omega - E_b \tag{1.1}$$

The atom responds linearly to the weak intensity radiation.

Multiphoton ionization

If $\hbar\omega < E_b$, more photons are necessary for ionization.

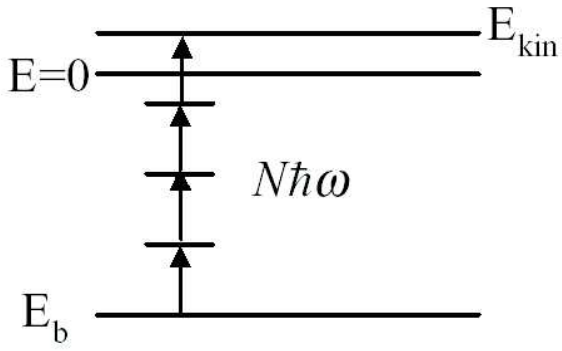

Figure 1.2: Schematic diagram of multiphoton ionization process. The atom is ionized through absorption of N photons whose energy $\hbar\omega$ is smaller than the binding energy $\geq E_b$ of the electron.

In multiphoton ionization (MPI), the atom "sees" the laser as a flow of N photons with energy $\hbar\omega$. The electron can reach the continuum via multiple photon absorption, only if the absorbed energy is higher than its binding energy (see figure 1.2).

The resulting kinetic energy of the electron is now given by

$$E_{kin} = N\hbar\omega - E_b. \tag{1.2}$$

MPI has first been discussed in the PhD thesis of Maria Goppert Maier, a student of Max Born. It can be accurately modelled by lowest-order perturbation theory [17, 18]. This picture, in fact, is valid as long as the electric field strength is much smaller than the atomic electric field ($F_0 \ll F_a$). Such a condition allows the treatment of the external potential as a small perturbation of the Coulomb potential so that it is possible to solve the Schrödinger

equation using the perturbation theory. The ionization rate for N photons absorption is then given by

$$\Gamma_N = \sigma_N I^N, \tag{1.3}$$

where σ_N is the generalized cross section and I the intensity of the incident light.

Above threshold ionization

In 1979, in an experiment on six-photon ionization of xenon, Agostini et al. [19] have shown an electron energy spectrum that could not be completely explained by applying equation (1.2). They have investigated the ionization of xenon atoms (E_b = 12.27 eV) with a frequency doubled Nd-glass laser ($\hbar\omega$ = 2.34 eV). The obtained energy spectrum has shown a first peak at an energy of 2 eV which corresponds to the kinetic energy of an electron emitted with six-photons ionization and a second additional peak, separated by a photon energy from the first one. This phenomenon could be explained with the assumption that the number of the absorbed photons is higher than the required number N to have ionization (see figure 1.3). The process was called Above Threshold Ionization (ATI) [20].

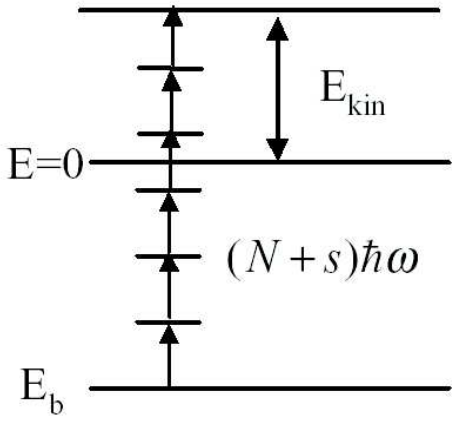

Figure 1.3: Photoionization picture. The atom is ionized through absorption of n photons with energy $\hbar\omega$.

For moderate intensities, the ATI process can be properly described by low-order perturbation theory. In this case the ionization rate formula (1.3) and the photoelectrons kinetic energy formula (1.2) generalize respectively to

$$\Gamma_N \propto I^{N+s} \tag{1.4}$$

and

$$E_{kin} = (N+s)\hbar\omega - E_b. \tag{1.5}$$

Further experimental investigations have shown that at higher field strengths the measured energy spectra no longer behaves in a perturbative way. As visible in figure 1.4a), with an increase of the intensity, the first peak disappears while the peaks corresponding to the absorption of a higher number of photons becomes more probable and do not follow the power law (1.4) anymore. In a strong field, the binding energy increases by a quantity U_p.

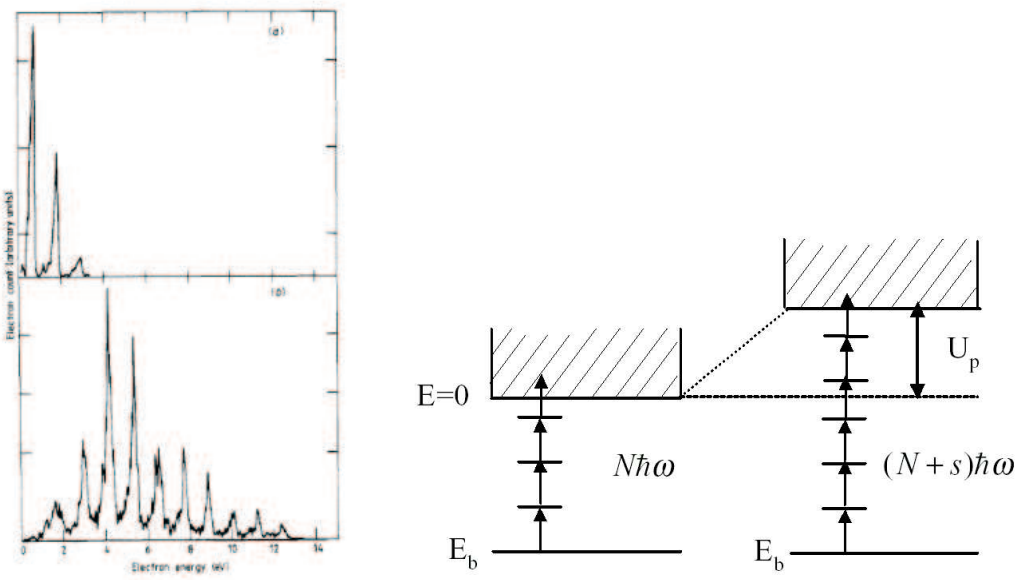

Figure 1.4: On the left side, the photoelectron energy spectra measured for xenon irradiated by a picosecond laser pulse [5]. On the right, the shift of the ionization potential due to the ponderomotive component in the electron kinetic energy.

The physical interpretation is that the atom ground state is hardly shifted while the Rydberg states and the ionization limit are shifted up by U_p. The

reason for such behavior lies in the fact that a free electron in an electric field gains a cycle-averaged kinetic energy due to the oscillation of the field in addition to a translational kinetic energy. This quiver energy, also called Ponderomotive energy U_p, is defined as

$$U_p(eV) = \frac{q^2 F_0^2}{4m\omega^2} = 9.33 \times 10^{-14} I(W/cm^2)\lambda^2(\mu m). \tag{1.6}$$

The ponderomotive energy has to be supplied by the photons or, alternatively one can say that there is an increase of the ionization potential of the atom, as shown in figure 1.4b).

This means that the ionization can happen only with a higher number of photon than usually necessary. In such a case, the electron will acquire a kinetic energy given by

$$E_{kin} = (N + s)\hbar\omega - (E_b + U_p). \tag{1.7}$$

However, it can recover the full kinetic energy (1.5) only when the pulse duration of the field is long enough to allow the electron to leave the focus (generally about 10 ps). In this case, due to spatial inhomogeneity of the laser beam, the electron experiences the conservative force $-\nabla U_p$ which accelerates it until it gains U_p. In contrast, if the pulse has a subpicosecond duration, the electron does not have time to be accelerated and its final kinetic energy is given by eq. (1.7).

1.2 Tunneling Ionization

Let us now consider the case when the external potential becomes so strong that it cannot be considered as a perturbation of the Coulomb potential ($I > 10^{14}$ W/cm^2). Here, the multiphoton picture is no longer suitable. It is thus necessary to find a new approach to describe ionization. If the laser frequency is low (starting from the near infrared region), it is possible to use a quasi-static approximation which was introduced in 1965 by Keldysh [6]. In this model, the atom "sees" the incident light as an oscillating field (figure 1.5(a)) [21, 22]. The field bends the Coulomb potential to form a barrier through which the electron can tunnel, as shown in figure 1.5(b). A factor γ, called Keldysh parameter, was introduced to define the transition between the two different ionization regimes as a function of the laser field strength

and frequency. Expressed in atomic unics ($m = e = \hbar = 1$), this parameter is defined as

$$\gamma = \omega\sqrt{2E_b}/F_0 \tag{1.8}$$

where E_b is the binding energy of the electron, ω and F_0 are the frequency and the strength of the laser field respectively. If γ is higher than unity, the multiphoton process takes place. For $\gamma \ll 1$, tunneling ionization dominates.

The experiments presented in this work are performed with a Ti:Sa laser light ($\omega = 0.056$ a.u.) at field strengths such that the factor γ is much less than unity. It is then appropriate to state that the tunneling picture is suitable to describe the results. For this reason some theoretical consideration about tunneling will follow.

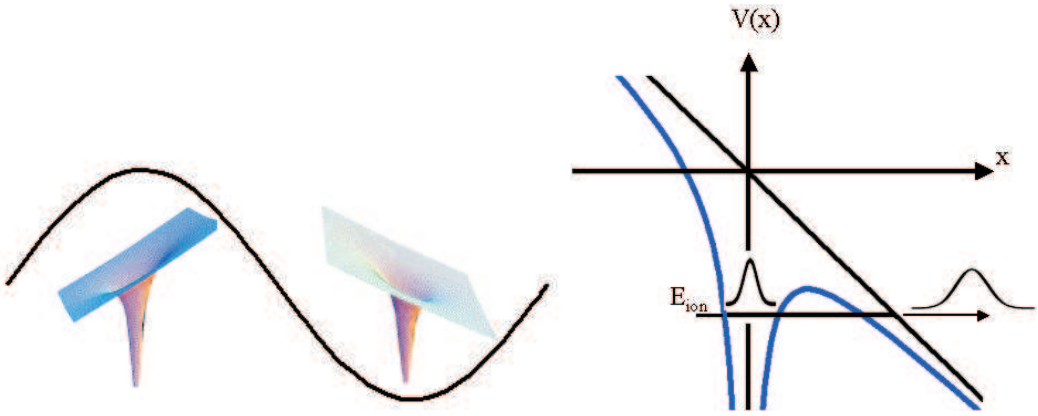

(a) (b)

Figure 1.5: Tunneling picture. (a) The electric field is seen as an oscillating field. (b) The electric field bends the Coulomb potential to form a barrier through which the electron can tunnel.

Tunneling in an electric field

The one dimensional potential of an electron moving in an atomic field and a static field F_0x is described by

$$V(x) = -F_0x - \frac{Z}{x}. \tag{1.9}$$

The electric field bends the Coulomb potential to form a barrier as shown in figure 1.6a). The barrier reaches its saddle point V_s at a position x_s given

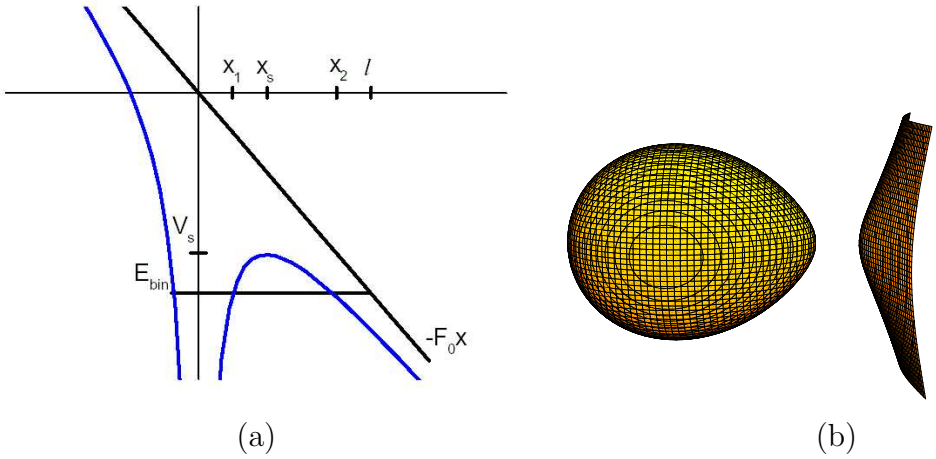

(a) (b)

Figure 1.6: Tunneling ionization. (a) One-dimensional picture. (b) Equipotential surface for the case $E_b = -Z/r - F_0 x$ just below the barrier.

respectively by

$$\frac{\partial V(x)}{\partial x} = 0 \qquad \Longrightarrow \qquad x_s = \sqrt{\frac{Z}{F_0}} \tag{1.10}$$
$$V(x_s) = V_s = -\sqrt{4ZF_0}$$

If the binding energy of the electron is below the saddle point, it is possible to determine the length of the barrier l_1 solving the equation:

$$-E_b = -F_0 x - \frac{Z}{x} \quad \Longrightarrow \quad x_{1,2} = \frac{E_b \pm \sqrt{E_b^2 - 4ZF_0}}{2F_0} \tag{1.11}$$

$$l_1 = x_2 - x_1 = \frac{\sqrt{E_b^2 - 4ZF_0}}{F_0} \tag{1.12}$$

It has to be noted that in the Keldysh quasi-static approximation, the Coulomb potential is firstly neglected. Hence, the barrier through which the electron tunnels is generated by the external electric field and its width becomes $l = E_b/F_0$. The previous description is one-dimensional because the

action of the electric field is influencing only one axis (x-axis). However, the Coulomb potential is a three dimensional system defined as

$$V_c = -\frac{Z}{\sqrt{x^2+y^2+z^2}} = -\frac{Z}{r} \tag{1.13}$$

In figure 1.6(b) is shown the equipotential surface for the binding energy level E_b subjected to a potential $V(r) = -Z/r - F_0 x = -E_b$. The electron is confined classically in an egg-shaped volume, although quantum-mechanically it can tunnel to the continuum, on the right side.

Over-the-barrier ionization

As the field strength increases, the barrier becomes smaller. The saddle point decreases until it becomes equal to the electron binding energy so that the electron is no longer bound (figure 1.7(a)). The process changes from tunneling to over-the-barrier ionization (OBI) [23]. The field strength at

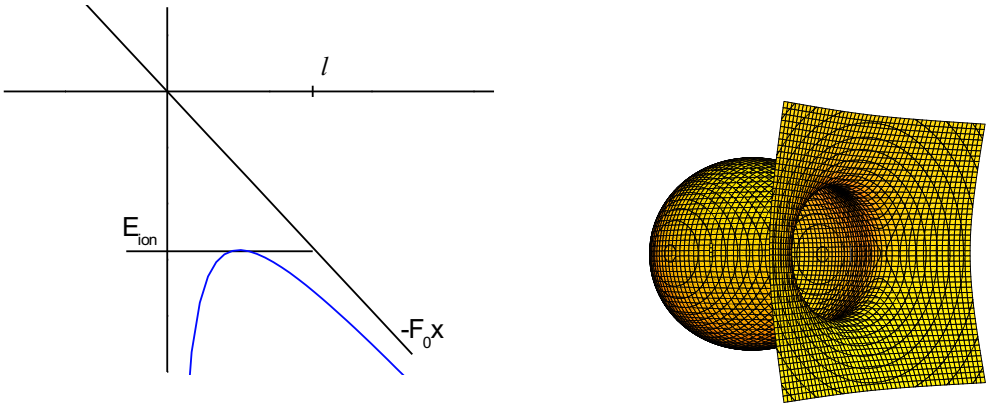

a b

Figure 1.7: (a) Threshold intensity for over-the-barrier ionization in 1D representation. (b) Equipotential surface for the binding energy of the electron. The external field, in this case, is so strong that $V_s < E_b$.

which the top of the barrier (V_s) is equal to the electron binding energy (E_b),

is designated as the threshold field strength between the two processes and it can be easily calculated as:

$$V_s = -\sqrt{4ZF_0} = -E_b \Longrightarrow F_{OBI} = \frac{E_b^2}{4Z} \tag{1.14}$$

The intensity threshold is then,

$$I_{th}(W/cm^2) = 4 \times 10^9 \frac{E_b^4[eV]}{Z^2}. \tag{1.15}$$

As for the case of tunneling, it is possible to represent in a 3D picture the equipotential surface for an electron (see figure 1.7(b)) for a value of $F_0 > E_b$. A circular opening arises, through which the electron can classically escape.

Over-the-barrier ionization for complex atoms The threshold field strength defined in equation (1.14) does not take into account the orbital angular momentum of the initially bound electron. A more general formula is derived in [24] for atomic systems which do not present exceptional symmetry for the solution of the Coulomb potential. The expression is thus not valid for hydrogenlike ions. The extended threshold F_{cr} is given by

$$F_{cr} = A(m)\left(\frac{E^2}{4Z}\right), \tag{1.16}$$

where $E = E_b + \delta E_{dc}$ is the binding energy of the electron subjected to a dc Stark shift. The factor $A(m)$ is an enhancement factor which depends on the magnetic quantum number m and it is defined [24] as

$$A(m) = \frac{1 - 3/32(|m|/n^*)}{1 - 19/32(|m|/n^*)}. \tag{1.17}$$

The parameter n^* = is $\sqrt{Z^2e^2/(2a_0|E_b|)}$ with $a_0 = \hbar^2/(\mu m e^2)$. Usually, the Stark effect is negligible, so that n^* reduces to the effective principle quantum number of the unperturbed atomic level. If $m = 0$, $A(0) = 1$ and F_{cr} reduces to F_{OBI}. When $m \neq 0$, the threshold intensity is increased by a factor $A(m)^2$. There are two reasons for this. Firstly, because of the symmetry of the atomic potential, the atomic energy is shared between the motion in the $y-$axis (polarization direction of the electric field) and in the plane perpendicular to it. On the other hand, when $m \neq 0$, the angular momentum barrier pushes the electron off the $y-$axis so that a stronger field is required to pull the electron again along it.

Stark effect Correlated with a strong electric field is the AC Stark effect. In the tunneling regime, the laser frequency is much smaller than the transition frequency from the ground state to the first excited state. Thus, it is possible to approximate the AC Stark by a DC Stark shift [25]. It consists in a shift δE_{st} of the atomic energy level E_b by

$$\delta E_{st} = -\frac{1}{2}\alpha F_0^2 \tag{1.18}$$

where α is the polarizability of the atom. Additionally, the Stark shift of highly excited states does not influence ionization from the ground state. In fact, an electron is not excited to higher bound states by tunneling.

1.3 Ionization probability

In 1966, Permelov, Popov and Terent′ev developed a method for calculating the probability of ionization of a bound state under the action of an alternating field (PPT theory) [26]. This method is valid for laser fields with $\omega \ll \omega_t$ where ω_t is the tunneling frequency defined as $\omega_t = F_0/\sqrt{2E_b}$. In this way, it is possible to solve the problem of ionization in an adiabatic approximation. While the electron is tunneling, in fact, the change of the field can be neglected.

They have shown that the ionization rate of an arbitrary atom in an oscillating electric field is proportional to the rate in a stationary field. They differ only by a factor given by averaging the rate over a period of the external field. This means that the ionization occurs mainly at the maximum values of the field.

ADK Theory for complex atoms Twenty years later Ammosov, Delone and Krainov extended the PPT theory to complex atoms and ions [7]. Their theory is known as "ADK-theory".

Considering an external field of the form

$$\mathbf{E} = F_0 \cos(\omega t), \tag{1.19}$$

and an electron located in a Coulomb potential, the tunneling rate for a complex atom given by the ADK model [7] is

$$w_{adk} = E_b \mid C_{n^*l^*} \mid^2 f_{lm} \exp\left(-\frac{2(2E_b)^{3/2}}{3F_0}\right) \left(\frac{2(2E_b)^{3/2}}{F_0}\right)^{2n^*-|m|-1} \left(\frac{3F_0}{\pi(2E_b)^{3/2})}\right)^{1/2}, \tag{1.20}$$

where $n^* = \frac{Z}{\sqrt{2E_b}}$ and $l^* = n^* - 1$ are the effective principal and angular quantum numbers respectively and m is the magnetic quantum number. The factor $(3F_0/\pi(2E_b)^{3/2})^{1/2}$ appears from averaging over a period of the field, while $\left((2(2E_b)^{3/2})/F_0\right)^{2n^*-|m|-1}$ takes into account the corrections for the Coulomb potential. The coefficients $\mid C_{n^*l^*} \mid^2$ and f_{lm} are respectively

$$\mid C_{n^*l^*} \mid^2 = 2^{2n^*}[n^*\Gamma(n^* + l^* + 1)\Gamma(n^* - l^*)]^{-1}, \tag{1.21}$$

which generalizes the formula for the hydrogen atoms to complex atoms with different values of the quantum numbers, and

$$f_{lm} = \frac{(2l+1)(l+ \mid m \mid)!(2^{-|m|})}{\mid m \mid!(l- \mid m \mid)!}. \tag{1.22}$$

Tunnel ionization in circularly polarized light It is important to remember that the formula described previously for the ionization probability is valid in the case of linearly polarized light. The dependence of the probability on the ellipticity of the field was treated in [26]. For an elliptically polarized light, the field is given by

$$E = F_0(e_x \cos(\omega t) \pm \epsilon e_y sin(\omega t)). \tag{1.23}$$

The circular polarization is given for $\epsilon = 1$. The ionization rates for circularly polarized light differ from the rates for linearly polarized light by the factor $(3F_0/\pi(2E_b)^{3/2})^{1/2}$ so that

$$\omega_{circ} = (3F_0/\pi(2E_b)^{3/2})^{-1/2}\omega_{adk} \tag{1.24}$$

Because $F_0 \ll E_b$, the rates for circularly polarized light are always higher than the rates for linearly polarized light. However, at the same intensity the field strengths are always a factor $\frac{1}{2}$ smaller than for linear polarization.

1.4 Tunneling in relativistic regime

The ionization processes and their underlying theories described in the previous sections occur at intensities below 10^{16} W/cm^2. At higher laser intensities, the velocity of the electron in the continuum approaches the speed of light ($v \simeq c$) and the relativistic effects, caused by the presence of the magnetic field component of the laser beam, are no longer neglegible. Furthermore, the ionization of strongly bound electrons takes place for which the binding energy becomes comparable to the rest mass. It is possible, then, that the magnetic field affects the sub-barrier motion of the electron during tunneling.

Because the experiments presented in this work are carried out in an intensity regime which approaches the relativistic domain, it is necessary to discuss if and eventually how relativistic effects are influencing the ionization rates. Currently, only one paper is known which is treating this problem [27], giving for the first time a quantitative prediction of the tunnel ionization rate in relativistic laser fields. An analytical formula is derived using the Klein-

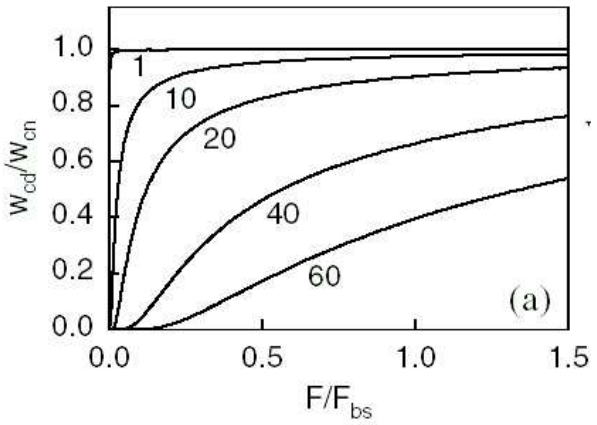

Figure 1.8: Ratio of relativistic (Dirac) to nonrelativistic ionization rates in an electromagnetic field for several charge states [27].

Gordon and the Dirac equations. The solution of such formula for a Coulomb

potential is

$$\omega_{cd} = \frac{mc^2}{\hbar^2}\frac{1}{2\sqrt{3}\Gamma(2\epsilon+1)\xi}\sqrt{\frac{3-\xi^2}{3+\xi^2}}\left[\frac{4\xi^3(3-\xi^2)^2}{\sqrt{3}(1+\xi^2)}\right]^{2\epsilon}\left(\frac{F_S}{F}\right)^{2\epsilon-1}\times \sqrt{\frac{2F}{\pi F_s\beta}}\exp -(\beta(F_S/F)+6\mu\arcsin(\xi/\sqrt{3})) \tag{1.25}$$

where $\mu = Ze^2$, $\epsilon = [1+\mu^2/(1+\sqrt{1-4\mu^2})^2]^{-1/2}$ denotes the total relativistic energy of the ground state and $F_S = m^2c^3/(e\hbar)$ is the Schwinger field strength corresponding to $I_S = 4.7\times 10^{29}\ W/cm^2$. Additionally, $\xi = \sqrt{1-\epsilon(\sqrt{\epsilon^2+8}-\epsilon)/2}$ and $\beta = 2\sqrt{3}\xi^3/(1+\xi^2)$. The factor $\sqrt{\frac{2F}{\pi F_s\beta}}$ comes from averaging over half a laser period. The comparison between ω_{cd} and ω_{adk} has shown that the deviation of the relativistic from the nonrelativistic rates is 20% for charge states $Z \leq 20$ (see figure 1.8). The ionization of charge states higher than twenty happens for intensities higher than $10^{21}\ W/cm^2$. A deviation of one order of magnitude appears for $Z = 60$. Intensities between 10^{23} and $10^{24}\ W/cm^2$ are necessary however to reach such ionization states.

Stark shift For highly charged ions, the Stark shift is negligible. The atomic polarizability is, in fact, proportional to Z^{-4}. The contribution of the shift at the threshold field strenght $F_{th} = E_b^2/(4Z)$ for over-the-barrier ionization for charge states $Z \leq 20$ is less than 50 meV. With the exception of the first charge state, which presents a shift $\delta E_{st} = 0.026$ meV at $F_{th} = 3.4\ 10^8$ V/cm, for the low charge states ($1 < Z \leq 8$), the shift does not exceed 10 meV (e.g. for $Z = 8$, $\delta E_{st} = 6$ meV at $F_{th} = 3.44\ 10^9$ V/cm) while for the high charge states ($9 \leq Z \leq 20$), it increases up to 50 meV (e.g. for $Z = 15$, $\delta E_{st} = 42$ meV at $F_{th} = 3.1\ 10^{10}$ V/cm). The shift, then, is negligible in comparison to the binding energies which vary from ten to a few hundreds of eV.

Zeeman effect The energy levels of an atom, in the absence of external fields, have no dependence in space. In the presence of a magnetic field **B**, they are split into several fine structure levels, known as Zeeman effect. The magnetic field, by providing a preferred direction in space, removes the degeneracy in the magnetic quantum number m_l.

Usually, an atom has a total magnetic dipole moment $\mu = \mu_b m_l/2$ where $\mu_b = 9.27\times 10^{-24}$ J/tesla. The orientation of the energy levels due to the

Zeeman effect is given by

$$\delta E_{zee} = -\mu B. \tag{1.26}$$

By using the threshold field strength for over-the-barrier ionization to calculate the magnetic field as $B = F_{th}/c$, the typical values for the Zeeman shift vary from a few meV for the low charge states (e.g. $\delta E_{zee} = 7$ meV for $Z = 1$ at $F_{th} = 3.4 \times 10^8$ V/cm) to several hundred for the high states (e.g. $\delta E_{zee} = 0.59$ eV for $Z = 15$ at $F_{th} = 3.1 \times 10^{10}$ V/cm). Although the contribution of the Zeeman effect to the binding energy is more than one order of magnitude higher than the Stark effect, its influence is still negligible in comparison with the dimension of the binding energies.

Chapter 2

Multiple Ionization

For a complete understanding of the results presented in this work, it is also necessary to analyse the behavior of the electron in the continuum. It is responsible, in fact, for several effects that are observable in an atom-laser interaction. Under the effect of the external field, an electron can return to the parent ion and interact with it. Several processes result from such an interaction. The electron can be captured by the ion and high harmonic generation occurs. On the other hand, it can elastically as well as inelastically recollide. In the last case, it results in multi-electron ionization. This work concentrates on the production of multiply charged states in an intensity regime where the tunneling picture describes the single ionization process. For this reason, the following chapter will describe only the mechanisms which lead to multi-electron ionization, while for high harmonic generation it is referred to reviews such as [23]. In this chapter, firstly an overview of the mechanisms in the nonrelativistic regime is given. Later on, the relativistic effects are treated.

2.1 Nonsequential Ionization

The first measurements of ion yields for helium, neon and xenon ionized by strong laser fields exhibit, for the second charge state, a strong deviation from the theoretical curves describing sequential ionization [8, 19, 29, 30, 31]. Typical experimental curves are shown in figure 2.1 [8]. The points correspond to the data obtained by double ionization of helium with a linearly polarized, 100 fs, 780 nm light wave. The solid curves are the expected

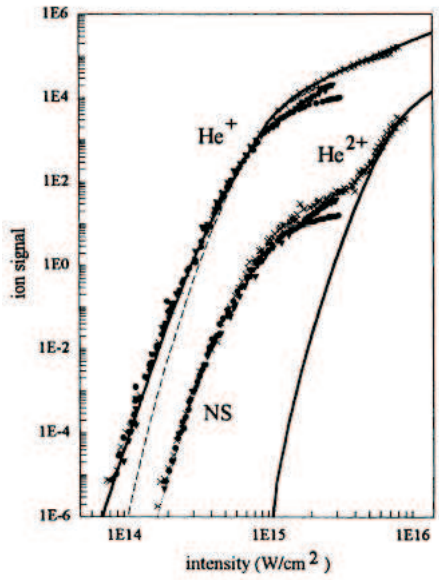

Figure 2.1: Measured He^+ and He^{2+} ion yields [8] as function of the laser intensity. The laser light is linearly polarized, with 100 fs pulse width and a center wavelenght of 780 nm. The solid lines correspond to the yields calculated using SAE [28]. The dashed line represents the ion yields for He^+ calculated using the ac-tunneling ADK rates [7]. The deviation of the data from the theoretical curves near saturation are due to volume effects.

behavior for sequential ionization calculated with the single electron approximation (SEA) [28]. The ion yield for the single ionization is in agreement with the theoretical curve. The data for He^{2+}, however, show a discrepancy of many orders of magnitude from the theory. A nonsequential (NS) ionization process, where two electrons are emitted "simultaneously" from the core:

$$He \Longrightarrow He^{2+} + 2e^-$$

has been invoked to interpret such high rates. The data agree with the model for sequential ionization (solid line) only at intensities above the saturation threshold ($I = 1.5 - 8\ 10^{14}$ W/cm^2). Here, in fact, all the neutral atoms in the volume are ionized, so that only He^+ ions are present in the interaction region and He^{2+} can be generated only through sequential ionization. Later, several experiments investigating different noble gases reproduced the same

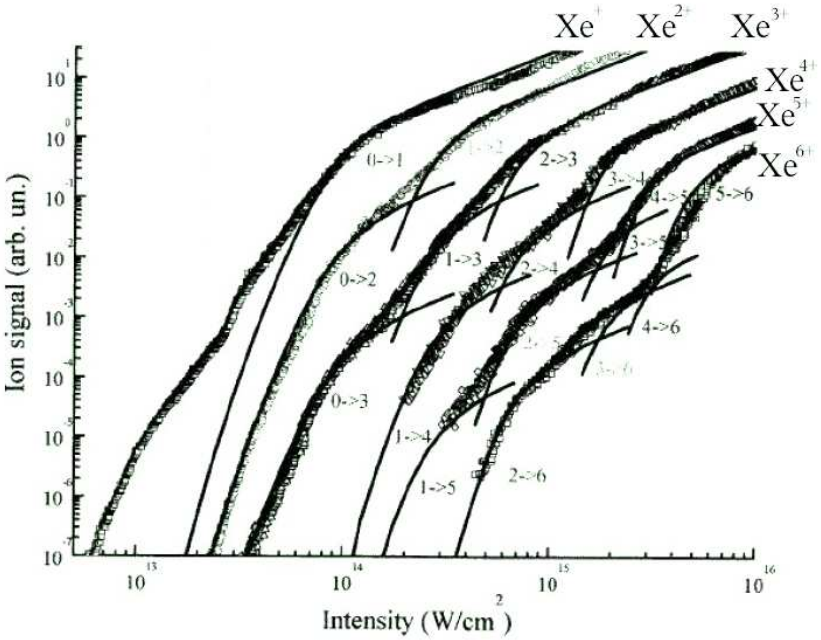

Figure 2.2: Multiple ion yields of xenon as function of the laser intensity (from [9]). The laser light is linearly polarized and with a center wavelength of 800 nm. The curves (solid lines) correspond to the calculation taking into account several ionization transitions.

deviation in the ion yield curves [9, 32, 33]. The group of Chin [9] has observed the nonsequential ionization in xenon up to the sixth charge state (see figure 2.2) and up to the third charge for argon.

2.1.1 Mechanisms behind nonsequential Ionization

So far, the time-dependent response of a multielectronic atom to an ultra strong laser field had been described within the single electron approximation (SAE). Because the correlation between the electrons is included only in the initial wave function, the multiple ionization is assumed to occur sequentially. The SAE approximation breakdown implied by the results of figure 2.1 and 2.2 triggered the search of new mechanisms that could reflect the importance of electron-electron correlation.

"Shake-off" Mechanism

Fittinghoff et al. proposed a model in which the nonsequential ionization proceeds through a "shake-off" mechanism [30]: when the first electron escapes, an inner electron experiences a rapid change in the potential. The electron cannot adapt to this instantaneous variation and it might be "shaken" and also become free. To simulate this process, two parameters were introduced: the intensity at which double ejection becomes probable, called critical intensity I_c, and the probability a^2 ($a \sim 0.5\%$) that the second electron is ionized.

In order to get the population for the second charge state, the new conditions have been taken into account in the rate equations, as follows:

$$\begin{aligned} \frac{dN_0}{dt} &= -R_{01}N_0 \\ \frac{dN_1}{dt} &= R_{01}N_0 - R_{12}N_1 \\ \frac{dN_2}{dt} &= (R_{12} - R'_{12})N_1 - R_{23}N_2 \end{aligned} \tag{2.1}$$

where R_{ij} are the ionization probabilities for sequential ionization and $R'_{12} = a^2 R_{12}$ if the intensity is above the critical intensity. To estimate I_c, Fittinghoff relates it to a previous experiment reported in [34]. The ion yield obtained by integrating the above equation rates can reproduce the experimental data for He^{2+}.

However, a few inconsistencies are immediately obvious. The shake-off model does not give any dependence of ion yields on the laser polarization. Therefore, it cannot easily explain the suppression of the nonsequential ionization observed in experiments with circularly polarized light [19, 35, 36]. Additionally, the model assumes that both electrons escape almost in phase at the maximum of the field. So, both electrons should be ejected in the same direction, which is in contrast to the back-to-back emission expected according to the threshold law for single ionization discussed in [37].

Collective Tunneling

Another model was suggested by the group of U. Eichmann [38]. Here, the assumption is that of a collective tunneling process. Numerical calculations have shown that two electrons could simultaneously tunnel if both are in

equilibrium at the same distance from the core. The tunneling rates calculated within this model are, however, too low to explain the enhancement in the ion yield due to nonsequential ionization for the pulse duration encounted in today s experiments.

Rescattering Model

An alternative mechanism was proposed by Corkum [12]. It is based on electron-electron inelastic rescattering. The first ejected electron interacts with the field of the laser radiation. Within half of an optical cycle the electron returns to the nucleus. If the kinetic energy the first electron acquires from the field (the maximum value of this energy is $3.17U_p$) exceeds the binding energy of the second electron, the ion core can be collisionally ionized as follows:

$$e^- \quad + Kr^{q+} \quad \rightarrow \quad Kr^{(q+1)+} \quad + e^- + e^-$$

where q represents the residual charge of the ion. This model describes qualitatively several phenomena in high intensity laser fields: generation of high harmonics [39], the energy distribution of the photoelectrons and the angle distribution of the high energy electrons emitted in ATI [40]. The strong polarization dependence of the nonsequential ionization process observed in [36] is also explained by this model. The overlap between the electron wave packet and the core is getting more improbable with the increase of the ellipticity. Nonsequential ionization is observable for linearly polarized light only. Additionally, new experiments using differential methods confirm the validity of this model [10, 41, 42, 43, 44]. In these experiments the momentum distribution of ions and electron can be measured. Informations on the dynamics which play a role in nonsequential ionization are obtained where integral measurements fail.

The rescattering model is now widely accepted as the mechanism for nonsequential ionization, though a few puzzles are still present.

From the theoretical point of view, several approaches have been taken in consideration for the description of this effect: computations in which the Schrödinger equation is solved directly [45, 46, 47] or which employ Floquet-Fourier transformation [48, 49, 50], $S-$matrix techniques [51], but also more

intuitive approximate models [8, 12, 52]. In the final part of the chapter, the most important of those approaches are presented.

- **Numerical Solution of the Schrödinger Equation**

  One method consists in the full numerical solution of the time dependent Schrödinger equation (TDSE) for a Helium atom (two electron system) in an external electromagnetic field. Several groups are engaged with it [46, 53, 54, 55, 56]. The group of Burnett [46], starts with the correction of the SAE approximation, so that the influence of the outer to the inner electron is taken into account. This is done including the Coulomb correlation term. The 3D model is able to describe quantitatively the experimental data for Helium from the group of DiMauro [8] with the suggestion the outer electron is returning back to core and interacting with the remaining electron.

- **S-Matrix**

  The S-Matrix theory proposed by Becker and Faisal [57] produces ion yield curves that are in very good agreement with the experimental data of many groups. The model explains the nonsequential ionization process as following: the outer electron absorbs from the laser field a number of photons higher than its binding energy (virtual ATI process). The excess energy is transferred to the inner electron via correlation and the two electrons leave the core simultaneously. The S-matrix model releases an exact solution for He. For different atoms and for different laser parameters several approximations have been used and a good agreement has been achieved with the measurements for atoms subjected to a linear polarized light [33, 58, 59]. However, up to now, no calculations have been performed for the case of circularly polarized light.

- **Quasiclassical Recollision Model**

  Several groups focused their attention on a semiclassical rescattering model [8, 22, 52, 60]. In the simplest version [22], three steps can be distinguished. First, a bound electron tunnels free at a particular phase of the field with a rate determined by the ADK theory. In the second step, it classically moves in the laser field. Initially the electron is accelerated away from the core, but within half a cycle, it is driven back to the ion core. During the time it is returning, the wave packet

spreads. In the third step, the recolliding wave packet has enough energy to interact with the core via e−2e inelastic rescattering. In the first calculations using this model, the probability for ionization was determined by comparing the returning wave packet with the inelastic cross section. The results have given double ionization probabilities that were too low to explain the experiments [8, 52]. Later, more complete calculations have taken in consideration spin factors and Coulomb field effects on the electron wave packet and improved the agreement with the experiments [60]. However, recollision models are limited for the prediction of the behavior of two-electron systems because many physical processes are only accounted in an approximative manner.

Despite the recent development of computational techniques for investigating double photoionization, serious disagreements remain between the various calculations. For our investigations, we will discuss the nonsequential ionization using the quasiclassical recollision model, because we are interested only in a qualitative approximation of the effect.

2.2 Electron dynamics in nonrelativistic regime

Once the electron is released by the tunnel effect, it appears in the continuum with zero initial velocity. Its further motion is described by the Newton equations for a free charged particle in an electromagnetic field. The force acting on it is

$$\mathbf{F} = q(\mathbf{E} + \mathbf{v}/c \times \mathbf{B}) \tag{2.2}$$

The electric and magnetic field components for a linearly polarized light wave with a frequency ω are described respectively by:

$$\begin{aligned} \mathbf{E} &= F_0 cos(\omega t) \\ \mathbf{B} &= B_0 cos(\omega t) \end{aligned} \tag{2.3}$$

with $B_0 = F_0$. When $v << c$, the magnetic field component can be neglected (nonrelativistic regime). For the periodicity of the laser field, it is possible to investigate the electron dynamics in an oscillating electric field within a

period $T = 2\pi/\omega$. The position and velocity at the time of ionization t_0 are set to 0. The electron is accelerated by the field away from the core with:

$$\ddot{y}(t) = \frac{d^2y}{dt^2} = \frac{eF_0}{m}\cos\omega t. \tag{2.4}$$

Expressed in atomic unics, equation (2.4) simplifies to:

$$\ddot{y} = F_0 \cos\omega t. \tag{2.5}$$

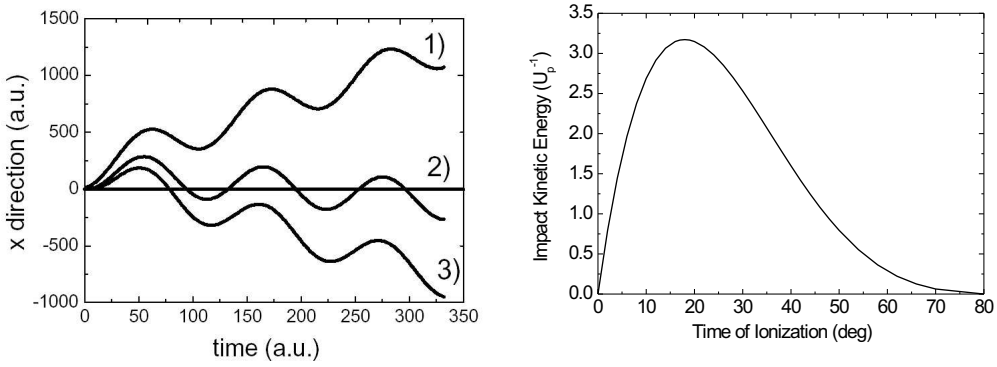

(a) (b)

Figure 2.3: a) Trajectories of an electron during a laser period. The electron was ionized at different laser phases. Respectively at: (1) $\omega t_0 = -20°$; (2) $\omega t_0 = 5°$ and (3) $\omega t_0 = 18°$. b) Kinetic energy of the returning electron as a function of the initial ionization time.

Then, it is possible to determine the electron velocity and position at a time t, by resolving the classical motion equations:

$$\dot{y}(t) = \int_{t_0}^{t} \ddot{y}dt = -\tfrac{F_0}{\omega}\left(\sin(\omega t) - \sin(\omega t_0)\right) \tag{2.6}$$

$$y(t) = \int_{t_0}^{t} \dot{y}dt = -\tfrac{F_0}{\omega^2}\left[(\cos(\omega t) - \cos(\omega t_0)) + \omega(t - t_0)\sin(\omega t_0)\right].$$

The electron trajectories along the polarization direction strongly depend on the ionization time. This means that the phase ωt_0 at which the electron is set free from the core plays an important role in the electron dynamics. In figure 2.3a) are shown the electron trajectories during a laser period, for three initial phases. In one case, the electron does not intersect $y = 0$

anymore (figure 2.3(1)), in the other two cases, the electron can return more times (figure 2.3(2)) or only once (figure 2.3(3)). When it is returning back ($y = 0$), it will have a kinetic energy $E_{kin} = 1/2\dot{y}^2$. Its energy depends on the laser phase at which it is ionized. Figure 2.3b) shows this dependency. As already mentioned, to ionize further the ion core, the returning electron should have a kinetic energy higher than the binding energy of the second electron. In the nonrelativistic regime, it can happen that such a condition is satisfied only when the electron acquires its maximum kinetic energy of $3.17U_p$ (initial phase $wt_0 = 18°$ or $wt_0 = 108°$).

2.3 Electron dynamics in relativistic regime

The intensity region we are interested in investigating lies in the transition regime between the nonrelativistic and fully relativistic domains. In this "quasi"-relativistic regime the magnetic field influences the electron dynamics but the machinery of relativity does not seem to be required yet [61], as shown in figure 2.4.

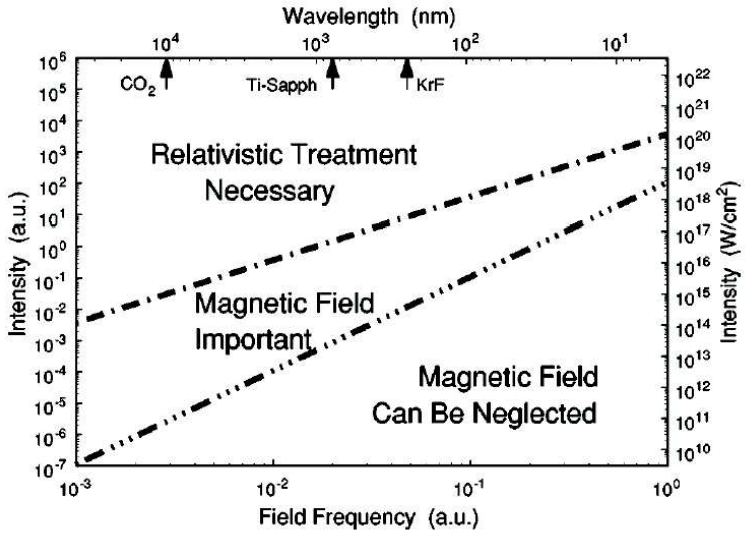

Figure 2.4: Importance of the magnetic effects depending on field strength and laser wavelength.

.

In the following, first and second order relativistic effects that could influence the electron motion are briefly described. In the discussion of the experimental results, they will be treated in more detail.

First order relativistic effects

In the "quasi"-relativistic regime the force acting on the electron is given by the Lorentz force

$$\mathbf{F} = q(\mathbf{E} + \mathbf{v}/c \times \mathbf{B}) \tag{2.7}$$

Here, the magnetic field component $\mathbf{B}$ is no longer negligible. It is possible then to calculate the trajectories along the laser polarization ($y(t)$) and propagation ($x(t)$) direction respectively. Because of the electric field component,

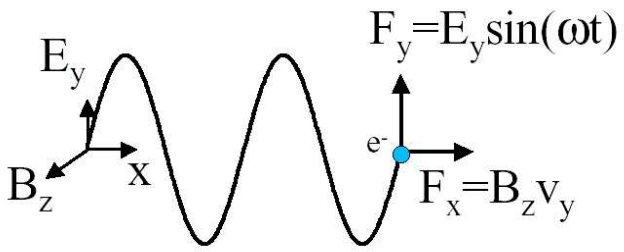

Figure 2.5: An electromagnetic wave acts on an electron with a force $\mathbf{F} = q(\mathbf{E} + \mathbf{v} \times \mathbf{B})$.

the electron will move along the polarization direction of the laser, under the force $F_y = E_y \sin(\omega t)$ and it will acquire a velocity v_y. The magnetic field component acts on the electron with $F_x = B_z v_y \sin(\omega t)$. It is possible to calculate the electron trajectories by solving numerically the Newton equations [23]:

$$\frac{d\dot{y}(t)}{dt} = E_y \cos(\omega t); \tag{2.8}$$

$$\frac{d\dot{x}(t)}{dt} = E_y/c\dot{y}(t) \cos(\omega t).$$

The solutions are calculated starting at an ionization time t_0 and setting as initial condition $x(t_0) = l$ where l is the end of the tunnel. In this intensity regime, the Lorentz force acting on the electron is reduced by the ratio v/c due to the magnetic field.

Fully relativistic domain

True relativistic effects, however, are $(v/c)^2$ effects. Because the electron rest mass has to be taken into account, the motion equations (2.9) change into the form

$$\frac{d}{dt}\frac{\dot{y}(t)}{\sqrt{1-(\dot{y}(t)/c)^2}} = E_y \cos(\omega t); \tag{2.9}$$
$$\frac{d}{dt}\frac{\dot{x}(t)}{\sqrt{1-(\dot{x}(t)/c)^2}} = E_y/c\dot{y}(t)\cos(\omega t).$$

In the discussion of the experimental results, both the treatments will be considered and compared over an intensity domain between 10^{14} and 10^{19} W/cm^2. We want to make a statement whether the first order relativistic effects describes the highly charged states ionization or a fully relativistic treatment is already required. Additionally, we will compare the results obtained with a third case, where the effect of the Coulomb potential is also taken into consideration. In the previous cases, in fact, the assumption is that the electron is free in the electromagnetic field. In reality after ionization, the electron is still near the ionic core which may act on the electron via Coulomb refocusing [62].

Chapter 3

Laser System

The experiments described in this work, were conducted with the 30 TW laser system at the Max Born Institute. It generates $35 - 40$ fs pulses at a wavelength of 815 nm. The precision with which the parameters are determined is very important for the calibration of the ion yield curves. For this reason, the next chapter is dedicated to the description of the laser system as well as to the methods for the characterization of its parameters.

3.1 The 30 TW Laser System

The laser system at the Max Born Institute is a multi TeraWatt (TW) Ti:Sapphire laser [63].

The ultrashort laser pulses are generated via Chirp Pulse Amplification (CPA) [1, 64]. The laser composition is shown in figure 3.1.

It consists of a master oscillator, a pulse stretcher, four stages of amplification and a pulse compressor. The operation of the self-modelocked master oscillator is based on the Kerr nonlinearity arising in the laser crystal. Intracavity chirped mirrors are introduced to compensate group velocity dispersion. The Ti:sapphire crystal is pumped by a 5 W cw diode laser. The master oscillator produces a continuous sequence of linearly polarized Fourier-transform limited 12 fs pulses with 13 ns temporal gap and about 300 mW average power ($\approx 0.5 \times 10^{-9}$ J/pulse). It is the feature of CPA technique that before amplification the short femtosecond pulse is stretched in time by introducing a frequency chirp onto the pulse. It increases the pulse duration to a sub-nanosecond range. The optimal duration of the stretched

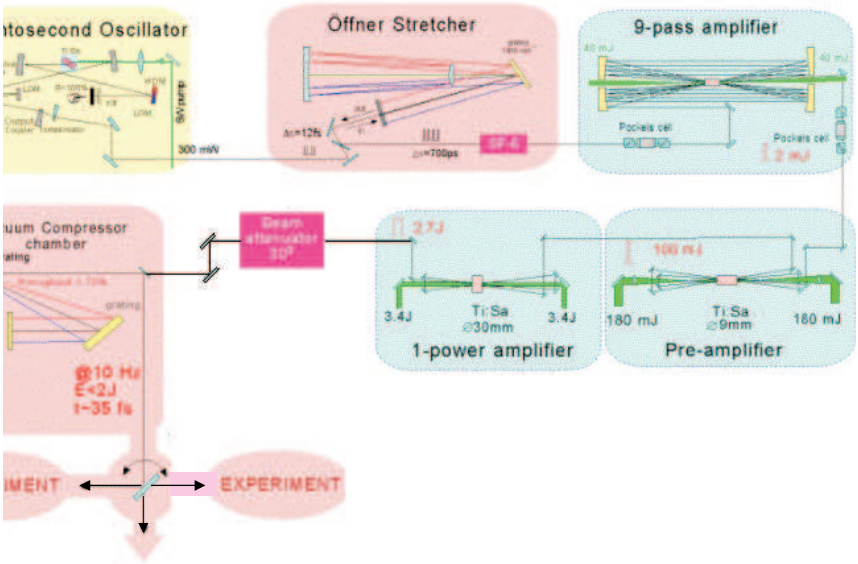

Figure 3.1: Multi-TW Ti:Sapphire scheme.

pulse is determined by the need to avoid damage to the optics and to eliminate nonlinear distortions in the spatial and temporal profile of the beam. Typically for terawatt CPA systems, an expanded pulse duration of $\geq$ 200 ps is necessary.

Just after the stretcher, to increase the energy from nJ to mJ level, a high-gain amplifier is used. The amplification occurs mostly in this stage. At first, the low-energy chirped pulse is injected into the cavity of a multipass regenerative amplifier. The low-energy chirped pulse is injected into the first pass using a Pockels cell. The presence of Pockels cell in every stage of the laser is necessary to avoid any amplification of sponataneous emission (ASE).

After the 9-th pass the amplified pulse has $\sim$ 4 mJ energy. In order to be isolated from the back reflected radiation, the multipass amplifier is separated from the preamplifier by a second Pockels cell. After this amplifier, the pulse energy reaches about $\sim$ 2.5 mJ. The second step is a preamplifier. After the fourth pass the amplification reaches the saturation and its $100 - 120$ mJ pulses are emitted from the preamplifier. The spectral width of the amplified pulse after the preamplifier has a value of $\Delta\lambda = 38$ nm. The final power stage of the Ti:Sa laser is pumped by four frequency-doubled Nd:Yag

beams. All four pump laser beams are imaged on the surface of a 30−mm diameter 20−mm thick Ti:Sa crystal. The power amplifier is optimized for 3− passes. The power amplifier is able to deliver laser pulses with energy $E_L \sim 1.5$ J at the repetition rate of 10 Hz. The amplified pulse is then directed into a compression vacuum chamber where the high energetic pulses are recompressed via two holographic gratings (40 cm diameter) to a pulse duration $\tau = 35 - 40$ fs. The output beam has a spatial diameter $D = 70$ mm. Once the beam has a focus of the order of μm, the peak intensity can

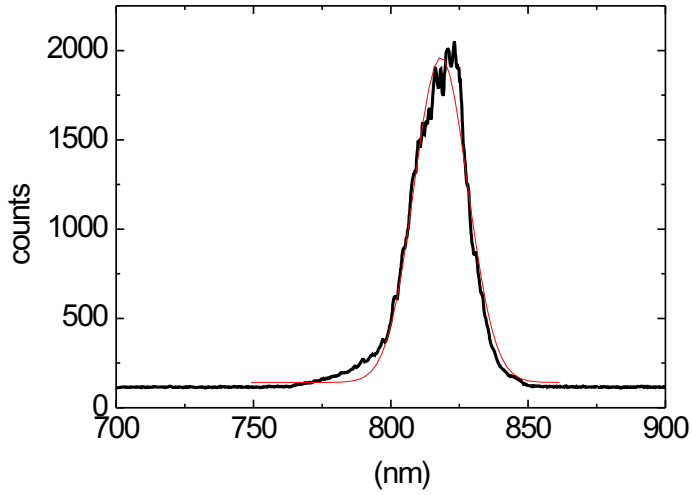

Figure 3.2: The laser spectrum at the entrance of the experimental chamber shows that the wavelength distribution is centered at $\lambda = 815$ nm.

reach 10^{19} W/cm^2 at a wavelength centered at $\lambda = 815$ nm. In the frame of the present work, the measurement of the spectrum has been done with a fiber spectrometer and is shown in figure 3.2.

3.2 Characterization of the laser parameters

A propagating laser beam is usually defined as a gaussian pulse in space and in time. The field amplitude can be described as:

$$E = E_0 exp(-r^2/\omega_0^2) \tag{3.1}$$

where ω_0 is the beam waist which is, for definition, the radius at which the intensity decreases to $1/e^2$. The intensity of a laser beam is given by

$$I = 1/2c\epsilon_0 E^2 exp(-log(2)t^2/\tau^2) = I_0 exp(-2r^2/\omega_0^2) exp(-log(2)t^2/\tau^2) \quad (3.2)$$

where I_0 is the peak intensity and τ is the full width half maximum ($FWHM$) of the gaussian pulse. Integrating (3.2) in time and in space, one obtaines that the total energy E_L available in the pulse is

$$E_L = I_0 \frac{\pi\omega_0^2}{2} \sqrt{\frac{\pi}{log(2)}} \tau. \quad (3.3)$$

The laser beam intensity can be then determined by the formula:

$$I = \frac{0.94 E_L}{\pi\tau\omega_0^2}. \quad (3.4)$$

In the frame of this PhD work, a precise characterization of the energy, pulse width and focus waist has been done to determine the effective value of intensity available during the experiment.

3.2.1 Laser Energy

The energy measurement is done with a calorimeter positioned before the compressor chamber and it is shown, together with the standard deviation, in figure 3.3 as function of the attenuation steps. The energy fluctuations over more than 10000 shots are between 5% and 10%. Inside the compressor and along the way to the experimental chamber, the beam loses about 57% of its energy. Thus, during the experiment, an energy of about $E_L = 0.6 - 0.7$ J is available. The variation of the energy for the measurement of intensity dependent ion yield curves, was obtained via an optical attenuator. The system consists of a rotating basement where two polarizing mirrors are mounted with a 70° incident angle [65]. For a linearly polarized laser beam, only the perpendicular component to the mirror surface will be reflected. The second mirror is used for the amplification of the effect. By the rotation of the system along the optical axis, the effect on the incident beam is a polarization filter which allows a continuous variation of the pulse energy down to $4 - 5\%$ of the maximum energy.

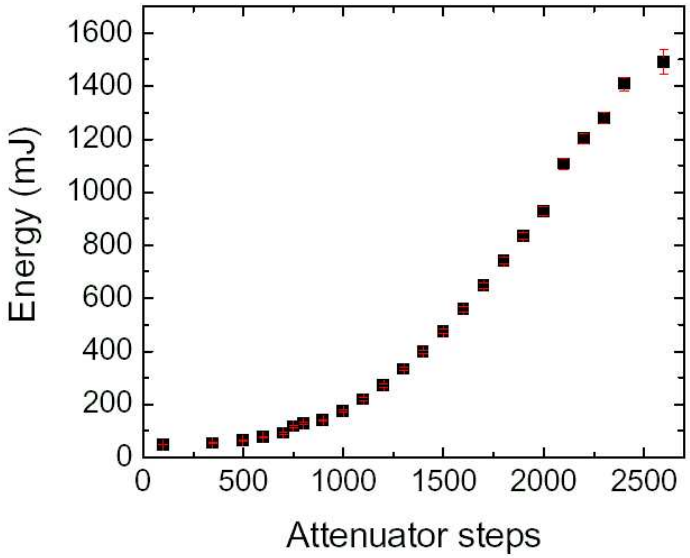

Figure 3.3: Laser energy and its standard deviation (in red) over 10000 shots as function of the attenutation steps. The energy measurement is made before the compression stage.

3.2.2 Focus measurement

Because of the extremely high intensity values that are reached in the focus region, a measurement of the beam waist is difficult. It is not possible to measure it with standard lenses or with high precision microscopes because the laser intensity would destroy the optical elements. The imaging of the focus has to occur using an attenuated beam. The energy is chosen low enough so that the lens is not compromised. A lens with a focal length of $f = 60$ mm is then positioned to image the focus. The image is acquired with a 16 Bit CCD camera (the dimension of the pixels are 9×9 μm). The focus measured with this set-up is shown in figure 3.4. The waist is extrapolated from the profiles along the x and y direction (figure 3.4(b)) of the image. In this case the focus shows an ellipticity along the x direction. The focus radius along the two axes are measured to be $\omega_x = 5.5\mu$m and $\omega_y = 12.5$ μm. This corresponds to an average beam waist of ca. 8.1 μm. Because it is not possible to make an on-line measurement of the focus, shot to shot changes can only be estimated.

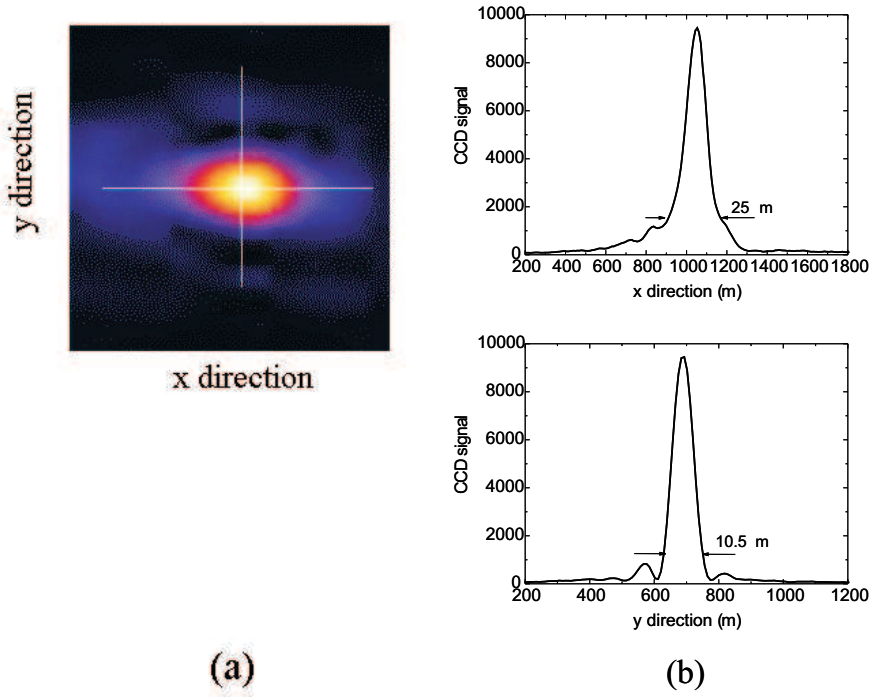

Figure 3.4: The magnification of the focus is ca. 0.1 and the profile extrapolation gives a focus area where the 86% of the energy is contained in $270\mu m^2$. The diffraction rings are due to the quality of the optics used to purse the imaging.

3.2.3 Pulse Width measurement with SPIDER

The typical pulse for the Ti:Sapph available in MBI is shown in figure 3.5 and the result is a width of $35 - 40$ fs. The pulse width is measured with a SPIDER (see figure 3.6a)). This method is capable of providing a precise measurement of very-short pulses. It is based on shearing interferometry in the optical frequency domain. The laser beam passes through a thin beam splitter (etalon). The transmitted beam is stretched into its frequency components while two in time delayed beams are generated by reflection on the two faces of the etalon. The three beams are, then, focused in a crystal where the two replica will interact with different frequencies of the stretched beam (see fig 3.6b)). The result is an interferogram that can be measured with a spectrometer. A program converts the information from the interferogram into the pulse width of the beam.

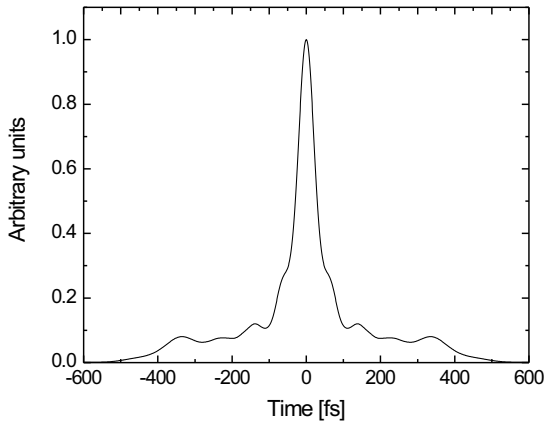

Figure 3.5: The Ti:Sa pulse width measured with the SPIDER method. The result is a 40 fs long pulse.

The pulse width is determined by two parameters of the compressor: the distance and the angle between the gratings. The first is responsible for non-linear errors of the second order in the recompression. A wrong angle determines a non-linear error of the third order. Through a measurement with the SPIDER, it is possible to adjust the compressor parameters until the optimum pulse width is found.

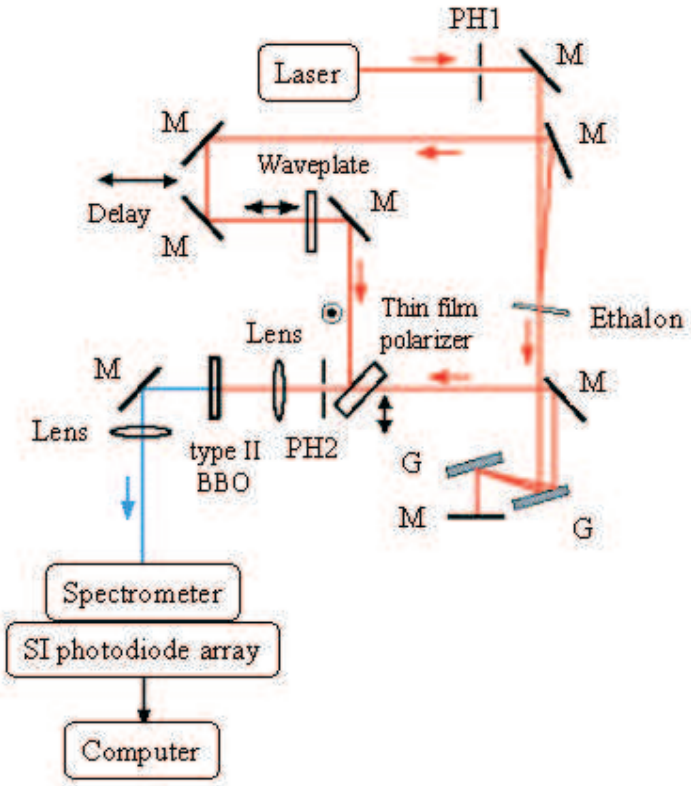

a)

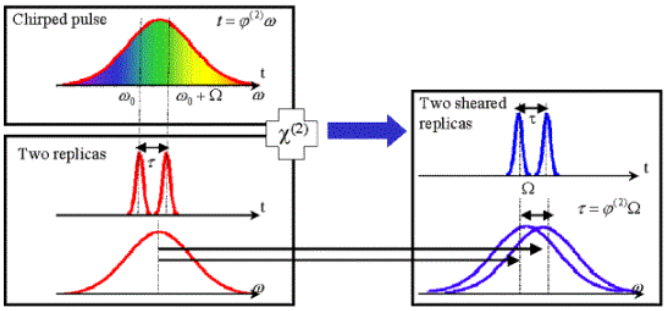

b)

Figure 3.6: a) SPIDER set up for femtosecond pulse measurement. b) the chirped pulse interacts in a non-linear crystal with the two replica delayed in time.

3.3 Cleaning of the Ti:Sa Optical Components

Modern Ti:sapphire lasers [63, 66, 67, 68, 69] reach high-peak power values of the order of Terawatt. The optical components of such systems are subjected to a strong irradiation, while at the same time, they have to ensure a high efficiency and high resistance for a long time. To prevent laser beam degradation due to non-linear effects during its propagation, all components (from the pulse compression stage to the interaction target) are typically mounted in vacuum chambers. Furthermore, this protects sensitive optics from external factors (as e.g. dust and water) present in air. Nevertheless, organic substances are trapped in the mechanical and electronical components that are mounted in the chambers. Such substances evaporate and can be deposited on the surfaces of gratings and other optical components. Because of the high intensity carried by the laser beam, it can be possible that molecules of the layers are cracked and carbon is deposited on the incidence area by the laser beam. A carbon layer will be formed on the optical surface. If this carbon layer is not removed at an early stage, it will absorb energy and the transmission as well as the throughput of the system will be drastically reduced. The continuous absorption of energy and deposition of carbon on the optical surfaces may result in permanent damage of the coating layers.

The deposition of carbon on optical surfaces, particularly on gold coated gratings and mirrors with dielectric coatings, is a typical source of problems for multi-terawatt Ti:Sa laser running in a repetitive mode ($\sim$ 10 Hz). In fact, gold coated gratings cannot be wiped as is possible, to some extent, with "hard" dielectric coatings. Sometimes, laser systems were operated at a reduced repetition rate to avoid the contamination of the mirrors. This, however, limits the performance of the laser unacceptably .

Therefore, in the frame of the present work, a permanently installed system has been developed that permits cleaning of optical elements as soon as any trace of carbon becomes visible. It avoids time-consuming realignment of the optics, and prevents any further contamination.

3.3.1 Cleaning system setup

For the Ti:Sapphire system at Max Born Institute (MBI), we adopted a method for cleaning of XUV optics in electron storage rings [70] and of electron microscopes [71]. For electron microscopes, the action of the electron probe itself polymerizes organic hydrocarbons. In the case of the storage

rings, the molecules are cracked because of the high XUV-photon energy; in our case, it is the high intensity of the optical light.

The procedure is based on the generation of a radio frequency discharge inside the vacuum chamber filled with a mixture of argon (neutral gas) and oxygen (active gas). The produced plasma leads, through charged particle bombardment, to the oxidation of the layers forming CO and CO_2. Under these conditions such molecules do not attach tightly to the surfaces and can be pumped away [72].

The RF discharge is produced by an antenna that consists of a pure aluminium perforated plate connected to a rf-vacuum feedthrough. The RF signal is produced by a RF plasma generator with a fixed frequency (13.56 MHz) and a variable power emission (maximum up to 300 W) into 50Ω load. To avoid that part of the power is reflected back into the RF generator, impedance matching is made through an antenna tuner (Palastar inc.) supporting radio frequencies between $1,8 - 30$ MHz and a maximum power emission of 1500 W. A gas inlet precision valve is used for a fine regulation of the Ar-O_2 mixture. The maximum power used for the cleaning is 50 W and the mixture ratio Ar-O_2 is 0.6 ($0.3Pa$ for Ar, $0.5Pa$ for O_2).

3.3.2 Cleaning Method Characterization

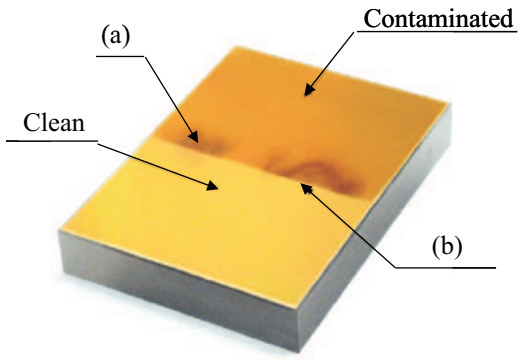

Figure 3.7: Photo of the grating after the cleaning procedure. The cleaning time was about 30 minutes. Half of the surface was covered to show the difference between the grating surface before and after the cleaning.

The cleaning system was first tested in a separate chamber to be sure that it can be applied to laser optics, especially to expensive diffraction gratings.

The picture of a strongly contaminated gold coated diffraction grating (20×16 cm^2) subjected to the cleaning process is shown in figure 3.7. It was used for a period of several months for pulse compression at a level of laser power 5 TW. Imprints of the laser beam ((a) and (b)) are clearly visible. Half of the surface was protected during the process of decontamination by an aluminium cover to observe the result of the cleaning. An exposure time of 30 minutes was enough to significantly remove the carbon layer.

The grating surface structure was probed with an atomic force microscope to determine the influence of the carbon layer and of the cleaning procedure on the grating structure (figure 3.8). This AFM (SIS, Germany) is a very compact instrument, optimised for the inspection of optical surfaces. It is mounted in the objective-turret of an optical microscope and capable of probing samples of up to 1 m lateral dimension. We observed a homogeneous

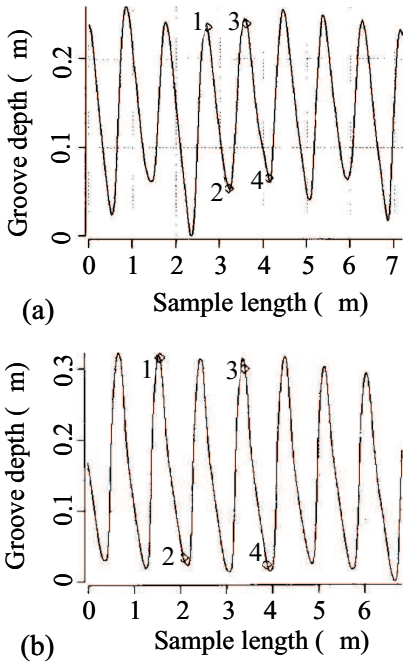

Figure 3.8: (a) Acquisition with an atomic force microscope of the grating surface where the contamination is still strongly visible. The Blaze angle is calculated from the slope of the curve from the points 1 and 2 and from 3 and 4. (b) Acquisition of the surface where the cleaning took place.

groove profile of the cleaned area with a depth of 300 nm (figure 3.8(b)). The

Blaze angle is estimated to be 31°. In the contaminated area (figure 3.8(a)), the groove depth is no longer homogeneous and it has been diminished to $200nm$. The Blaze angle of the grating has changed by the deposited carbon to an average value of 24 deg.

Additionally, the diffraction efficiency of the grating as a function of the incidence angle before and after the cleaning is compared with the efficiency measured for a new grating (figure 3.9). The curves acquired in the case

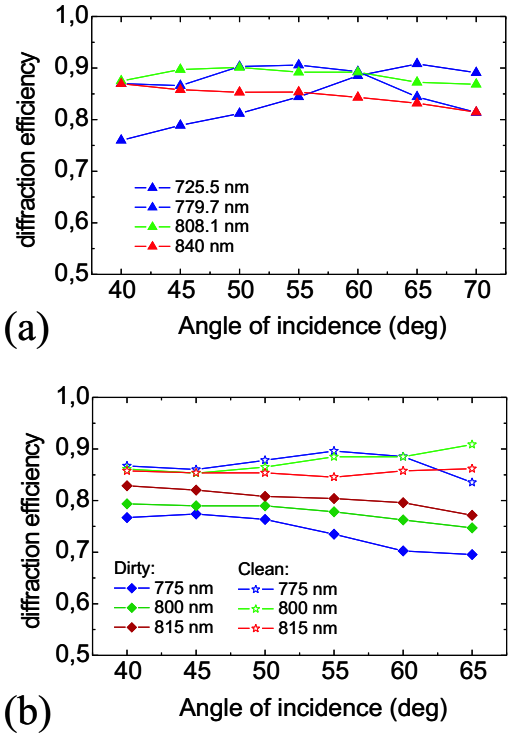

Figure 3.9: Comparison between the diffraction efficiencies for (a) a new grating; (b) the contaminated grating (empty signs) and the cleaned one (full signs).

of a new grating (figure 3.9(a)) show that the efficiencies for different wavelengths are between 80% and 90%. A decrease in reflectivity down to 70% is observable (figure 3.9(b)) for the contaminated area of the grating. After the cleaning, a complete recovery of the grating properties could be achieved.

We install an RF plasma cleaning system as an "on-line" tool in all sectors of our vacuum system, in which optical components require periodical cleaning. It is necessary to adapt the antenna dimension with respect to the

volume of the chamber so that the discharge is homogeneously distributed and a surface reaction takes place. We have installed the cleaning system in the pulse compression chamber (figure 3.10) [63].

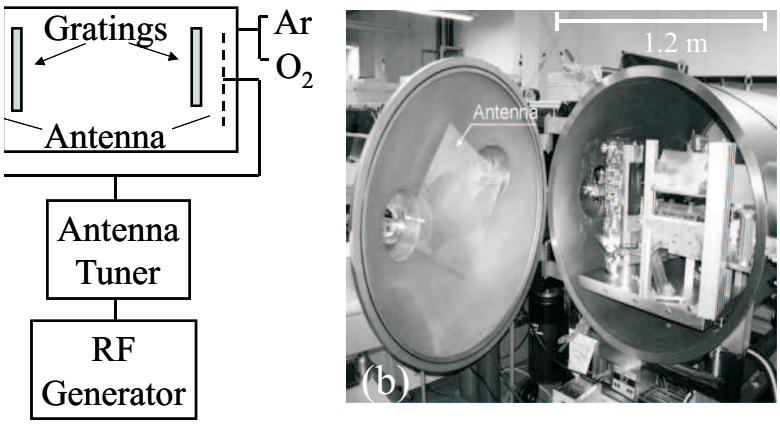

Figure 3.10: (a) a schematic representation of the cleaning system connected to the compressor chamber is shown. (b) one of the antennas mounted in the compressor chamber is shown.

Because of the large dimensions of the cylindrical vacuum chamber of the MBI-Ti:Sapphire laser system ($1.2m$ diameter, $1.5m$ long), two antennas are mounted in a symmetric way on the two sides. Here, the cleaning procedure is adopted as a prevention method. Every time the compressor is exposed to air a discharge runs for a short period before the laser system is used for experiments. A diagnostic system is mounted for the control of the gratings efficiency. A He-Ne laser beam is expanded to have the same diameter of the output Ti:Sa beam. It is diffracted at the same grating position of the Ti:Sa output beam, but, due to the different wavelength, it is reflected in another direction, where the signal is detected by a photodiode. Up to now, no decrease of the grating efficiency has been observed.

Furthermore, we set up a single antenna in a vacuum chamber where a dielectric coated adaptive mirror is installed. This mirror is used to improve the wave front of the laser beam. It has been observed that, periodically, a carbon layer is generated on the area, where the laser beam is incident. The cleaning procedure is applied as soon as the carbon substrate becomes visible. A relatively short exposure time of less than 20 minutes is appropriate to clean the mirror.

The fact that different optical elements show different growth of carbon contamination might be due to different surface quality.

A possible draw back of the method is that it is based on a reactive etching process so that a too long exposure time could lead to damage of optical components. In particular, if the ions produced in the discharge have high kinetic energy, they may cause sputtering. This is especially dangerous for holographic diffraction gratings where a photoresist is present under the gold layer. However, limiting the rf-power to $50W$, after two years of periodically cleaning of our laser optics, no trace of degradation of the optics were observed.

Chapter 4

Experiment

The first part of the chapter is dedicated to the description of the experimental set-up. In the frame of the present work, new focusing optics as well as the detection system have been installed in a previously existing ultra-high vacuum chamber. The second part of the chapter is focused on the description of the method used for the data acquisition.

4.1 Experimental set-up

After the recompression stage, the laser beam is steered through a vacuum tubing system to the experimental chamber. As already mentioned in the previous chapter, the vacuum is necessary to prevent laser beam degradation, due to non-linear effects during its propagation in air. The tubing system is kept under vacuum of the order of magnitude of 10^{-6} mbar. The system is shown schematically in figure 4.1. In the first chamber, an adaptive mirror is present to correct the wave front of the beam using a Hartmann-Schack Sensor. In the second chamber, a rotating mirror is used to direct the laser beam to the different experimental chambers. A system composed of two mirrors is used, at the end, for a fine alignment of the beam in the target chamber. The experiment requires very good vacuum for the measurement of highly charged ions. The background pressure is kept below 5.0×10^{-9} mbar. This is possible by separating the target chamber from the tubing system via a 500 μm thick glass.

The experimental set-up is shown in figure 4.2. The laser beam propagates onto an off-axis parabolic mirror (1) with a diamter of 95 mm, a focal length

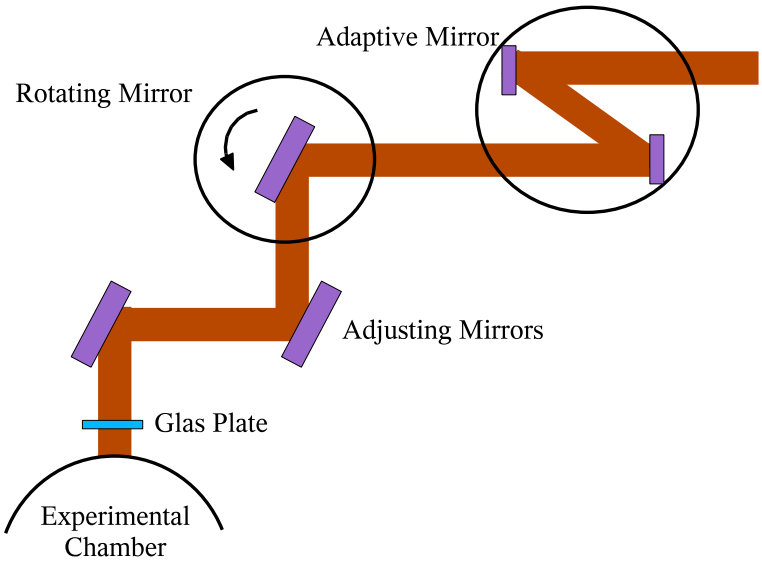

Figure 4.1: Schematic representation of the tubing system between compressor and experimental set-up. The adaptive mirror is used to correct the laser wave front. A rotating mirror is installed to direct the laser beam to the different experimental chambers.

of 150 mm and an off-axis distance of 60 mm. The 70 mm diameter beam is focused in the center of a quadruple of equidistant rods (2), 20 mm apart. An extracting electric field (E) accelerates the ions towards the detector (4). The ions are mass/charge selected by their time of flight (TOF mass spectrometer). To shield the detector from the noise signal generated outside the focal region, a 510 mm long tube (3) was installed between the field rods and the MCP. The detected interaction volume is reduced by introducing a slit with a 0.3 mm aperture (5) between the focus region and the 5 mm opening of the TOF tube. The typical acceleration voltages can vary in a range from 100 to 500 V. The ion detector is a Microchannel Plate (MCP). The output signal from the detector is then amplified and interfaced to the electronic chain necessary for the data acquisition. The signals are converted by a Constant Fraction Discriminator (CFD) into logic pulses that are sent to a time-to-digital converter (TDC) with a 32 μm full scale and a resolution of 500 ps. A computer program reads the data in the form of a time spectrum (a typical example is shown in figure 4.3). The rare gas to be investigated, is injected in the chamber through a high precision valve. The working

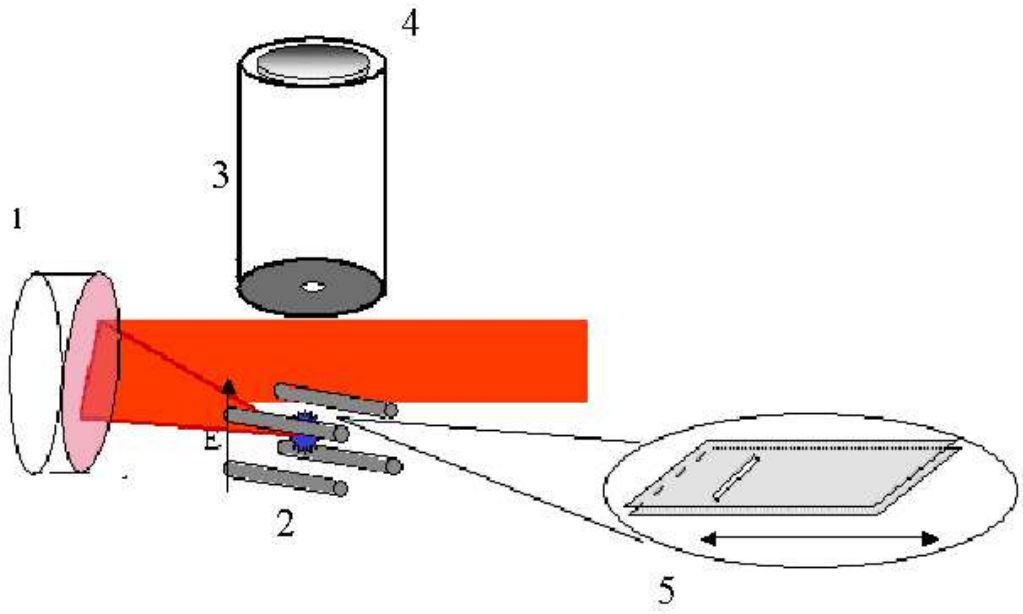

Figure 4.2: Schematic experimental set-up. The laser beam is focused by the off-axis parabolic mirror (1) in the center of a quadruple of equidistant rods (2). An extracting field (E) accelerates the ions through a shielding tube (3) to a Microchannel Plate (4). A slit (5) with an aperture of $300\mu m$ reduces the detection area.

pressure is variable, but it is never higher than 1.0×10^{-7} mbar to avoid space charge effects. The laser intensity regime from 10^{16} W/cm^2 and 10^{18} W/cm^2 is obtained by using the attenuator. This allows for the investigation of intensity dependent ion yields for high charge states for heavy atoms (krypton and xenon). As already mentioned, the measurements are based on TOF spectroscopy. The following section is dedicated to the description of the method for better understanding of the results.

4.2 Principles of TOF-MS

Time-of-flight mass spectrometry (TOF-MS) consists of a separation-in-time of ions generated in the laser focus and accelerated by a constant electric field into a field-free drift region (see figure 4.4). Because the accelerating field is

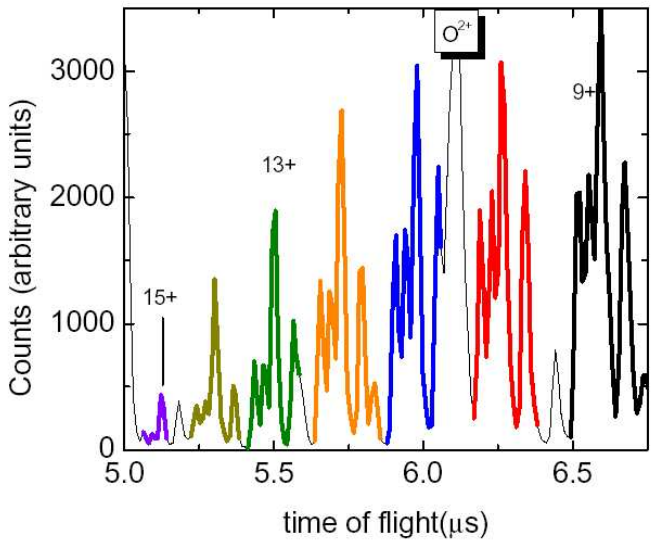

Figure 4.3: TOF spectrum for krypton. The different colors put in evidence the detected charge states from $Z = 9$ (black) to $Z = 15$ (viola).

constant, the velocity of ions depends only on their specific mass-to-charge ratio. The flight time depends on $(\sqrt{q/m})$, so that the ions will travel the same distance to the detector in different times; light and highly charged ions will simply move faster than heavy and low charged ones.

Signal "peaks" arise from ion packets, and the time-of-flight is defined at the peak centroid. The peak width (Δt_{FWHM}) reveals the resolution of the data. A good resolution allows to distinguish the isotopes for every charge state, as visible in figure 4.5. Krypton has four natural isotopes with abundance higher than 10% and in the spectrum all four are distinguishable. The concepts and equations related to mass separation can be developed. Ions are formed, at first, in the ionization region. The acceleration is determined by the Newtons law:

$$\begin{aligned} F &= ma = qE \\ a &= \frac{q}{m}\frac{\Delta V}{d} \end{aligned} \tag{4.1}$$

where ΔV is the extraction potential and d the distance between the plates. Once the ions are in the field-free drift region, they fly with constant velocity

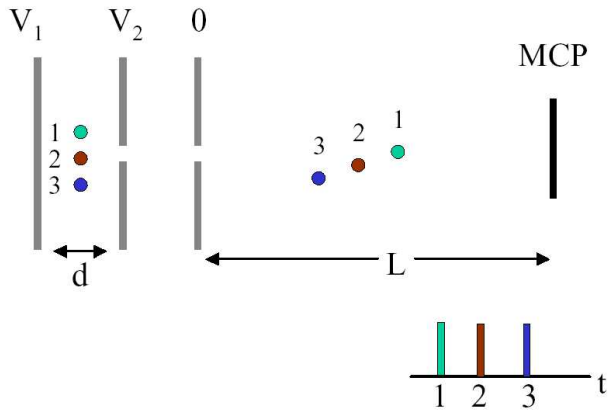

Figure 4.4: Schematic diagram of the time of flight mass spectrometer. Three different charged ions are accelerated with different velocities from the electric field generated between the two plates. The particle with the lowest mass/charge ratio arrives at the detector at an earlier time.

v until they hit the MCP detector. The kinetic energy of the ions is given by:

$$\frac{1}{2}mv^2 = Ze\Delta V; \tag{4.2}$$

the velocity results to be, then:

$$v = \sqrt{\frac{2Ze\Delta V}{m}}. \tag{4.3}$$

Assuming that most of the ion's flight time (t) is spent in the drift tube ($L \gg d$), the time-of-flight can be determined through

$$t = \frac{L}{v} = L\sqrt{\frac{m}{2Ze\Delta V}} \tag{4.4}$$

Rearranging this equation, it provides the conversion of the time-of-flight data into a direct mass-to-charge relation:

$$t = \sqrt{\frac{m}{Z}}\frac{L}{\sqrt{2e\Delta V}} \tag{4.5}$$

Because the dimension of the drift tube (L) and the applied acceleration potential (ΔV) are constants, the $\frac{m}{z}$ ratio and ion identity are determined from the time-of-flight.

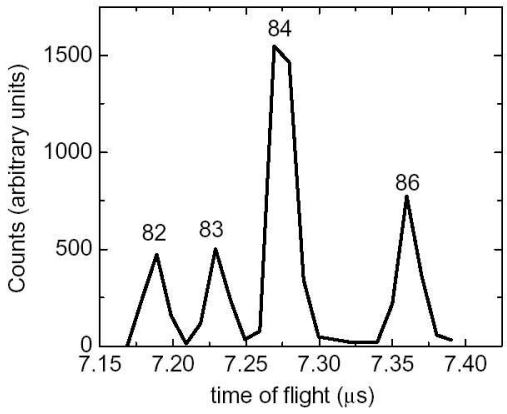

Figure 4.5: Separated isotopes peaks for the Kr^{12+} charge state. The 4 isotopes with the highest natural abundance are clearly separated.

A simulation of the time of flight using the SIMION program, has shown that all the charge states under study acquire a kinetic energy between 15 and 45 keV which lies in the regime of maximum efficiency ($\geq 75\%$) of the detector for positive ions. It has to be noted, however, that the detector efficiency decreases to 50% for higher charge states ($Z \geq 20$) whose kinetic energy becomes higher than 50 keV. Additionally, all the ions located within 1 mm from the focus hit the micro channel plate. A 300 μm aperture limits the focus region and ensures that all the ions are going to be detected.

Laser properties are integral aspects of the ionization process. The intensity of the laser beam is the most obvious feature that affects the ion yield. In addition, the output stability of the laser is crucial. The advances in laser technology have aided quantization and reproducibility, but deviations in the shot-to-shot reproducibility of the laser energy can still be up to 10%.

The ion yield curves as a function of the laser intensity are extrapolated from the integration of the peaks with the higher abundance ($m = 84$ for Kr and $m = 131$ for Xe) of the TOF spectra acquired at different laser energies. For the lowest energy values, the data have been collected over 12500 shots. The energy fluctuation during the acquisition time was estimated to be around $5 - 10$ %.

The measurements with circular polarized light are obtained by introducing in the laser beam a $\lambda/4$ plate with 50 mm diameter. A teflon ring with a 100 mm outer and 40 mm inner diameter was positioned in the beam to

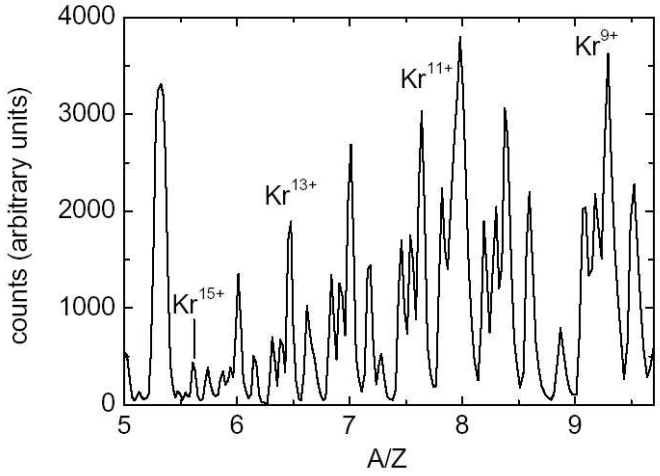

Figure 4.6: m/Z ratio derived from the TOF spectrum. The krypton has $A = 84$ and the different charge states are clearly resolved.

adapt it to the plate. For this reason the energy available for the experiment is reduced to 33% of the total energy.

The data are fitted to the theoretical curves obtained from the ADK theory [65]. Because the calibration of the intensity is constricted by the uncertainty in the focus measurement and by the pulse and energy fluctuations, using the parameters described in chapter 3 ($40fs$ pulse, 8.1 μm waist), the experimental data has to be shifted in the intensity scale by a constant factor $(1.2 - 1.3)$ to fit the theoretical curves.

Chapter 5

Intensity Dependent Yields of Highly Charged Ions

This chapter is dedicated to the discussion of the experimental results obtained for krypton and xenon in the intensity regime between 10^{16} and 10^{18} W/cm^2. Our experiments are focused on intensity dependent ion yields of inner subshells of heavy atoms (krypton and xenon). First of all, we want to scrutinize the validity of the single active electron ionization picture for the highly charged states. In the intensity regime at which ionization of highly charged states takes place, in fact, relativistic effects are no longer negligible. These effects could indeed influence the process not only of single electron ionization, but also of multiple electron ionization.

For the description of the experimental results, we have chosen the ADK theory because, first of all, the tunnelling picture is suitable for the intensity range under study. For field strength higher than 1 a.u. ($I > 3.5 \times 10^{16}$ W/cm^2), in fact, the Keldysh parameter γ is always smaller than unity. Additionally, as already mentioned in chapter 1, relativistic effects do not influence the nonrelativistic tunneling rates for the single electron ionization for intensities below 10^{21} W/cm^2. The electron dynamics responsible for nonsequential ionization, are, in contrast, strongly affected at intensities above 10^{16} W/cm^2.

The first experimental evidence from our group [13] that the nonsequential ionization should be already suppressed at these intensities, was subsequently confirmed by the experimental results on neon discussed by the group of Walker in [15]. In this chapter, we further investigate the ionization behavior of krypton in ultra-intense linear polarized light and we discuss in

more detail the processes which lead to the suppression of the nonsequential (NS) ionization by means of a quantitative estimation of the rescattering probability as a function of the charge states.

The fact that the ionization of the highly charged ions proceeds sequentially, opens a completely new field of study on the behavior of the electrons subjected to a laser field. In fact, if we take a deeper look to the ADK formula (1.20) for the ionization rates, we notice a strong dependency on the magnetic quantum number of the active electron. Several questions arise immediately: what happens to the electrons which belong to a close shell between two ionization steps? do they have time to couple? If this is the case, how does coupling influence the ionization? Or is the ionization so fast that electrons remain in their initial state while they are sequentially stripped out of the core? In addition, one has to take into consideration that besides ionization, the electric and the magnetic field components of the laser light influence the electron orbital states via the Stark and the Zeeman shift respectively. What are the related effects? Our experimental results on the ionization of the electrons in the $3d-$shell of krypton (as well as of xenon) provides the closest possibility to answer all these questions. Based on our experimental results, we could explore the problem if the ionization is faster than the atomic processes leading to fully core relaxation. In the first case, the electrons remain in their initial states while in the second case, the correlation between the remaining electrons (by coupling) is much faster than ionization and sets in before a further electron is stripped out from the ionic core. Such discussion is treated in the last part of the chapter for the $d-$shell of krypton in linearly polarized light.

5.1 Evidence for the suppression of NS ionization

The goal of these investigations was to exclude the possibility of nonsequential ionization at the intensities under consideration. If so, the experiments provide a clear basis for comparison with single active electron theories, such as ADK.

In this section, we investigate krypton and xenon in the intensity range between 10^{16} W/cm^2 and 10^{18} W/cm^2 in linearly and circularly polarized light. We measured the ion yield curves for Kr^{7+} and Kr^{8+} for the lower intensities

(10^{16} W/cm^2 to 10^{17} W/cm^2). For the highest intensities (10^{17} W/cm^2 to 10^{18} W/cm^2), we investigate the charge states $Z = 9$, $Z = 10$ and $Z = 11$ for krypton and $Z = 14$ and $Z = 15$ for xenon. The binding energies of the charge states under investigation are listed in table 5.1. The choice of the charge states is related to the experimental resolution. The time scale where such ions are detected is free from background so that at very low energies the signal to noise ratio is still high enough to produce meaningful results. The experimental results are compared to the ion yields calculated

	Z	7	8	9	10	11	12	13	14	15
Kr	E_b (eV)	111	125.94	230.9	268	318	367	416	465	515
Xe	E_b (eV)	92.1	105.9	171	202	233	263	294	325	358

Table 5.1: Binding energies E_b for krypton and xenon for the charge states under investigation.

using the rates from the ADK theory for sequential ionization at intensities below 10^{16} W/cm^2. Because we still do not have any information about the influence of the initial state of the active electron on the process of ionization, we use for our calculation an averaged value of the ionization rates. In the simulation, the laser pulse is a Gaussian distribution with 40 fs duration. The focus volume is determined by a Gaussian focus waist $\omega_0 \sim 8$ μm and the laser wavelength $\lambda = 815$ nm.

5.1.1 Krypton in linearly polarized light

The data for Kr using linearly polarized light are shown in figure 5.1. The data cover a dynamic range of about 4 orders of magnitude. The sequential ionization picture based on the ADK tunneling rates results in an adequate fit for all the charge states. The deviation of the data from the theoretical curve for Kr^{9+} and Kr^{10+} in the saturation regime is an example of volume effects.

A laser beam can be described as a Gaussian beam propagating along the z direction. Its intensity distribution in space and in time can be described with the formula:

$$I[z,r,t] = I_{peak}\left(\frac{\omega_0}{\omega(z)}\right)^2 \exp\left[-2\left(\frac{r}{\omega(z)}\right)^2\right] \exp\left[-\left(\frac{(t-z/c)^2}{\tau_p^2}\right)\right]. \quad (5.1)$$

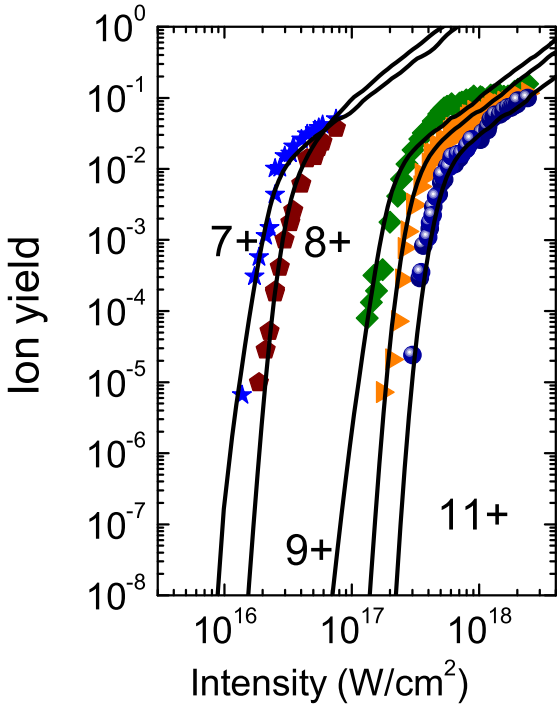

Figure 5.1: Intensity dependent ion yields for: Kr^{7+} (stars) and Kr^{8+} (pentagons), Kr^{9+} (exagons), Kr^{10+} (triangles)and Kr^{11+} (circles) compared with the theoretical curves from the ADK model.

where r describes the radial coordinate perpendicular to the propagation direction x. The beam radius $\omega(x)$ is defined as the radius at which the intensity drops at $1/e^2$. Its minimum value is called focal waist ω_0. The evolution of $\omega(x)$ depends on x and ω_0 as follows:

$$\omega(x) = \omega_0 \sqrt{1 + \left(\frac{x\lambda}{\pi\omega_0^2}\right)^2}. \tag{5.2}$$

Once the maximum intensity of the laser (I_{peak}) is known, it is possible to plot (see fig 5.2) the intensity distribution in a volume expanding along the propagation direction (between $-x$ and $+x$) and radially limited by the

focus diameter (between $-w_0$ and w_0). The volume between two iso-intensity

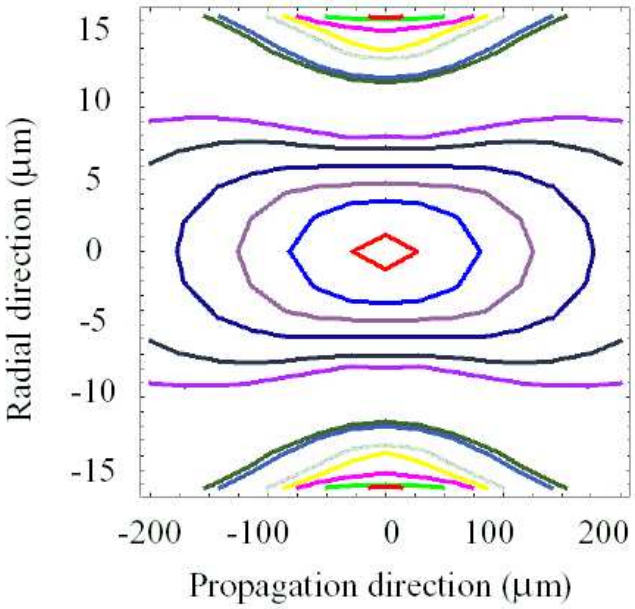

Figure 5.2: Contour plot of the intensity regions where krypton charged states are produced from $Z = 1$ up to $Z = 13$. The contours correspond to the threshold intensities for over-the-barrier ionization 1.15 for the produced charges. On the x axis is reproduced the length of the aperture that is limiting the focus; the y axis corresponds to the focus diameter ($10\mu m$). The volume is calculated for $\lambda = 815$ nm.

shells can be calculated as following [73]:

$$V(I > I_0) = V_0 \left(\frac{2}{9}\xi^3 + \frac{4}{3}\xi - \frac{4}{3}\arctan(\xi) \right) \tag{5.3}$$

where $\xi = \sqrt{I_{peak}/I_0 - 1}$ and $V_0 = 2\pi\omega_0^4/\lambda$. Additionally, if the detection area of the focus region is restricted by an aperture along the laser propagation direction between $-x_i$ and $+x_i$, the collection volume is restricted by these new boundaries as follows:

$$V(I > I_0) = V_0 \left(\frac{2}{9}\zeta^3 + \frac{4}{3}\zeta - \frac{4}{3}\arctan(\zeta) + \left(\frac{\zeta^3}{3} + \zeta \right) \ln\left(\frac{\xi^2 + 1}{\zeta^2 + 1} \right) \right) \tag{5.4}$$

where

$$\zeta = \begin{cases} \xi & \xi < x_i/x_r \\ x_i/x_r & \xi \geq x_i/x_r \end{cases} \tag{5.5}$$

where x_r is the Rayleigh length $\pi\omega_0^2/\lambda$. It defines the radius at which the waist radius becomes $\sqrt{2}\omega_0$. In the simulation used to compute the ion yields, the volumes are calculated using eqn (5.3). This means that the volume where the ions for a specific charge state are produced, grows without any limit along the propagation direction ($x \to \infty$) proportionally to $I^{3/2}$. Thus, an infinite number of ions is available during ionization. In fact, the detection volume is limited by an aperture. This results in a constant number of atoms available in the detection region. In our case, already at intensities below 10^{18} W/cm^2 all the atoms are ionized up to $Z = 9$, so that at higher intensities, the number of the detected ions for this state remains constant.

Looking further to the experimental data, no knee structure is apparent below the saturation intensity. We provide in the following an estimation of the contribution from a nonsequential process on the base of the quasiclassical recollision model (see section 2.1.1). The variable we are interested in is the probability for an electron wave packet to rescatter with its parent ion (from which it was firstly dislodged by laser ionization). The parameters involved in this calculation are the width of the electron wave packet and the cross section for e$-$2e rescattering. It has to be noted that this last parameter describes the rescattering process for an infinitely homogenous incident beam. In our case, we consider a gaussian wave packet to be the incident beam and the rescattering to happen only in a finite area in which the electron density is assumed to be homogeneous. These assumptions do not allow a precise calculation of the rescattering probability but only an estimation of an upper limit. Furthermore, because the magnetic field component is no longer negligible for the laser intensities at which the highest charge states are produced, we will also discuss its influence on the rescattering probability.

Cross section for e$-$2e collisions In the case of krypton the curves of the cross section are measured up to Kr^{18+} [74]. In figure 5.3 the cross sections for Kr^+ and Kr^{13+} are shown as functions of the electrons kinetic energy. We choose to work with the maximum value of the cross section for each charge state. To justify this option, we want to analyze in more detail as an example, the case of recollision with Kr^{6+}. The cross section σ as function of the electron kinetic energy is shown in figure 5.4a), together with the ionization

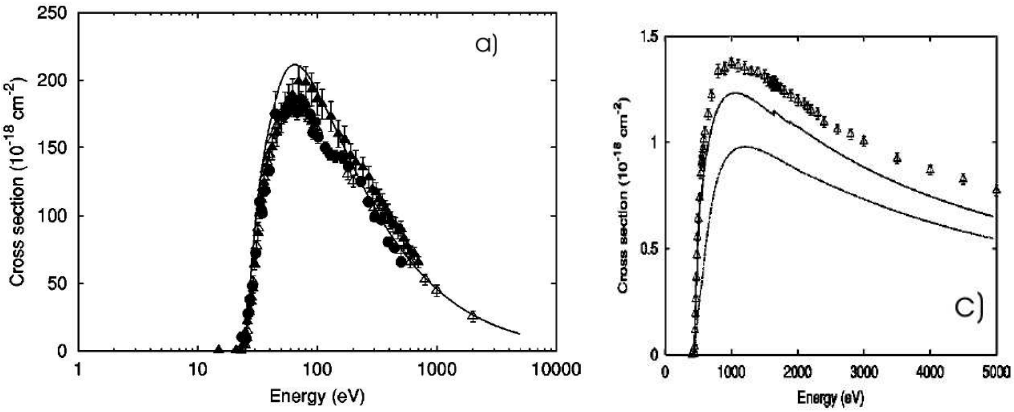

Figure 5.3: Cross-section for electron-ion collision as a function of the energy for a) Kr^{+} and b) Kr^{13+} [74].

probability calculated using the ADK formula (in red). It is visible that when the electron ionize with the highest probability, it acquires kinetic energies which correspond to the highest cross section values ($\sigma_{max} \sim 12\ 10^{-18}\text{cm}^2$ at a kinetic energy $E_{kin} \sim$ 340 eV). Furthermore, as already mentioned in section 2.2, the kinetic energy of the returning electron depends strongly on the laser phase at which the electron is ionized. In figure 5.4b) the kinetic energy for the electron returning to Kr^{6+} are reproduced as a function of the laser phase at an intensity $I = 4.2 \times 10^{15}$ W/cm^2. Here, it is visible that the electron has an energy higher than the 111 eV (dashed line) even at very small phases. If we now assume that the electron is coming back with its maximum energy $3U_p \sim 830$ eV, the cross section would reduce to 1/5 of its maximum ($10 \times 10^{-18}\ cm^2$). The electron-ion recollision probability P estimated using the maximum cross section is then larger than the real one P_{true} ($P > P_{true}$). In figure 5.4c) the maximum value of the cross section is reproduced as a function of the charge state. Inspecting the figure it is clearly visible that the e$-$2e collision cross section decreases with the increase of Z. It is reduced by more than one order of magnitude from Kr^{+} to Kr^{7+} and by more than two to Kr^{15+}.

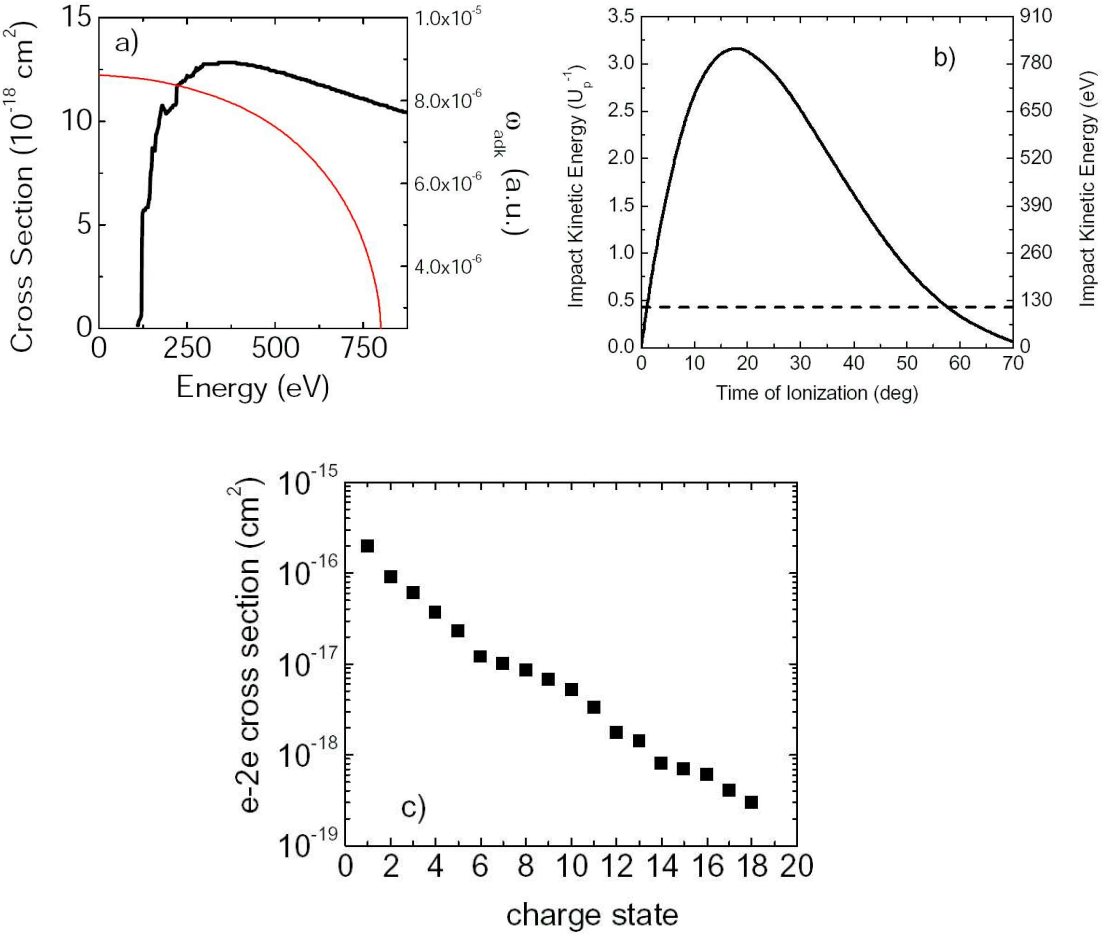

Figure 5.4: a) Cross section for electron-ion collision (in black) and the ADK ionization probability (in red) for Kr^{6+} at a a laser intensity $I = 4.2 \times 10^{15}$ W/cm^2, both as a function of the electrons kinetic energy. b) Impact kinetic energy as a function of the laser phase at which the electron is ionized for the case of the ionization of Kr^{6+} at a laser intensity $I = 4.2 \times 10^{15}$ W/cm^2. c) Maximum of the e$-$2e cross-sections for Kr charge states $Z = 1$ to $Z = 18$.

Electron wave packet At first, we consider the charge of the electron distributed over the whole volume so that (in atomic units)

$$\int_{-\infty}^{+\infty} dx \int_{-\infty}^{+\infty} dy \int_{-\infty}^{+\infty} dz \left(\sqrt{\frac{1}{2\pi\delta^2}}\right)^3 \exp\left(-(x^2+y^2+z^2)/(2\delta^2)\right) = 1. \tag{5.6}$$

However, for the calculation of the rescattering probability we reduce the problem to a two-dimensional system so that we consider only the electron wave packet components along the laser polarization (y) and propagation (x) direction. Because of the symmetry of the system, the behavior of the wave packet is the same in x and y. The electron wave packet is assumed to be a gaussian packet whose width δ_0, at the end of the tunneling ($y_0 = F_0/E_b$), is given by [75]:

$$\delta_0^2 = \hbar^2\kappa/(mF_0) \tag{5.7}$$

where $\kappa = \sqrt{2mE_b}/\hbar$. The packet spreads quadratically in time and the time dependent width is given by

$$\delta(t)^2 = \delta_0^2 + \left[\frac{\hbar t}{m\delta_0}\right]^2. \tag{5.8}$$

As a first step, we treat the system with the magnetic field component of the laser field neglected. Under this condition, as described in section 2.2, the electron is accelerated along the polarization direction (y) from the electric field, returns within half a cycle back to the nucleus, at a time t_r and interacts with the ion core in a head-on collision, as shown schematically in figure 5.5a). Using eqn (5.8), it is possible to calculate the width of the electron wave-packet at the time t_r when it returns to the ion core for every charge state (see figure 5.5b)). Furthermore, we consider that the electron will maximal recollide at t_r. As already mentioned, we assume the rescattering to happen in a finite area $\left(\sqrt{\frac{1}{2\pi\delta(t_r)^2}}\right)^2$ in which the electron density is homogenous. Thus, the calculated rescattering probability P (with $P > P_{true}$) is given by:

$$P = \left(\sqrt{\frac{1}{2\pi\delta(t_r)^2}}\right)^2 \times \sigma \tag{5.9}$$

where σ is the electron-ion cross section. In figure 5.6 (full circles) the rescattering probability P is shown as a function of the ionization state Z of krypton. In the calculations to determine the initial width of the electron wave

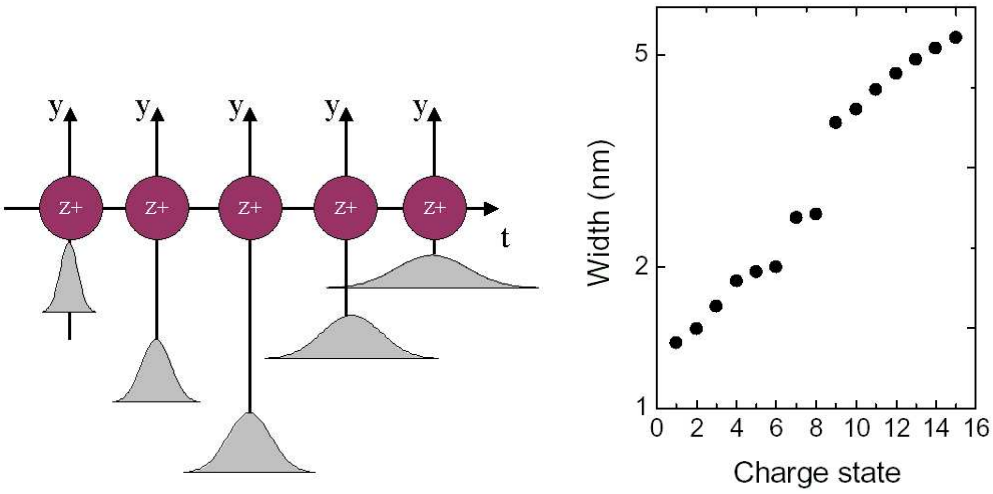

a) b)

Figure 5.5: a) Schematic representation of the trajectory of an electron wave packet uder the influence of an electric field as a function of the time. The wave packet spreads while it returns back to the nucleus. b) Electron wave packet width at the time t_r, when the electron accelerated by the electric field is returning to the core as a function of the charge states.

packet, we choose the electric field strength $F_0 = E_b^2/(4Z)$, which corresponds to the threshold for over-the-barrier ionization. It is visible that P decreases by more than two orders of magnitude ionizing up to $Z = 7$; even more than 4 orders for the highest charge states.

Magnetic field component As already mentioned, the magnetic field component strongly influences the electron dynamics. In fact, it pushes the electron along the laser propagation direction. Within half a cycle, the electron intersects the laser propagation axis at a position x_r different from its initial position immediately after ionization. A consequence of this shift is that a head-on collision between the electron and its parent ion is unlikely, as schematically shown on the right side of figure 5.6and thus, reducing the rescattering probability. For a qualitative analysis, we calculate the returning position x_r for a free electron under the two assumptions described in chapter 2: a) the magnetic field influences the ionization of the charge states under discussion (first order relativistic effects); b) we use a fully relativistic

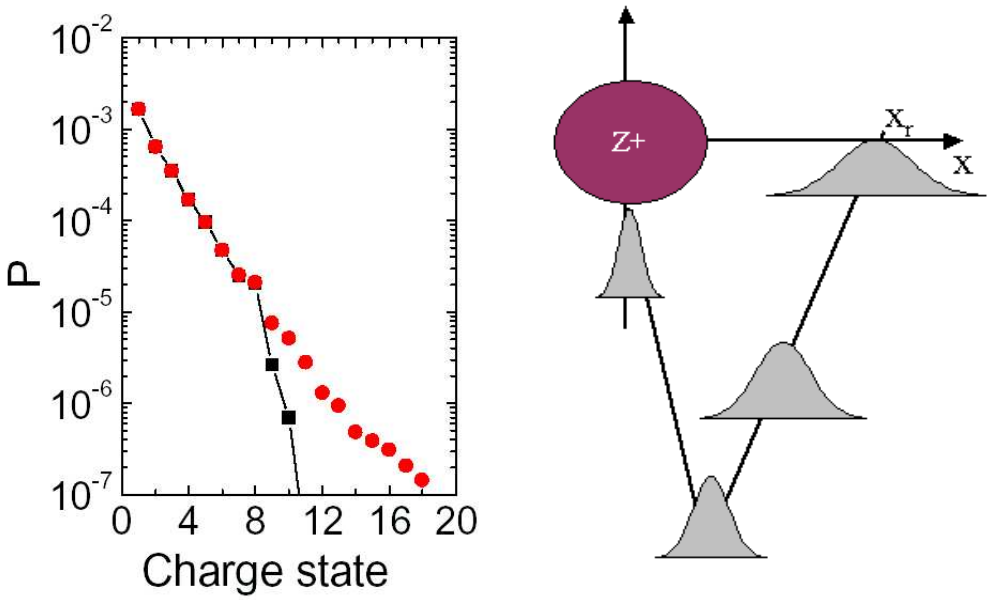

Figure 5.6: On the left: rescattering probability P as a function of charge states of krypton. For the black squares, the magnetic field component is considered, while for the red circles it is neglected. On the right: schematic representation of the collision of a shifted electron wave packet with the ion core under the influence of the magnetic field.

considering the electron rest mass (second order relativistic effects). Besides, we also take into account the presence of the Coulomb potential which could effect the electron motion by refocusing. In figure 5.7a) it is visible that the qualitative behavior of the electron motion is the same in all the descriptions: the electron is ionized and drifts, subjected to the Lorentz force along the laser propagation direction. Within half a cycle, at a time t_r, the electron newly intersects the $x-$axis at x_r. In figure 5.7b) the solutions for x_r for the three models are given as function of the charge state. The laser intensity is fixed to be the threshold intensity $I = I_{th}$ for over-the-barrier ionization. The range is between 10^{14} W/cm^2 to 10^{19} W/cm^2. It is clearly visible that the second order relativistic effects (red circles) set in at very high intensities where charge states with $Z \geq 19$ are ionized. In contrast, the Coulomb focusing (open squares) affects the trajectories for the lowest charge states ($Z \leq 4$). For the intermediate states ($7 \leq Z \leq 19$) the deviations between the three calculations are negligible indicating that the trajectory of the re-

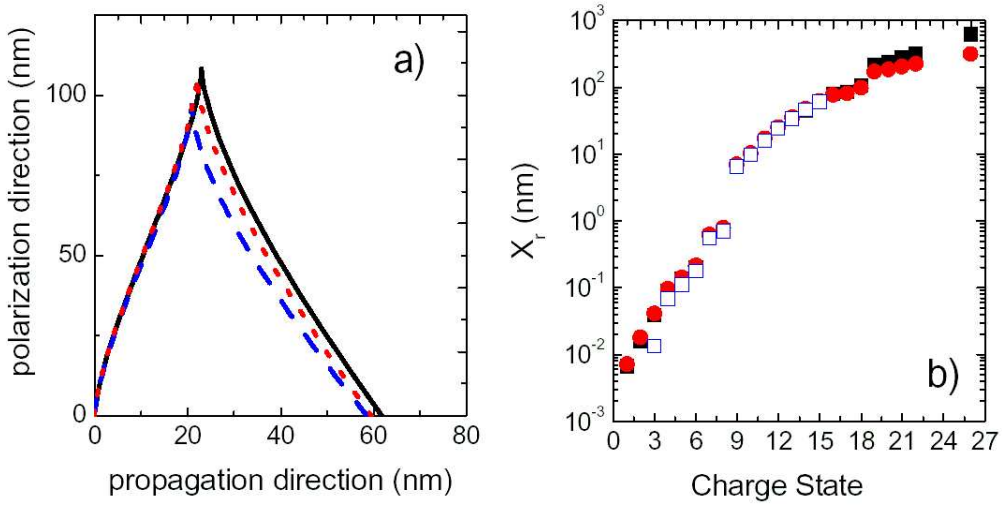

Figure 5.7: a) Electron trajectory from Kr^{15+} in a linearly polarized laser field with $E_0 = 6.0 a.u.$ calculated with three different approaches: fully relativistic treatment (broken line), first order relativstic effects (solid line) and including Coulomb refocusing (dotted line). b) Distance x_r for Kr charge states up to $Z = 26$ calculated with: first order relativstic effects (full squares), fully relativistic treatment (full circles), first order relativstic effects with Coulomb refocusing (open squares).

turning photoelectron is strongly influenced by the magnetic field component of the laser light (full squares). The shift along the laser propagation direction due to the magnetic field becomes larger than 10 nm for charge states with $Z \geq 9$. The returning electron clearly misses the ionic core.

As a consequence, we consider the wave packet function alog the propagation direction to be

$$g(x) = \sqrt{\frac{1}{2\pi\delta(t_r)^2}} \exp\left(-\frac{(x - x_r)^2}{2\delta(t_r)^2}\right) \tag{5.10}$$

In the calculation for the rescattering probability, this results in the fact that the electron is not intersecting the ion at the maximum of its wave packet anymore, but in $g(x = 0)$, where $x = 0$ is the position of the parent ion. Formula (5.9) reads now

$$P' = \left(\sqrt{\frac{1}{2\pi\delta(t_r)^2}}\right)^2 \exp\left(-\frac{x_r^2}{2\delta(t_r)^2}\right) \times \sigma. \tag{5.11}$$

The drift of the electron in laser propagation direction, which sets in for Kr charge states with $Z \geq 8$ causes the rescattering probability to decrease exponentially. This is clearly visible in figure 5.6a) for $Z = 10$ (black squares), where the probability is far below the probability obtained without the magnetic field component. We note that only the rescattering probabilities up to charge state $Z = 10$ fall into the range shown in the figure.

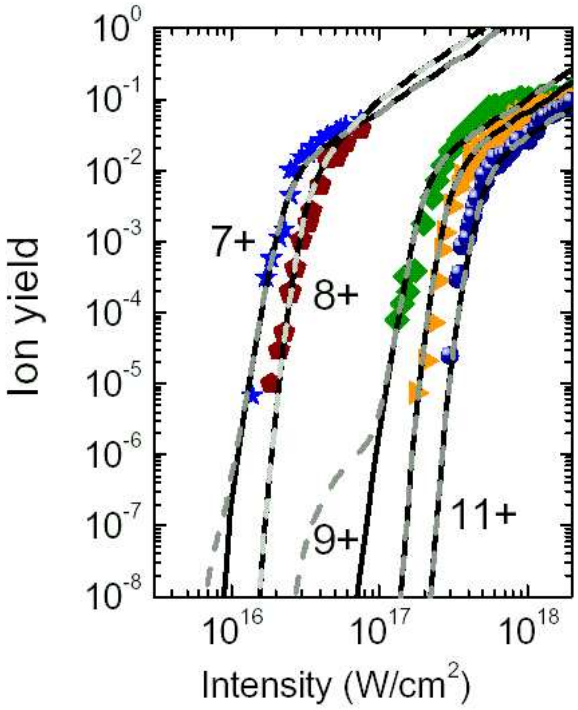

Figure 5.8: Comparison of the experimental yield with the theoretical curves for sequential (solid lines) and for nonsequential (dashed lines) ionization.

Including P' properly in the ionization rates for different charge states, we obtain ion yield curves containing an upper limit, in the frame of the rescattering model, for the nonsequential contribution at least for charge state less than Kr^{10+}. The curves (broken lines) are compared with the data and with the theoretical curves for sequential ionization (straight lines) in figure 5.8. Within the 6 orders of magnitude range of the plotted ion yields, an enhancement due to rescattering is visible only for the states Kr^{7+} and

Kr^{9+}. These states correspond to the first ionization stages of a closed subshell ($4s-$ and $3d-$shell, respectively). The enhancement occurs at intensities well below saturation. Otherwise, influences of the nonsequential process on the ion yield curves lie outside the plotted range. Comparing the theoretical curves to the experimental data we find that the enhancement for the charge states Kr^{7+} and Kr^{9+} lies outside the dynamic range of the experiment.

In conclusion, no effects of rescattering for highly charged states are present. For charge states up to $Z = 8$, this is due to the strong reduction of the e−2e cross section for electron-ion collision and the increasing of the width of the recolliding electron wave packet with the charge state. This is in agreement with the observation of ion yields for lower charge states of Kr, Kr^{+}-Kr^{4+} [33], where the enhancement is indeed visible, but it decreases towards higher charge states. For higher charge states ($Z \geq 9$), the rescattering probability vanishes exponentially due to the influence of the magnetic field component leading to the suppression of the nonsequetial yield enhancement. From this it follows that the sequential ionization picture describes the experimental data very well for all charge states, which is an indirect confirmation of the theoretical results of Milosevic *et al.*, that the tunneling process in the "quasi-relativistic" regime is essentially nonrelativistic. The presence of a strong magnetic field does not influence the single electron ionization itself but rather suppresses the mechanism that leads to multi-electron ionization.

5.1.2 Xenon in linearly polarized light

The experimental results for the charge states $Z = 14$ and $Z = 15$ of xenon are represented in figure 5.9a). The lowest charge states ($Z \leq 11$) are not available because they are already in their saturation region at the intensities at which the experiment is pursued. For the case of xenon too it is possible to estimate qualitatively the NS component to the ion yield. At variance with krypton, the cross sections for the high states of xenon are not known. An estimate is possible using the Lotz formula and the appropriate coefficients [76]. We compare firstly the values obtained by this equation with the measured one for krypton. In figure 5.9b) the maximum values of cross section measured by [74] (squares) are compared with the calculation from the Lotz formula (circles) for charge states with $Z \geq 7$. For high charge states, it is clear that the Lotz formula overestimates the cross section. Thus, we have to keep in mind that the values calculated by this formula for the xenon charge state with $Z = 13$ and $Z = 14$ gives a qualitative but not quantitative

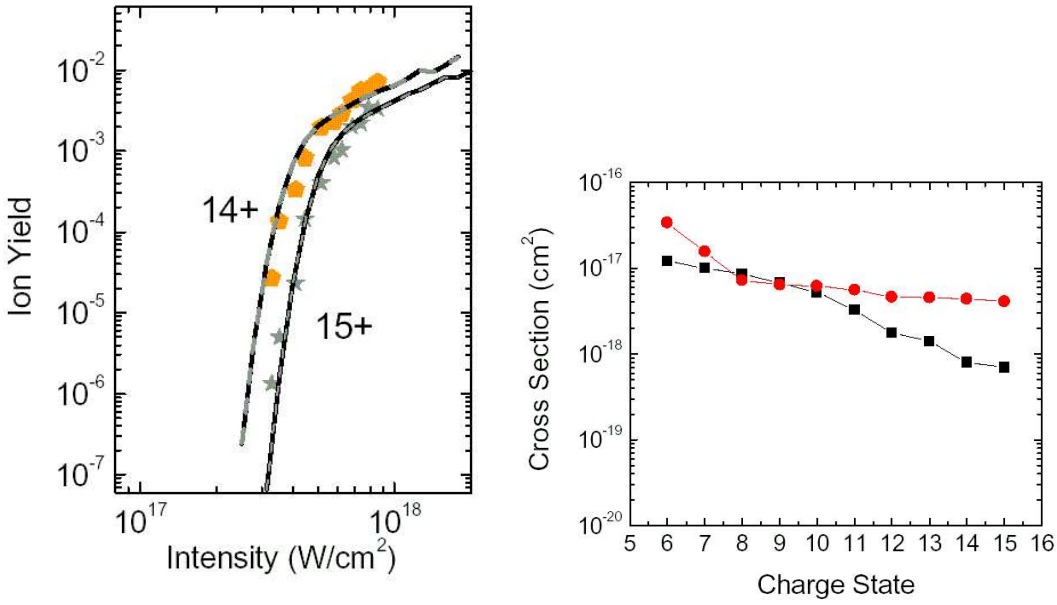

a) b)

Figure 5.9: a) Intensity dependent ion yield for Xe^{14+} (pentagons) and Xe^{15+} (stars). b) The measured (squares) maximum values of the cross section for e−2e collision for several Kr charge states [74] are compared with the calculated values using the Lotz formula [76] (circles).

information of the rescattering component. Moreover, for xenon, the shift induced by the magnetic field on the electron trajectory has to be taken into consideration in calculating the probability for the electron to recollide with the ion. Within the experimental dynamic range no rescattering effect is expected (gray dashed line in figure 5.9a)). The curves for xenon are well approximated by the sequential curves. This is a hint that the influence of the relativistic effects on the ionization processes is independent of the atom species.

5.2 Investigation of core relaxation effects

5.2.1 Ionization of $d-$shell electrons of heavy atoms

The absence of the nonsequential ionization process in the interaction between very high intense laser fields and heavy atoms, opens a completely new field of investigation. The fact that the ionization proceeds sequentially, allows the investigation of the influence of the atomic processes on the ionization. During the ionization of highly charged ions, in fact, the occupation

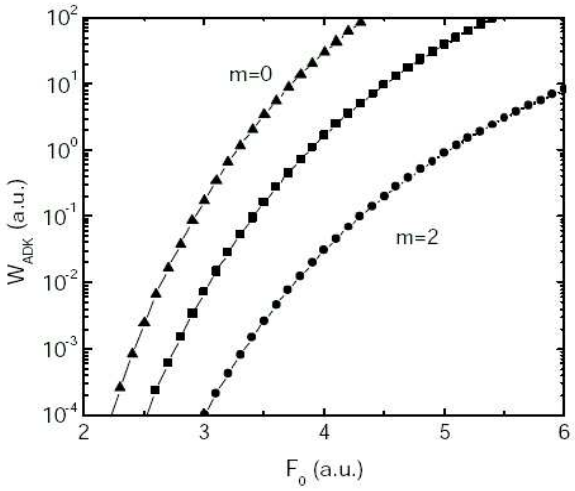

Figure 5.10: ADK model for the ionization rate of the charge state $Z = 15$ as a function of the electric field strength calculated for three different value of the magnetic quantum number m: $m = 0$ (triangles); $m = 1$ (squares) and $m = 2$ (circles).

of m-substates in an atomic subshell acquires importance. The question was brought up and discussed in a recent Letter by Taïeb et al. [77]. The single electron ionization rates (1.20) described by the ADK theory, are strongly dependent on the magnetic quantum number. For an angular momentum of $l = 2$, the ionization rates for the $|m| = 2$ sub-states are typically 3 orders of magnitude lower than for the $m = 0$ sub-states, as visible in figure 5.10 for the Kr charge state with $Z = 15$.

Furthermore, the electrons left in the open shell could rearrange in different groud states configurations due to the LS coupling. The energetic levels

of such configurations differ in a few tens of eV, which correspond to a period which is of the same order of magnitude as the laser period. Thus, it is possible that the ionization and the internal atomic processes compete with each other.

If the time scale at which sequential ionization occurs is faster than the LS coupling, the active electron is supposed to occupy its initial state during ionization. The process would proceed with the dependence on the magnetic quantum numbers. Hence, it should be expected that the $m = 0$ substates ionize first, while the remaining electrons ionize only at substantially higher field strengths. In contrast, if the atomic processes are faster than ionization, the remaining electrons are supposed to couple with each other. Additionally, it has to be considered that besides ionization, the magnetic field component of the laser light influences the electron orbital states via the Zeeman shift which could give also a contribution to a relaxation of the ionic core. Thus, a "mixing" of the initial m-states has to be taken into account in the calculation of the ionization probability.

The ionization of the electrons in the $3d-$shell of krypton (as well as of xenon) provides the most adequate possibility to find an answer to these questions. On the basis of the experimental results, in fact, it can be understood whether the ionization is faster than the atomic processes or if between two ionization steps, the ionic core "relaxes". In the following we discuss these topics on the basis of the experimental results.

To describe the overall ionization process we start from the neutral Kr atom. The first eight electrons of Kr ionize at relatively low laser intensities (below $10^{16} W/cm^2$). The next available electrons emerge from the closed $d-$subshell and require a laser intensity about a factor of ten higher than necessary for the first 8 electrons. After the ionization of the first eight electrons there is time (several laser cycles) for the core to relax to the spherical singlet state before the ionization of the d-shell sets in. Consequently, details of the underlying ionization mechanism of the initial 8 electrons do not have any effect on the following discussion.

In order to apply the ADK formula we need to fix the m-quantum number for each electron in the subshell. At first, the magnetic quantum number m is taken with respect to the electric field vector as quantization axis. The ten electrons occupy the available $m-$quantum states as required by the Pauli principle, i.e. 2 electrons are in the $m = 0$, 4 are respectively in the $|m| = 1$ and $|m| = 2$ substate. Within the laser pulse, the ionization of the $m = 0$ states is the most probable, followed by the $m = 1$ components and finally by

the $m = 2$ components. If we suppose that no reorientation of the m-quantum numbers happens during sequential ionization, the electrons remain in their initial state, keeping their initial $m-$quantum number. Consequently, the last 4 electrons in the shell should ionize at a substantially lower rate. On the other hand, if the reorientation is faster than ionization, we can expect for each electron to occupy the magnetic quantum numbers statistically.

In the absence of a clear theoretical prediction for the time scale of the reorientation we have chosen to compare our results with two limiting cases. In the first case, the reorientation is fast, which means the LS coupling of the remaining electrons takes place as soon as the subshell is no longer closed. As an example, we describe a two-electron system in a $l-$shell. Both electrons have the orbital quantum number $l_1 = l_2 = l$ and they have equal probability to have a magnetic number $m_{1,2} = -1, 0, 1$. When they are correlated, the total angular momentum is $\mathbf{L} =\mid l_1 - l_2 \mid, .., \mid l_1 + l_2 \mid$. Using the Clebsch-Gordan coefficients ($< l_1, l_2, m_1, m_2 | L, M >$) [78], it is possible to calculate the new states that the coupled electrons can occupy as

$$|LM >= \Sigma_{m_1 m_2} < l_1, l_2, m_1, m_2 | L, M > |l_1, m_1 > |l_2, m_2 > . \tag{5.12}$$

As a result one has a system of states with $L = 0, 1, 2$ combination of the states for the single electrons. The state $L = 0, M = 0$, for example, is given by

$$|0, 0 >= 1/\sqrt{3}|1, -1 > |1, 1 > +1/\sqrt{3}|1, 1 > |1, -1 > -1/\sqrt{3}|1, 0 > |1, 0 > . \tag{5.13}$$

It is clearly visible that due to the correlation between the two electrons, the new state occupied by the total system is a combination of the initial m quantum numbers. This results in ionization rates which are statistically averaged over the available m-quantum numbers [26]:

$$\omega = \left(\sum_{i=0}^{2} \omega_i \right) / (2l + 1) \tag{5.14}$$

where ω_i is the ADK rate calculate for each m substate (for a d-shell $i = 0, 1, 2$) and l is the angular momentum.

For the opposite case of slow reorientation, the first two electrons of the d-shell ionize with the $m = 0$ rate, the next four with the $m = 1$ rate and

the last four with the $m = 2$ rate:

$$w = (q \times w_0 + k \times w_1 + j \times w_2) \qquad \begin{array}{lcl} Z = 9 & \Rightarrow & q = 2, k = 4, j = 4 \\ Z = 10 & \Rightarrow & q = 1, k = 4, j = 4 \\ Z = 11 & \Rightarrow & q = 0, k = 4, j = 4 \\ . & & \\ Z = 13 & \Rightarrow & q = 0, k = 2, j = 4 \\ . & & \\ Z = 15 & \Rightarrow & q = 0, k = 0, j = 4 \\ . & & \end{array} \tag{5.15}$$

In figure 5.11 are shown the ion yields for three charge states which have different m quantum numbers calculated using the two different ionization probabilities. For both cases, the ionization behavior of the first electrons ($Z = 10$ in the figure) in a $m = 0$ substate is very similar and leads to the same ion yield curves. When the most probable m-substates are already

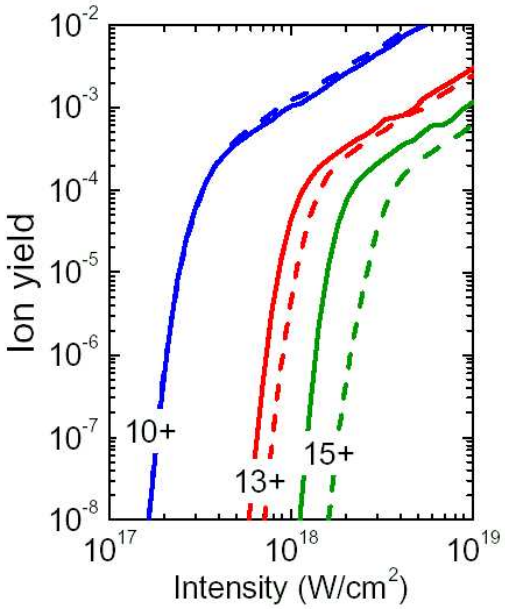

Figure 5.11: Comparison between the $m-$dependent (dashed) and the over all the m averaged ion yield curves (solid) for Kr^{10+} (blue), Kr^{13+} (red) and Kr^{15+} (green).

ionized, the two methods result in strongly different ion yields for the residual

electrons in the subshell being in $m = 1$ and $m = 2$. We note that the difference between the two cases does not depend on an absolute intensity determination. Rather, it shows up as a relative shift between the ion yields for different charge states. For the highest charge states ($Z = 15$ in the figure), the "slow" reorientation leads to ion yields (dashed lines) that are $2 - 3$ orders of magnitude smaller than for the "fast" reorientation (solid lines).

In the following, we compare the experimental data with the curves resulting from the m-dependent (dashed lines) and the averaged rates (solid lines) in figure 5.12. In the case of $Z = 9$ and $Z = 10$ both models fit the

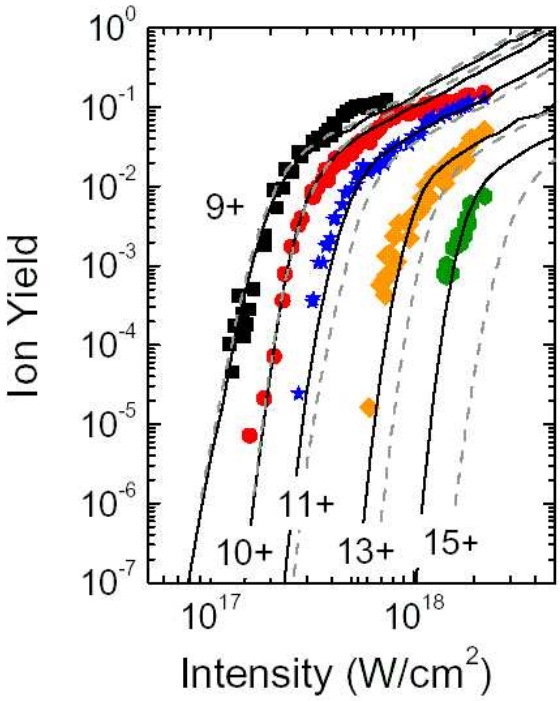

Figure 5.12: Intensity dependent ion yield for Kr^{9+} (squares), Kr^{10+} (circles), Kr^{11+} (triangles), Kr^{13+} (diamonds) and Kr^{15+} (stars). The charge states correspond to the ionization of the $d - shell$ of krypton. The theoretical yield curves are calculated taking into account the $m-$ dependence of the ionization rates (dashed lines) and averaging the rates over all the m-states (solid lines).

data very well. However, for the calculation which describes the slow reorientation, a difference of one order of magnitude is observable already for

the next charge states ($Z = 11$ and $Z = 13$). For the highest charge state ($Z = 15$), the difference is increased up to three orders of magnitude. As a matter of fact, the set of curves calculated averaging over all the m states matches the data very well.

To confirm the results obtained for krypton, we investigate also the d-shell ionization for xenon. The binding energies of Xe are lower than for Kr. In the intensity regime between 10^{17} and 10^{18} W/cm^2 it was possible to detect charge states between $Z = 12$ and $Z = 17$. Thus, we have the possibility to verify the fast reorientation theory, comparing directly states from $m = 1$ (Kr^{12+} and Kr^{14+}) and $m = 2$ (Kr^{15+}, Kr^{16+} and Kr^{17+}). In figure 5.13 the two models are compared. As for the case of krypton, already for the

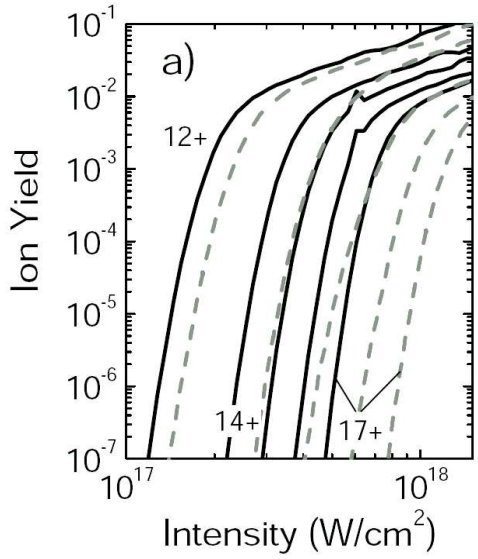

Figure 5.13: Comparison between the $m-$dependent (dashed) and the over all the m averaged ion yield curves (solid) for Xe charge states with $Z = 12, 14, 15, 16$ and $Z = 17$. On the bottom: Intensity dependent ion yields for Xe^{12+} (pentagons), Xe^{14+} (squares), Xe^{15+} (circles), Xe^{16+} (triangles) and Xe^{17+} (stars). The charge states correspond to the ionization of the $d-$*shell* of xenon.

first charge state, the difference between the "fast" (solid lines) and "slow" (dashed lines) reorientation is more than one order of magnitude. This gap is increasing with the charge states. For the electrons with $m = 2$, the difference rises to more than 3 orders of magnitude. Now, in figure 5.14b) and c) the data are compared with the curves from the two models, respectively.

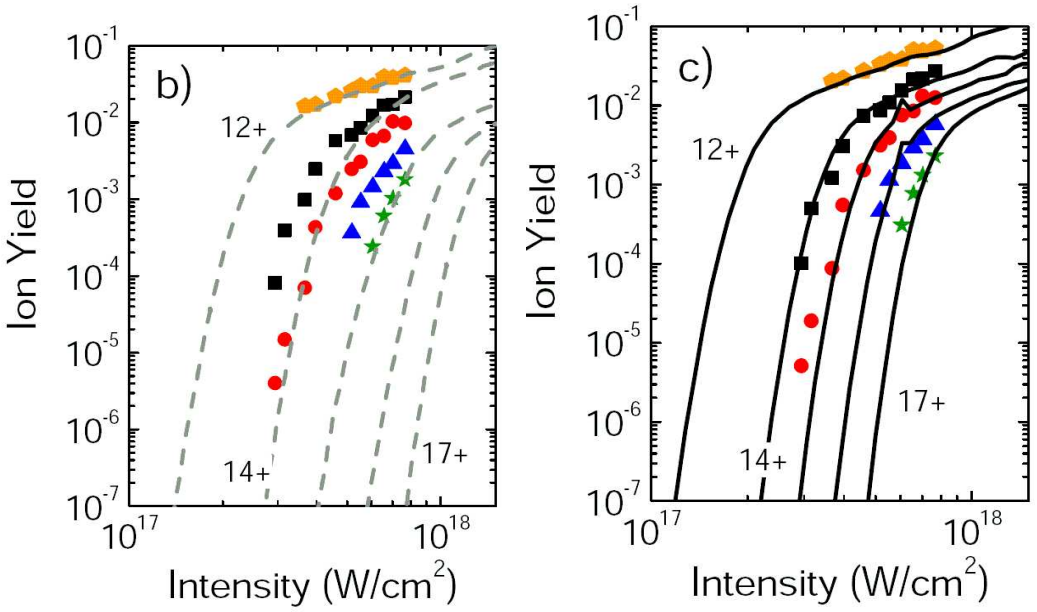

Figure 5.14: b) The theoretical yield curves are calculated taking into account the $m-$dependence of the ionization rates (dashed lines); c) the rates are averaged over all the m-states (solid lines).

In figure 5.14b), we fit the data for Xe^{12+} to the correspondent curve. It is already visible that the charge state with $Z = 14$ which corresponds to a $m = 1$ electron, agrees with the theory only in the saturation regime. The yields for the $m = 2$ electrons are orders of magnitude higher than it would be expected if the electron would remain in the initial m state. Again, the whole set of data is very well described by the calculations which take into account m averaged ionization rates as shown in figure 5.14c).

This clearly indicates that the reorientation of the m-states is fast. Apparently, the core fully relaxes between two successive ionization steps. A further process could be involved in the core relaxation. In the interaction with an electromagnetic field, besides ionization, the active electron is subjected to the action of orthogonal fields. The electric field component determines the axis along which the orbital angular momentum $\mathbf{L}$ of the system precesses. We decide to change our notations so that the precession axis, together with the electric field direction, are now along the $z-$axis. The electric field acts

on the energy level $|lm>$ by a tensorial Stark shift given by [79]:

$$E_{st}(l,m)|LM>= -\left(\alpha_0 + \alpha_2 \frac{3m^2 - l(l+1)}{l(2l-1)}\right) F_0^2 |lm>, \tag{5.16}$$

where α_0 and α_2 are the scalar and the tensor polarizability respectively and F_0 the field amplitude. At the same time, the magnetic field component (which will be no longer B_z, but B_x, as shown in figure 5.15), acts on the system with a Zeeman shift $\mathbf{E_{Zee}} = -0.5\mathbf{B}\cdot\mathbf{L}$. The scalar product has only the

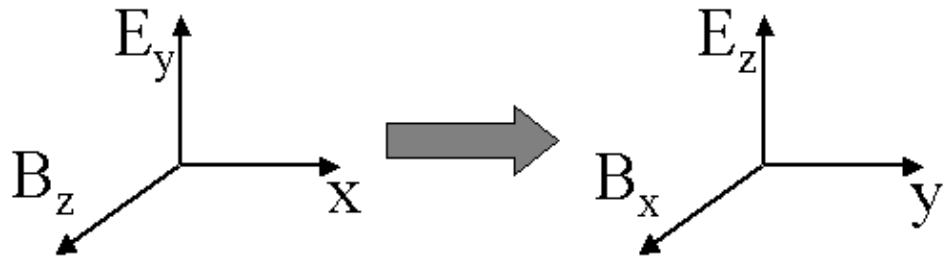

Figure 5.15: Change of the axis notation to the standard notation for description of the angular momentum.

component $E_{Zee} = -0.5 B_x L_x$. It is possible to calculate the eigenvalues and the eigenvectors which are the solutions of the Hamiltonian which describes the orthogonal fields ($\mathbf{H} = \mathbf{E_{Zee}} + \mathbf{E_{st}}$) using the matrix representation of angular momentum operators [78]. By introducing the raising and lowering operators

$$L_\pm = L_x \pm L_y \tag{5.17}$$

such that

$$L_\pm |lm>= \hbar \left[l(l+1) - m(m\pm 1)\right]^{1/2} |lm \pm 1>, \tag{5.18}$$

where $|lm>$ and $|lm \pm 1>$ are the initial and final state respectively, the component L_x can be written as

$$L_x = L_+ + L_-. \tag{5.19}$$

For simplicity, we solve the matrix form of the Hamiltonian for the case of a $l = 1$ shell, where the magnetic quantum number m varies from -1 to 1:

$$\begin{pmatrix} E_{st}(1,-1) & \hbar\sqrt{2}B_x & 0 \\ \hbar\sqrt{2}B_x & E_{st}(1,0) & \sqrt{2}\hbar B_x \\ 0 & \hbar\sqrt{2}B_x & E_{st}(1,1) \end{pmatrix}$$

The eigenvectors of such a Hamiltonian are now field dependent:

$$\left\{ \left(1, -\frac{-3\alpha_2 cF_0 + \sqrt{64 + 9\alpha_2^2 c^2 F_0^2}}{4\sqrt{2}}, 1\right), (-1,0,1), \left(1, \frac{3\alpha_2 cF_0 + \sqrt{64 + 9\alpha_2^2 c^2 F_0^2}}{4\sqrt{2}}, 1\right) \right\}. \tag{5.20}$$

The eigenvalues are field dependent as well, as is visible in figure 5.16a). It

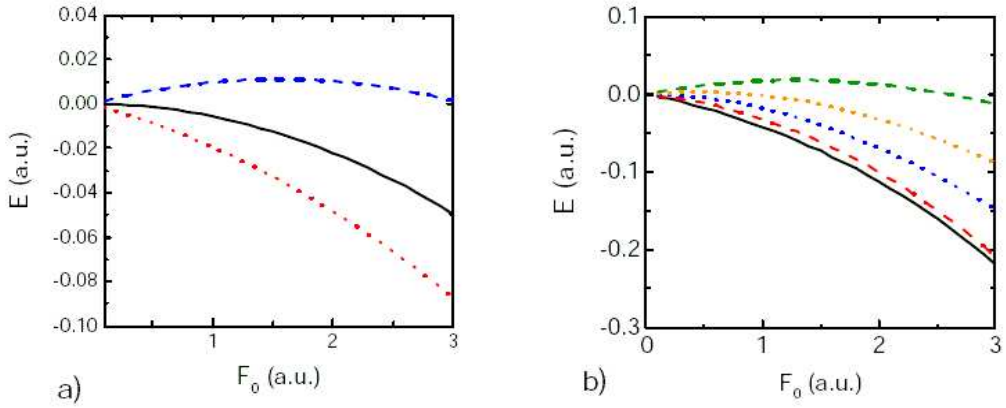

Figure 5.16: Eigenvalues of the Hamiltonian describing the energy levels of an electron with angular momentum a) $l = 1$, b) $l = 2$ in an electromagnetic field as a function of the laser field. In the calculation $\alpha_1 = 0.01$ a.u. and $\alpha_2 = 0.001$ a.u.

can be seen that the behavior of the energy levels proceeds linearly, due to the Zeeman effect, only for very weak fields ($F_0 < 1$ a.u.), while with the increasing of the field amplitude, the levels change quadratically with the

Stark effect. The energy levels of the ionic core rearrange into a state $|LM>$ which is a combination of the initial magnetic quantum numbers m, under the simultaneous action of an electric and magnetic field. The same concept is valid for the electrons in a $d-$shell. The energy levels of the electrons with $l = 2$ as a function of the laser field strength are shown in figure 5.16b).

If we assume that the typical time scale for these processes is connected to the electron motion in the atomic orbital, it results in the order of magnitude of a few tens of attoseconds. In table 5.2 are listed the precession times, expressed in fs, as a function of the charge states for $7 < Z < 15$. The atomic

Z	7	8	9	10	11	12	13	14	15
t (fs)	0.046	0.043	0.020	0.017	0.015	0.013	0.012	0.011	0.010

Table 5.2: List of the precession times for Kr charge states with $7 < Z < 15$.

processes are, then, much faster than the ionization in a 40 fs laser pulse. In

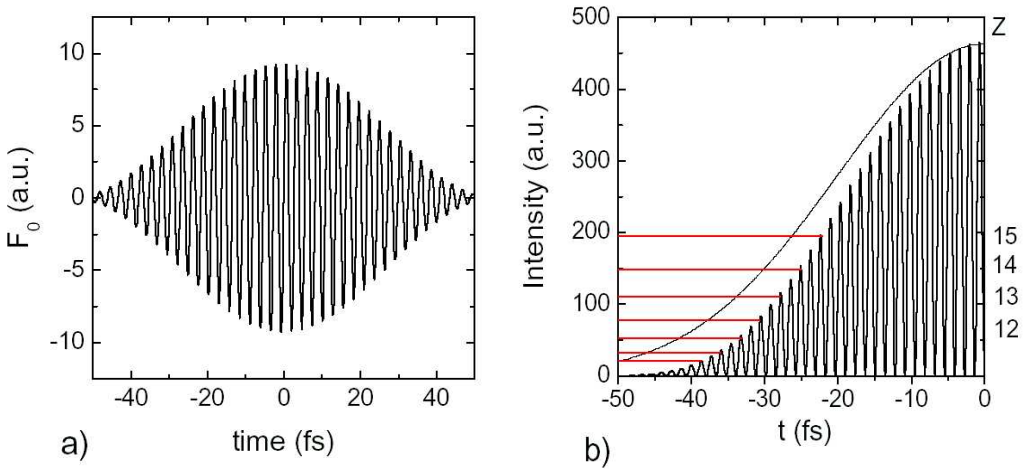

Figure 5.17: a) Field strength for a laser beam with $\omega = 0.056$a.u. and a pulse width $\Delta t = 40 fs$. A laser period corresponds to $\tau = 2.7$ fs b) Rising edge of the laser intensity together with the threshold intensity for over-the-barrier ionization for the Kr charge states with $9 < Z < 15$.

fact, if we represent the laser intensity as in figure 5.17b), it is clearly visible that if we suppose that the ionization proceeds at the threshold intensity for over-the-barrier, each charge state is generated near the maximum of each

laser cycle τ ($\tau = 2.7$ fs). The time scale at which ionization proceeds is two times larger than the time at which the atomic processes occurs. Between two ionization steps, both the electron correlation and the action of an electromagnetic field cause a reorentation of the substate occupied by the active electron. This leads to the necessity to treat the ionization probability for each electron statistically.

5.2.2 LS coupling of ground state configurations

As already mentioned in the previous section, the LS coupling of the electrons left in the open $d-$shell causes the ionic core to relax between two ionization steps. Furthermore, it could cause the electrons left in the open shell, to rearrange in different groud state configurations. The energetic levels of such configurations can differ in a few tens of eV, as shown in table 5.3.

Z	Outer Subshell		Binding energy (eV)
7	$4s^2$	^{1}S	106.8
8	4s	^{2}S	124.57
9	$3d^{10}$	^{1}S	231.74
10	$3d^9$	$^2D_{1/2}$	267.10
		$^2D_{3/2}$	265.8
11	$3d^8$	^{3}F	306.80
		^{1}S	291.41
13	$3d^6$	^{5}D	388.41
		^{1}S	374.81
15	$3d^4$	^{5}D	348.43
		^{1}S	341.63

Table 5.3: Electronic configuration and binding energies of the $4s-$ and $3d$-shells of krypton. Only the lowest and the highest configuration are considered.

In a recent paper [80], Kornev et al have discussed the possibility that, after the tunneling of the first electron of a $p-$shell, the remaining electrons can couple to a ground state configuration which leads the active electron to be energetically less bound (inelastic tunneling). In this model, the probabilities for multiple ionization of Ar and Kr atoms in circularly polarized light have

been calculated taking into account the different ground state configurations due to the LS coupling as ionization channel in addition to the sequential and nonsequential processes. This leads the yields of the highest charged states (Kr^{2+} to Kr^{6+}) to shift towards lower intensities in comparison with the pure ADK theory.

Because the ionization $d-$shell electrons proceeds sequentially, it is possible to investigate the influence of the inelastic tunneling on ionization also in linearly polarized light. In figure 5.18, we have compared the experimental results for charge states from Kr^{9+} to Kr^{15+} with two simplified cases.

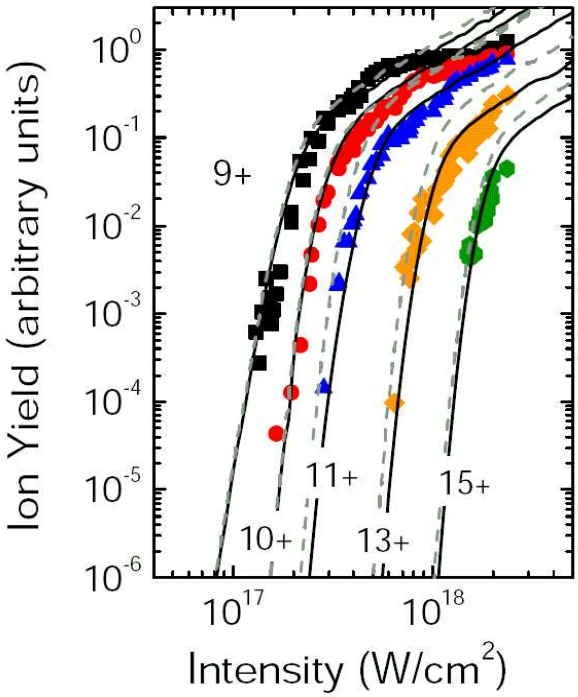

Figure 5.18: Intensity dependent ion yields for Kr^{9+} (squares) and Kr^{10+} (circles), Kr^{11+} (triangles), Kr^{13+} (diamonds) and Kr^{15+} (exagons) with linearly polarized light. The data are compared with the theoretical curves calculated for the ground state (solid) and for the LS coupling ground state configuration which leads the lowest binding energy for the active electron (dashed).

In the first case, during ionization, the electrons are supposed to occupy the ionic ground state (solid lines). In the second case, we take into con-

sideration a ground state configuration due to the LS coupling which leads the electron to be less bound (dashed lines). The ion yields calculation is performed by taking into consideration different binding energies in the calculation of the ionization rates. The energetic difference of each configuration from the ground state is calculated with Hartree-Fock [81]. The binding energies of the ground state are taken from [82]. The intensity dependent ion yields curve for Kr^{9+} is the same in both the calculations. This charge state is, in fact, generated by dislodging the first electron of the closed $d-$shell, for which only a single configuration is expected (see table 5.3). For the highest charge states ($11 \leq Z \leq 15$), the ground state presents several electronic configurations. In our calculation we take into account only the configuration which leads to the lowest binding energy.

As previously discussed by Kornev et al., the LS coupling leads to a shift towards lower intensities in the ion yields of the charge states Kr^{11+} to Kr^{15+}. Because the difference between the binding energies of the two ground state configurations is only a few tens of eV, this shift is not very prominent. Thus, the curves lie within the experimental error bars for the highest charges ($Z \geq 11$).

Krypton in circularly polarized light In the same intensity regime, we have also investigated the ionization mechanisms with circularly polarized light. It is the first time that intensity dependent ion yields has been measured for highly charged ions generated in the interaction of femtosecond circularly polarized laser pulses with heavy atomic species. The data are compared with the theoretical curves using the averaged ADK rates (1.3).

The differences between the yields for linear and circular polarization are typically a factor of two. The tunneling rates for circular polarization are higher than for the linear one (see figure 5.19a)). Since the field strength amplitude in circularly polarized light is constant, the circular rate remains constant over the whole optical cycle. However, for a given laser intensity, the peak electric field of circularly polarized light is smaller by a factor of $\sqrt{2}$ than that of a linear polarized light. These two factors lead to an appearance intensity for circular polarization higher than for linear polarization (see figure 5.19b)). Because our experiment does not involve an absolute measurement of the ion yields, we cannot further investigate this intensity shift.

Up to now, experimental data on ionization in circularly polarized light

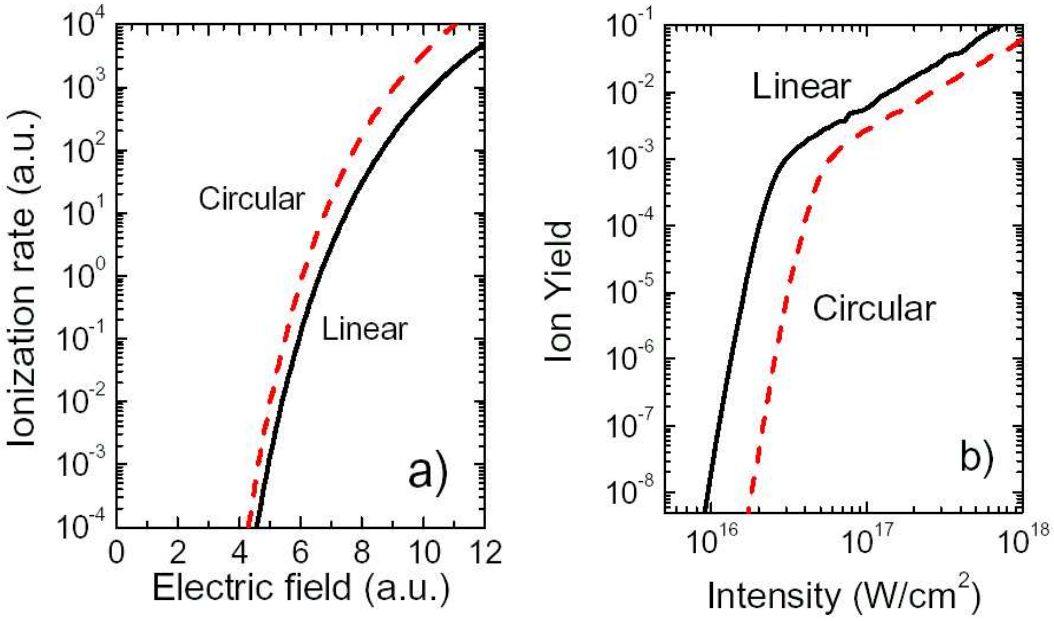

Figure 5.19: a) Ionization rates as a function of the field strength; b) intensity dependent ion yield for circular (red dashed line) and linear (black straight line) polarization

have been presented for low charge states under long pulse durations ($\geq$ 100 fs) and high laser frequencies [14, 36, 31]. In all cases, the enhancement due to a nonsequential ionization process was not present for the doubly charged ion yield. This confirmed the validity of the quasistatic model supporting the picture of a rescattering mechanism as responsible for nonsequential ionization.

Also in this case, we compare the experimental data with two different set of curves, to investigate the influence of the LS coupling in circular polarization. It is visible in figure 5.20 that the experimental data are well described by the sequential tunneling ionization picture based on the ADK tunneling rates for circularly polarized light for all charge states. In particular, the charge states Kr^{7+} (stars) and Kr^{8+} (pentagons) show very good agreement in the saturation regime where it is expected that the ionization of Kr^{8+} occurs before the yield of the previous charge state reaches the saturation. Because the difference between the binding energies of the ground state and the excited state is only a few tens of eV, the shift towards low intensities due to the core excitation is not very prominent. As for the data obtained

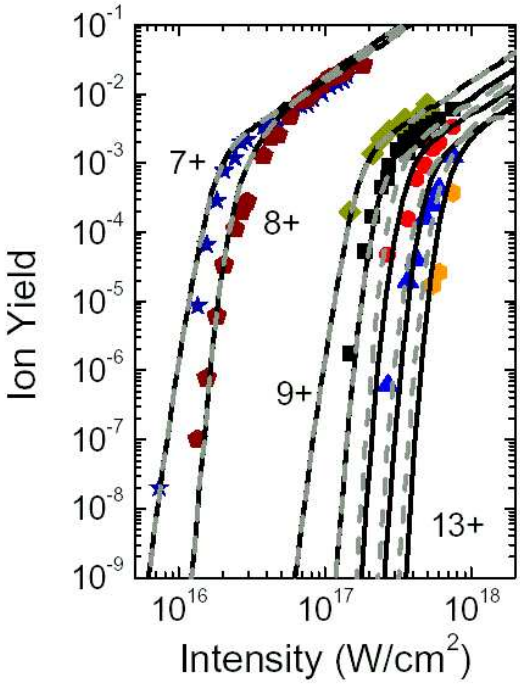

Figure 5.20: Intensity dependent ion yields for Kr^{9+} (stars) and Kr^{10+} (pentagons), Kr^{11+} (circles), Kr^{13+} (exagons) and Kr^{15+} (diamonds) with circularly polarized light. The data are compared with the theoretical curves calculated for the ground state configuration for the highest (solid) and the lowest (dashed) LS coupling.

with linearly polarized light, the two set of curves lie within the experimental error bars.

The measurements of the highly charged states ($Z = 9$ to $Z = 13$) turned out to be the most sensitive to the background conditions during the experiment. In figure 5.21 are shown, as an example, two independent measurements of the time of flight spectrum at a constant energy (ca. 90 mJ). A comparison between the spectra in figure 5.21a) and in figure 5.21b) shows that the peak corresponding to the isotope $m = 84$ for the highest observable charge state is much broader in the second case than in the first one. This is an indication of a possible enhancement of the ion number due to background signals. Thus, the experimental points could be acquired for the different charge states only where the spectrum did not show any noise signal.

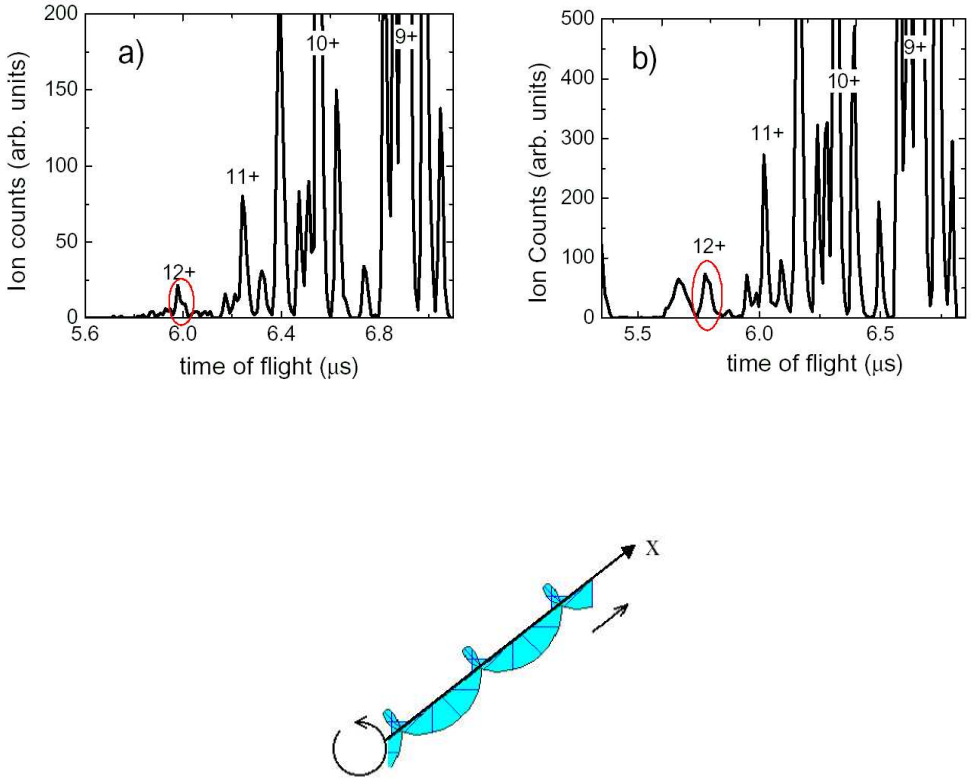

Figure 5.21: On the top: Time of flight spectrum for two independent measurements of Kr in circularly polarized light at a laser energy of ca 90 mJ. On the bottom: An electron in a circularly polarized light moves in an elliptical trajectory around the laser propagation axis x without ever crossing it.

In conclusion, the sequential ionization described by the ADK rates for circular polarization is a very good approximation for the results. In this case, however, the agreement between the results and the theory is not related to the suppression of the rescattering process due to relativistic effects as for linearly polarized light. In a circularly polarized wave, in fact, the polarization vector rotates in the plane perpendicular to the laser propagation direction (see figure 5.21). This rotation influences the motion of the electron which moves circularly in the plane perpendicular to the laser propagation direction without ever crossing it. Any recollision with the parent ion is impossible. As previously mentioned, such processes were also observed at

nonrelativistic intensities for low charge states. The observation of the same behavior for high charged states confirms the validity of this description.

Chapter 6

Ionization dynamics as laser intensity probe

Is it possible to use the ionization dynamics for laser intensity diagnostics? As described in chapter 3, to determine the laser intensity it is necessary to know three parameters individually : energy E_L, pulse width τ and focus waist ω_0. When the intensity increases up to 10^{19} W/cm^2, the last one in particular is not possible to be measured directly. The optical elements would not survive the laser energy. An important issue which is of high interest for the whole laser community, concerns the possibility to find new methods to characterize TW laser systems in a more direct way. Because the intensity characterises such systems, the main attempt is to search for a method to measure directly the intensity without relying on the laser parameters. Thus, the diagnostic of the intensity is not influenced by the separate measurements of pulse duration, beam waist or laser energy. In the next section the possibility to use atomic ionization dynamics as a probe of the laser intensity will be discussed.

6.1 Over-the-barrier ionization as an intensity probe

In chapter 1 it was mentioned that for very strong laser fields, the Coulomb potential can be bent so that its saddle point lies below the binding energy of the active electron. The probability that the electron leaves the atom is then very high. The intensity threshold between tunneling and over-the-barrier

ionization is defined as

$$I_{th} = 1/2c\epsilon_0 \frac{E_b^4}{16Z^2} \tag{6.1}$$

where c is the speed of light, ϵ_0 the permittivity in vacuum, E_b and Z the binding energy and the charge state of the active electron respectively. For a specific laser frequency, it depends only on the electron binding energy and the charge state. The independence from laser pulse, energy and waist is a very good feature from the perspective of applying the over-the-barrier ionization intensity threshold as an intensity probe. It may be supposed that the ions for which the active electron has its binding energy higher than the saddle point of the effective potential, are easily further ionized, thus generating a strong TOF signal. Therefore, from the analysis of the TOF spectrum of a specific rare gas, it is possible to determine the last charge state Z which produces a visible signal. The immediate statement that can be made is that the intensity available for ionization is higher than the I_{th} for the last measured charge state Z but it is still lower than the I_{th} for the next charge state $Z+1$, not yet visible in the spectrum. In this way, the intensity regime available for ionization can be limited. The electron binding energies

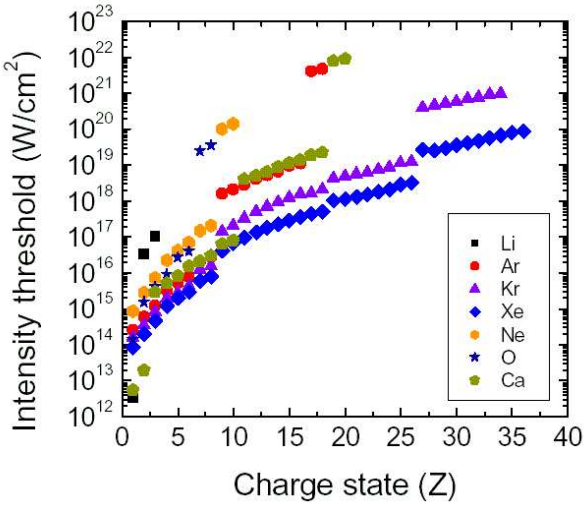

Figure 6.1: Intensity threshold for over the barrier as a function of the charge state, for several atomic species

are tabulated for every atomic species, so that I_{th} can be simply calculated, as

represented in figure 6.1. The proper choice of the atomic species to analyze, may lead to an accuracy within 20% in the intensity determination. In fact, the closer the OBI threshold intensities are for two contiguous charge states, the higher is the precision of the method. So, for example, krypton is an adequate candidate for the determination of intensities between 1×10^{18} and 1×10^{19} W/cm^2, while for higher intensities (up to few times 10^{20} W/cm^2), the ionization of xenon provides a more accurate result.

In our case, the TOF spectrum acquired with a laser energy of $E_L = 0.6$ J is shown in figure 6.2. The last visible charge state for krypton has $Z = 15$ (in red) while in the time range where the highest charge (with $Z > 17$) should appear (circled in figure6.2) no definite signals are evident. It has to be remembered that the detection efficiency does not depend on the charge state as far as $Z \leq 20$. Because the signal of the charge state with $Z = 16$ is

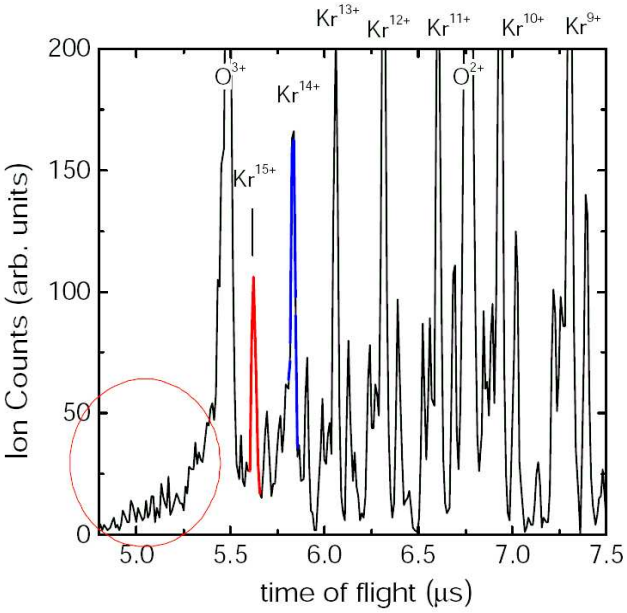

Figure 6.2: TOF spectrum at $E_L = 0.6$ mJ. Krypton ions, resolved in their 4 main isotopes, are visible up to Kr^{15+} (in red), together with the second and third charge of oxygen. At lower times of flight (in the circle), there are no further noticeable signals which point to the presence of higher charge states of krypton ($Z > 17$).

expected to coincide with the signal of O^{3+}, it is not possible to know whether its ionization takes place or not. Thus, we can only limit the intensity regime

between the threshold intensity for Kr^{15+} and Kr^{17+}, that means between 1.25 and 1.7 $\times 10^{18}$ W/cm^2.

6.2 ADK model as Intensity Probe

In the previous chapter, we have shown that the ADK model allows for a description of the behavior of the experimental intensity dependent ion yields for the high charge states generated in the interaction with a laser whose parameters satisfy the tunneling regime. In a comparison between the ADK formula and the TDSE treatment, it appears that the ionization rates deduced from both models exhibit similar variations, although the first overestimates the rates [77]. However, the slope of the single experimental curves as well as the relative behavior among the several curves are well reproduced by the theoretical yields calculated using m-averaged ADK rates. Though, it is still not possible to make any statement about the consistency of the absolute ion yields between the experimental data and the theoretical calculations. Thus, it is the standard procedure to normalize the curves in the yield scale.

The ADK model could provide immediate information of the intensity available for the ionization processes. The idea is related to the fact that the ADK model can predict the number of ions generated under irradiation with a laser beam. By comparing the theoretical yields for several charge states at a fixed intensity with the experimental values, it should be possible to determine the peak intensity regime where the ionization took place.

As already mentioned, an appropriate method for the intensity probe should be independent of the laser parameters. However, the pulse duration and the focus waist are required as initial conditions in the calculation of the ion yields. It is necessary then to deepen the analysis of the ADK model to determine if the initial conditions constrains our request for an intensity probe method. First of all, it has to be noticed that in the simulation the laser beam profile has cylindrical symmetry along the propagation direction and its tail is symmetric with respect to the plane. The pulse duration is also treated as an ideal Gaussian pulse.

The dependency of the ion yields on the beam waist appears in the calculation as the volume available for ionization. At a fixed intensity, a larger focus means a larger volume where a higher number of atoms are available for ionization. This leads to a shift in the yield scale of the curves calculated for

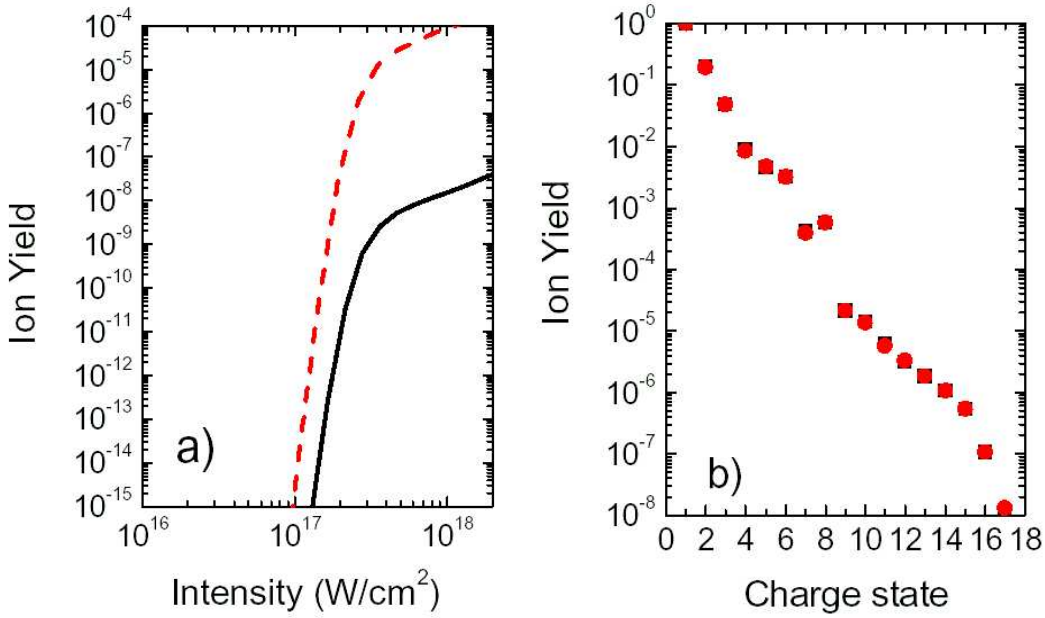

Figure 6.3: a) Ion yield curves for the charge state $Z = 10$ calculated for different waists: (dashed line) $\omega = 8.6$ μm and (solid line) $\omega = 1.0$ μm. b) Normalized ion yields at a fixed intensity ($I = 2.3 \times 10^{18}$ W/cm^2) calculated for different waists: (circles) $\omega = 8.6$ μm and (squares) $\omega = 1.0$ μm.

different focal waists, as shown in figure 6.3a). For our purpose, it is enough to normalize the yields to any of the charge states to remove the dependency of the yields on the waist (see figure 6.3b)).

A more delicate case is the dependency on the laser pulse duration, because the rate equations are time dependent. The calculation of the ion yield occurs through the integration of the rates in the time domain. Therefore, different laser pulses lead to a slight shift of the yield curves in the intensity scale. As shown in figure 6.4a), for a $\tau = 100$ fs pulse width (solid line), the ion yields are smaller than that obtained with a $\tau = 20$ fs pulse (dashed line). However, the behavior is the same for every pulse width. A shift factor of 1.14 is necessary to overlap the two set of curves, as visible in figure 6.4b). So, it has to be noticed that the uncertainty in the intensity evaluation due to the pulse dependence is lower than 15% for an error higher than 80% in the pulse width estimation.

On this basis, one can state that it is not necessary to know precisely the

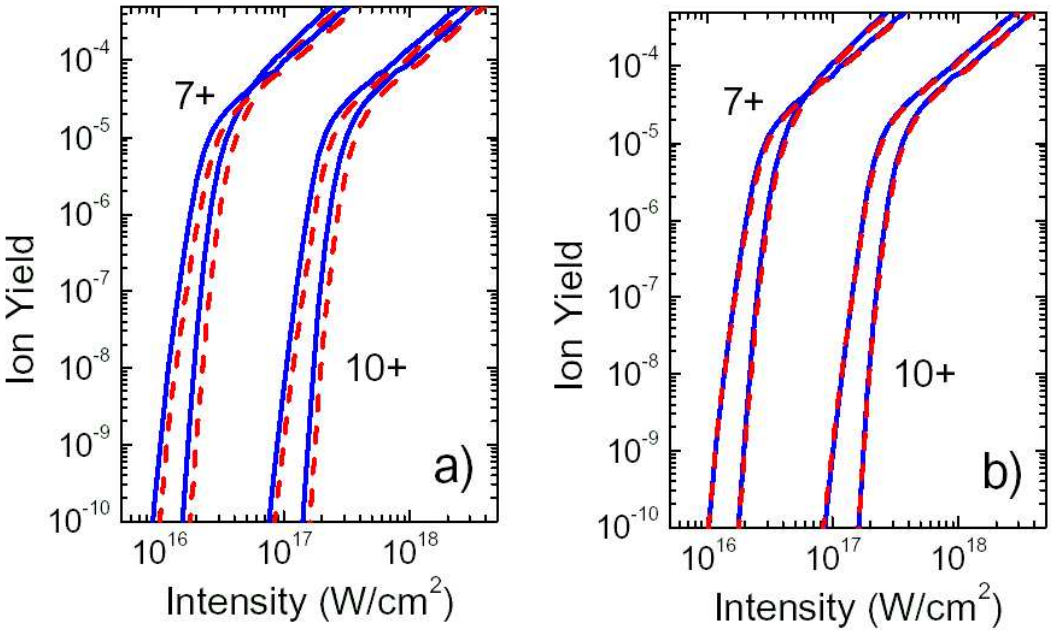

Figure 6.4: a) Ion yield curves for the charge states from $Z = 7$ to $Z = 10$ calculated for different pulses: (solid line) $\tau = 100$ fs and (dashed line) $\tau = 20$ fs. b) A shift factor of 1.14 is enough to overlap the curves calculated for the two different pulses.

pulse width to obtain a good estimation of the laser intensity. It is possible then to implement the method based on ADK rates to the experiment.

The ion yields, below saturation, are very sensitive to the variation of the laser energy E_L. In the TOF spectrum acquired at a fixed E_L, we can extrapolate the yield for several ion states. They can be compared, then, with the theoretical yields calculated for different peak intensities I_{adk}.

An example is shown in figure 6.5, where the data acquisition is accomplished at four different laser energies. The experimental yields (black squares) for several charge states are compared with the values calculated from the ADK theory for different intensities (in the figure expressed in multiples of 10^{18} W/cm^2). The theoretical curves are chosen in order to fit as precisely as possible all the charge states that are not yet in the saturation region. The discrepancy observable for the lowest charge states can be explained, as already mentioned, by the saturation of the detection volumes. The ion yield obtained with the ADK rate, are calculated over an infinite volume, while the detection region is limited by an aperture. The procedure

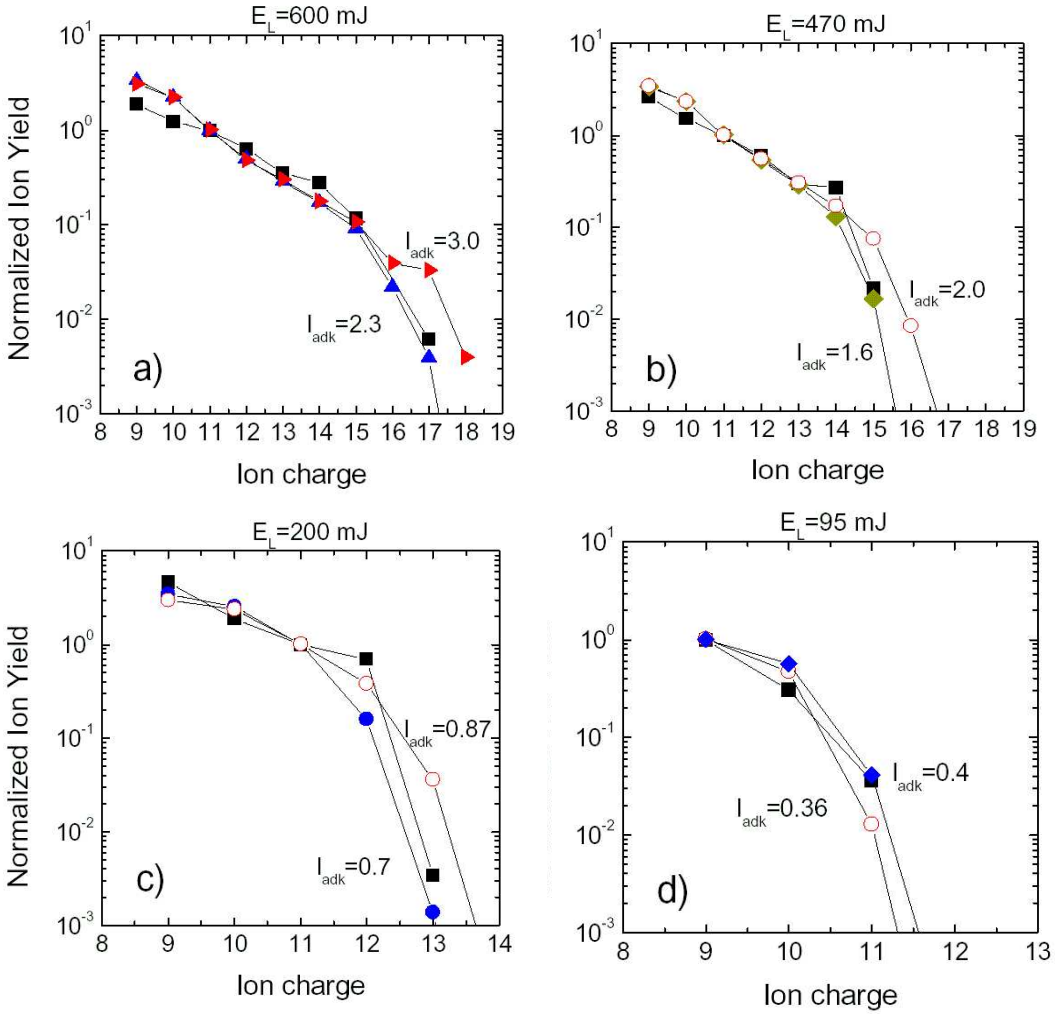

Figure 6.5: Determination of the laser peak intensity using the ion yields for several Kr charge states normalized to Kr^{11+}. The experimental data (squares) are acquired at 4 different laser energies E_L. For each of them, the data are compared with the theoretical yield from the ADK model calculated for different intensities I_{adk} (in the graphs expressed in multiples of 10^{18} W/cm^2).

is made for each energy separately. Furthermore, it is known that the inten-

E_L	I_{ADK}(6.5) 10^{18}W/cm^2	I_i 10^{18}W/cm^2
600	$2.3 - 3.0$	
470	$1.6 - 2.0$	$1.8 - 2.3$
200	$0.7 - 0.8$	$0.76 - 1.0$
95	0.4	$0.4 - 0.47$

Table 6.1: Intensity values I_{ADK} extrapolated from the ADK model and I_i estimated from the intensity dependence on the energy. They are in agreement with each other. In the table, the intensity values are given in multiple of 10^{18} W/cm^2.

sity scales linearly with the energy ($I_i = I_p \frac{E_i}{E_p}$). Once the peak intensity I_p corresponds to the highest energy value, it is also possible to derive the lower ones by using the linear relation between intensity and energy. In table 6.1 are listed the intensity values estimated from ADK independently for the several energies and from the linearity in relation to the peak intensity. As is visible, the results obtained independently for the different energies are compatible.

One should be careful to choose the experimental data for the comparison with the ADK theory to determine the laser intensity, as the ion yields for the charge states below saturation are very sensitive to the background. An enhanced ion yields due to the background may lead, in fact, to a wrong intensity determination. An example is shown in figure 6.6. In the spectrum acquired at $E_L = 730$ mJ (figure 6.6a)), in the time of flight range where the signals of the highest charge state of krypton are expected to appear, several peaks are visible. The signal to noise ratio is not good enough to distinguish clearly the peaks. If we suppose that the peak marked in red is the signal for $Z = 17$, the extrapolated yields would have a behavior like shown in figure 6.6b). As shown in figure 6.6b), using the ADK model to determine the intensity a value which fits the results better corresponds to a peak intensity I_p between 2.6 and 3.8×10^{18} W/cm^2 (empty circles in figure 6.6b)). Also shown in figure 6.6c) is the acquired time of flight spectrum at decreased energy of $E_L = 700$ mJ. The signal for Kr^{17+} is, now, almost not distinguishable from the background peaks. Once more, in figure 6.6d) the experimental yields are compared with the theoretical ones. The data can be fitted with a peak intensity of about $I_p = 2.3 - 2.6 \times 10^{18}$

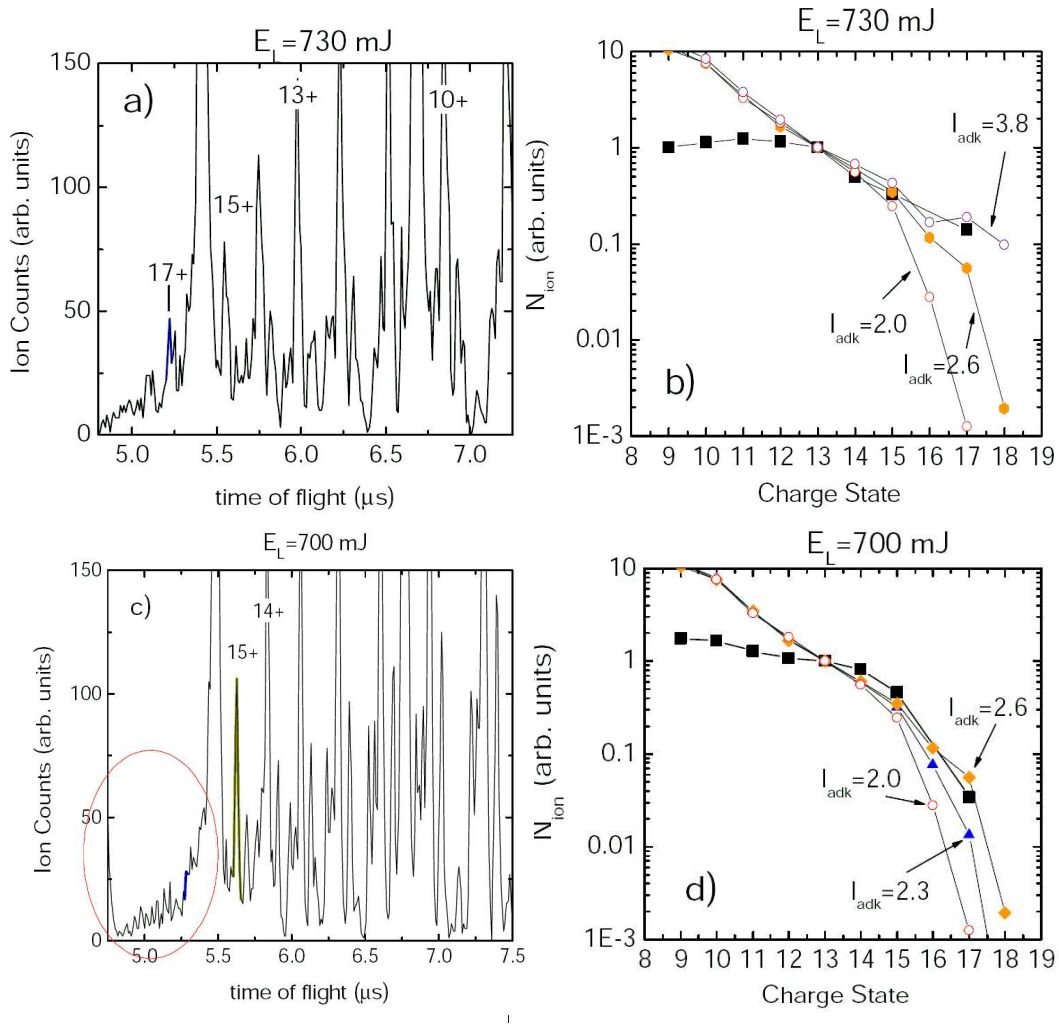

Figure 6.6: a) TOF spectrum acquired at the laser energy of $E_L = 730$ mJ. b) The ion yield signal extrapolated from a) is compared with the yield from the ADK model at three different intensities. c) TOF spectrum acquired at the laser energy $E_L = 700$ mJ and d) The ion yields are compared with the theoretical values at intensities scaled from a).

W/cm^2. Scaling with the energy to $E_L = 730$ mJ, the maximum peak intensity regime would be about $I = 2.4 - 2.7 \times 10^{18}$ W/cm^2 which is a factor 0.3 lower than the direct estimation obtained with the ADK model. If we now decide to neglect the signal of Kr^{17+}, the intensity regime extimated for $E_L = 730$ mJ reduce to $I = 2.0 - 2.6 \times 10^{18}$ W/cm^2 and for $E_L = 700$ mJ to $I = 2.0 - 2.3 \times 10^{18}$ W/cm^2. The magnitude of the intensities derived here is expected from the linear scale relation with the energy.

In conclusion, the ADK model seems to be a good method for a relative determination of the laser intensity within a maximum error of 15% if the laser pulse duration is unknown. Of course, such a method is applicable for laser systems whose parameters satisfy the conditions for the tunneling ionization regime, where the ADK theory is valid.

The experimental background conditions are required to be as good as possible to increase the detection resolution of the highly charge states. Besides, it is recommended to pursue the experiment at two laser energies at least. Such a procedure reduces the error in the intensity determination due to experimental limits.

Applying the ADK method to our experimental data, we conclude a maximal peak intensity of $2.0 - 2.6 \times 10^{18}$ W/cm^2 available for the experiment, which is almost a factor of two higher than the intensity estimated using the method based on the over-the-barrier intensity threshold ($1.2 - 1.7 \times 10^{18}$ W/cm^2).

By inserting the three laser parameters listed in chapter 3 ($E_L = 0.6 - 0.7$J, $\omega_0 = 8 - 9$ μm and $\tau = 40$ fs) in the equation (3.4) $I_p = 0.94 E_L/(\pi\omega_0^2\tau)$, the resulting peak intensity is $I_p = 4.8 - 6.5 \times 10^{18}$ W/cm^2 which is almost a factor of three larger than that by using the ADK method.

Several reasons can explain this difference. At first, the background reduces significantly the resolution of the experiment. It enhances strongly the signals over the full time scale so that the weak signals produced by the highly charged ions cannot clearly be resolved. Secondly, the focus waist is measured under conditions different from those of the experiment: for instance, the energy is attenuated. It is not possible to evaluate how much the focus dimension as well the laser front quality change when the energy of the focused beam increases by more than three order of magnitude. Additionally, during the long acquisition time, the pulse duration is fluctuating. Such fluctuation could possibly be measured however, with an "on-line" single shot pulse width measurement.

In conclusion, the investigation of the ionization dynamics for highly

I_{OBI}	I_{ADK}	I_p
$1.25 - 1.7$	$2.0 - 2.6$	$4.8 - 6.5$

Table 6.2: Comparison of the peak intensities delivered by the three different intensity probe methods: Over-the-barrier intensity threshold (I_{OBI}), ADK (I_{ADK}) and intensity calculated using equation (3.4) (I_p). The values are expressed in multiples of 10^{18} W/cm^2.

charged states is not only useful for a deeper understanding of the atomic physics at ultra high intensities. We have shown that the experiment as well as the theory behind it can be used in a more practical field. In table 6.2 are listed the peak intensities obtained from the three different methods.

It is possible then to adopt the over-the-barrier threshold ionization for a first coarse approximation of the peak intensity while for more precise information, the ADK method is recommended. Of course, the method which applies the ADK theory as an intensity probe does not deliver an absolute yield value, but it seems to be much more reliable for the determination of the intensity than the calculation from the three laser parameters that have to be measured independently. Moreover, the laser focus measurement is usually performed under completely different conditions than the one at which the experiment is pursued. This gives an uncertainty in the intensity determination much higher than the ADK model.

6.3 Laser intensity via ion yield optimization

The ionization signal, besides its application in possible determination of the absolute intensity, yields a relative value which can be used to optimize the pulse duration. As mentioned in chapter 3, the pulse width is determined in the recompression stage of the laser system by the distance and the angle at which the gratings are positioned. Usually, the pulse measurement with the SPIDER system has to be done before or after the experiment because it requires the full energy of the beam. This means a lot of time subtracted from the real experiment time. As long as an "on-line" method to measure the pulse simultaneously to the experiment is not found, the experiment itself can be used to optimize the pulse.

6.3.1 Gratings distance

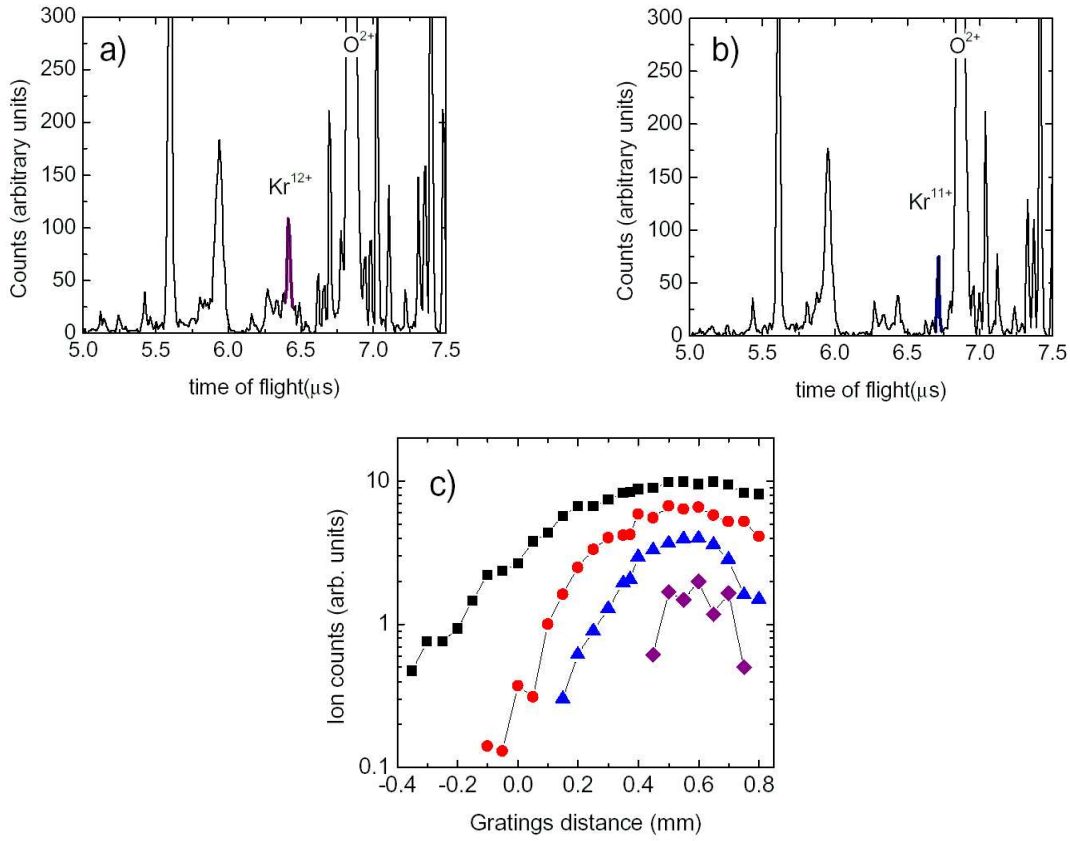

Figure 6.7: Kr spectrum acquired with a compression gratings distance that is respectively: a) 0.6 *mm*; b) 0.7 *mm*. Ion counts for Kr^{9+} (squares), Kr^{10+} (circles), Kr^{11+} (triangles) and Kr^{12+} (diamonds) as a function of the distance variation between the gratings.

The distance between the gratings is one of the fundamental parameters to obtain a short pulse. A wrong adjustment leads to a broad pulse and a low intensity. The ionization experiment can be useful for the optimization of this parameter. Acquiring the TOF spectrum at different grating distances, it is possible to determine in which position the highest charge states are observable. When the higher charge states is resolved, the optimization can be refined by maximizing the signal of the peaks.

In figure 6.7a) and b) are shown two example of spectra acquired at

different grating distances: in a) the higher charge state visible is Kr^{12+} (in purple) and the peak of Kr^{11+} is a strong signal while in b) the highest charge state is now $Z = 11$ and the signal is much weaker (60% smaller than for the previous case). Figure 6.7c) shows the signals for the charge states from Kr^{9+} to Kr^{12+} as a function of the variation of the gratings distance with respect to the initial position. The shortest pulse is obtained at a distance variation of about $0.6mm$.

6.3.2 Telescope angle

The same concept can be applied for the optimization of the angle between the gratings. In figure 6.8 is shown the TOF signal for Kr^{14+} at different angles. Again it is seen that there is only one position where the signal is at a maximum.

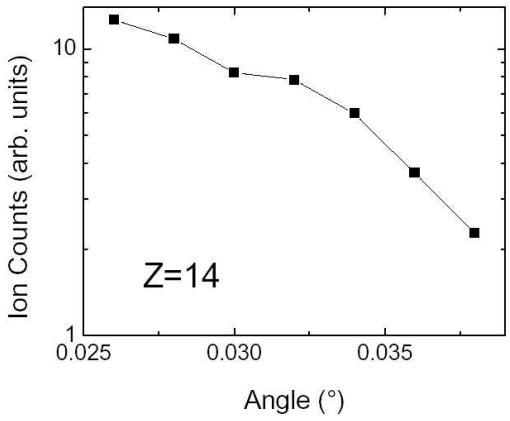

Figure 6.8: TOF signal for Kr^{14+} in function of the angle between the recompression gratings.

Conclusions

In this work we have presented experimental investigations on ionization dynamics for heavy atom species (Kr and Xe) exposed to super strong laser fields. We have focused our interest on the analysis of the intensity dependent ion yields for highly charged states. In particular, the $d-$subshell ionization of krypton and xenon has been investigated in linearly and circularly polarized light. The experimental results have been discussed within several theoretical models.

Our goal was the understanding of the dominant ionization mechanisms in the "quasi"-relativistic regime where we expect the so-called nonsequential ionization, known to be dominant at low intensities, to loose importance. We define the intensities between 10^{16} and 10^{18} W/cm^2, where the highly charged states are produced, as "quasi"-relativistic regime. Here, the electrons released in the continuum during the ionization process, are accelerated by the laser light to velocities which are approaching the speed of light. Hence, the influence of the magnetic field component is no longer negligible in the treatment of the ionization processes.

We have examined the applicability of the ADK theory [7], which describes the single-electron ionization process at nonrelativistic intensities, also for highly charged states. The choice of this theory is in agreement with a theoretical work [27] which has shown that the tunneling process for charge states with $Z \leq 20$ is not influenced by relativistic effects. The calculation of the ion yields using the ionization rates described by the ADK theory, requires to know exactly the initial state of the active electron (by its quantum numbers n,l and m). Because for the inner subshells of a multi-electron system, several electrons have the same n and l but different m quantum numbers, our main goal is to investigate experimentally whether the initial state of the active electron influences the sequential ionization process. To proceed in this analysis it was necessary, at first, to verify that the sequential

ionization is indeed dominant in the "quasi"-relativistic intensity regime. In absence of any information on the initial state of the active electron, we have modeled at first the ion yields for highly charged states using the rates for sequential ionization averaged over the magnetic quantum numbers.

We have shown that the agreement between experiment and calculated curves extends also to intensities where saturation due to volume effects occurs, with the exception of Kr^{9+} and Kr^{10+} for which a depletion of the detection volume is observed. For all the highly charged states, no evidence of the knee which is the "fingerprint" of the nonsequential ionization process is present. For nonrelativistic laser fields it is well known that a first electron which is set free by tunneling, returns to the parent ion under the influence of the external laser field and collisionally it dislodges a second electron. The role of the rescattering mechanism for the ionization process is expected to be largely diminished for highly charged ions [13]. The first evidences of the suppression of nonsequential ionization were provided only a few years ago by measuring the intensity dependent ion yields for neon [15]. Our experimental results on Kr and Xe have confirmed that the rescattering process is no longer dominant in the "quasi"-relativistic regime.

We have discussed the experimental observations by means of the semi-classical approach for the nonsequential ionization, also taking into account the influence of the relativistic effects on multiple ionization. On the one hand, the e−2e cross section, which is the characteristic parameter for the recollision process, strongly depends on the charge state of the parent ion and it reduces of more than two orders of magnitude from Kr^{+} to Kr^{15+}. Furthermore, the width of the recolliding electron wave packet increases with the ionic charge state. Thus, the rescattering probability decreases by more than four orders of magnitude from Kr^{+} to Kr^{18+}.

On the other hand, the returning electron drifts away from the core under the influence of the magnetic component of the laser field. Three different calculations have been used to describe the electron motion. We have shown that the first order relativistic effects ((v/c)) due to the Lorentz force ($\mathbf{F} = q(\mathbf{E} + v/c \times \mathbf{B})$), are sufficient to describe fully the electron dynamics for the charge states under study ($7 \leq Z \leq 15$). In fact, second order effects ($(v/c)^2$), which are related to the electron rest mass ($\mathbf{F} = mv/\sqrt{1-(v/c)^2}$), set in only at very high intensities, for charge states with $Z \geq 19$. We have also shown that the Coulomb force which acts on the returning electron due to the presence of the parent ion and which is expected to reduce the Lorentz drift, affects significantly only the trajectories of the electrons released from

low charged ions ($Z \leq 4$). This leads the rescattering probability to vanish exponentially for the charged states with $9 \leq Z \leq 15$.

In conclusion, for charges below Kr^{9+} the suppression of rescattering is mainly attributed to the strong reduction of the e$-$2e cross section for electron-ion collision. For higher charge states, moreover, the returning electron misses the parent ion under the influence of the magnetic field component.

The dominance of the sequential process in ionization of the charge states resulting from the closed $d-$shell of heavy atoms has opened a new field of investigation of the behavior of the electrons subjected to an intense laser field. It is known that the ADK ionization rates strongly depend on the magnetic quantum number of the active electron [7]. The electrons in the $m = 0$ state have more than two orders of magnitude higher rates than the electrons in $m = 2$ state. If ionization is faster than the core relaxation time, the electrons are expected to remain in their unperturbed states keeping their initial quantum numbers. Then, the two electrons in the $m = 0$ substate would be ionized first because they have a high tunneling probability. The four electrons in $m = 2$ state are ionized last at a substantially lower rate. The ion yields for the $d-$shell electrons provide a direct evidence for it.

A comparison of the experimental results with the yields computed taking into account this ionization "priority" has clearly shown a deviation which rises to more than three orders of magnitude for the highest charge states. In contrast, ion yields computed using ionization rates statistically averaged over the available m-quantum numbers describe well the experimental results. We conclude that during the sequential ionization process the ionic core fully relax before the next ionization occurs. Any memory of the initial magnetic quantum number is erased during ionization via a fast $m-$substate-mixing process. One reason for the state mixing is electron-electron correlation. Between two ionization stages the electrons remaining in the shell couple to a total angular momentum. Furthermore, besides the ionization process, the interplay of the orthogonal electric and magnetic field components acts on the active electron through a simultaneous Zeeman and Stark shift of its energy level which leads to a rearrangement of the electronic state into a combination of the magnetic quantum numbers m.

In a femtosecond laser pulse, the electrons are stripped out of the core sequentially in several laser cycles. Experiments with attosecond laser pulses, where ionization of several electrons is expected to occur within one cycle, could deliver further informations on the effective time scale at which core

relaxation actually takes place. Unfortunately, the current state-of-art technique does not yet provide such laser pulses with the required intensity.

Besides fundamentals of atomic dynamics, we were also interested in a theme which is of importance to the whole intense-laser community: namely the measurement of intensities larger than 10^{17} W/cm^2. The normal procedure through the measurement of energy, pulse width and focus waist simply fails because the optics cannot stand the laser intensity. This leads to the necessity to find a new standard which could directly probe the laser intensity. The fact that for intensities higher than 10^{17} W/cm^2 the ionization mechanism is purely sequential and the tunneling theory is still valid provides the opportunity to use the ionization dynamics as intensity probe. In the last chapter of this work two methods have been discussed for the intensity characterization, based on over-the-barrier ionization (OBI) and on the ADK theory respectively.

The first method consists in the identification of the last charge state Z whose signal is clearly distinguishable from the noise. The laser intensity available for the experiment is supposed to be higher than the threshold value for OBI of the visible charge state (Z) but too low to generate the next ion (with $Z+1$). The advantage of this method is the independency of the OBI threshold intensity from laser energy, pulse width and focus waist. Choosing a proper rare gas for different intensity regions, it is possible to determine the peak intensity within an accuracy of 20%.

The method based on the ADK theory releases a good method for a determination of the laser intensity. It is known that the calculated curves using the ADK ionization rates do not deliver an absolute ion yields, however our results have reproduced the slope of the intensity dependent ion yields for each charged states and, above all, the relative distance between the several curves. These two conditions are the important requirements for the applicability of the ADK theory as intensity probe. It is possible to use ADK to define the laser peak intensity, by fitting the measured ion yields for several charge states with the corresponding calculated yields. The more charge states that are available below the saturation region, the more effective is the method. However, the highest charge states are measurable only under the condition of extremely high signal to noise ratio, which is not easily applicable in an experiment pursued at such intensities. A comparison between the results obtained by applying the two methods to our experiment has shown a difference of a factor of two, which corresponds to an error of 30% in the intensity determination.

With the calculation of the intensity by using the equation $I_p = E_L/(\pi\omega_0^2\tau)$, where each parameter was measured separately, the peak intensity results in more than a factor of three larger value than by using the ADK method. However, the uncertainty in such measurement is much higher than for the ADK method. For example, it has to be taken into consideration that the focus waist is measured under conditions different from those of the experiment: in fact, the energy is attenuated. It is not possible, then, to evaluate how much the focus dimension as well the laser front quality changes when the energy of the focused beam increases by more than three order of magnitude. Additionally, during the long acquisition time, the pulse duration is fluctuating. The advantage of the ADK theory is, moreover, the possibility to measure the intensity "on-line" while the experiment is running.

In conclusion, we have shown that the method based on the threshold intensity for over-the-barrier ionization is applicable for a coarse approximation of the peak intensity, while the ADK theory releases a good method for a determination of the relative laser intensity.

Bibliography

[1] D. Strickland and G. Morou. "Compression of Amplified Chirped Optical Pulses". *Opt. Commun.*, **56**(3):219, 1985.

[2] G.S. Voronov and N.B. Delone. "Ionization of the Xenon Atom by the Electric Field of Ruby Laser Emission". *JETP Lett.*, **1**:66, 1965.

[3] J.L. Hall, E.J. Robinson, and L.M. Branscomb. "Laser Double-Quantum Photodetachment of I^-". *Phys. Rev. Lett.*, **14**:1013, 1965.

[4] P. Agostini, F. Fabre, G. Mainfray, G. Petite, and N. Rahman. "Free-Free Transitions Following Six-Photon Ionization of Xenon Atoms". *Phys. rev. Lett.*, **42**:1127, 1979.

[5] P. Agostini G. Petite and H. G. Muller. "Intensity dependence of non-perturbative above-threshold ionisation spectra: experimental study". *J. Phys. B: At. Mol. Phys*, **21**:4097, 1988.

[6] L.V. Keldysh. "Ionization in the Field of a Strong Electromagnetic Wave". *Sov. Phys. JETP*, **20**(1307), 1965.

[7] N.N. Delone M.V. Ammosov and V.P. Krainov . "ionization dynamics in strong laser fields". *Sov. Phys. JETP*, **64**:1191, 1986.

[8] B. Walker, B. Sheehy, L.F. DiMauro, P. Agostini, K.J. Shafer, and K.C. Kulander. "Precision Measurement of Strong Field Double Ionization of Helium". *Phys. Rev. Lett*, **73**:1227, 1994.

[9] S. Larochelle , A. Talebpour , and S.L. Chin . "Non-sequential Multiple Ionization of Rare Gas Atoms in a Ti:Sapphire Laser Field". *J. Phys. B*, **31**:1201–1214, 1998.

[10] R. Moshammer, B. Feuerstein, W. Schmitt, A. Dorn, C. D. Schröter, J. Ullrich, H. Rottke, C. Trump, M. Wittmann, G. Korn, K. Hoffmann, and W. Sandner. "Momentum Distributions of Ne^{n+} Ions Created by an Intense Ultrashort Laser Pulse". *Phys. Rev. Lett.*, **84**:447, 2000.

[11] T. Weber, M. Weckenbrock, A. Staudte, L. Spielberger, O. Jagutzki, V. Mergel, F. Afaneh, G. Urbasch, M. Vollmer, H. Giessen, and R. Dörner. "Recoil-Ion Momentum Distributions for Single and Double Ionization of Helium in Strong Laser Fields". *Phys. Rev. Lett.*, **84**:443, 2000.

[12] P.B. Corkum. "Plasma Perspective on Stron-Field Multiphoton Ionization". *Phys. Rev. Lett.*, **71**:1994, 1993.

[13] M. Dammasch , M. Dï¿½r, U. Eichmann, E. Lenz, and W. Sandner. "Relativistic laser-field-drift suppression of nonsequential multiple ionization". *Phys. Rev. A*, **64**(061402), 2001.

[14] E.A. Chowdhury, C.P.J Barty, and B. Walker. "Nonrelativistic Ionization of the L-shell states in Argon by a "Relativistic" 10^{19} W/cm^2 Laser Field". *Phys. Rev. A*, **6**3:042712, 2001.

[15] E.A. Chowdhury and B. Walker. "Multielectron Ionization process in Ultrastrong Laser Fields". *J. Opt. Soc. Am. B*, **20**:109–112, 2003.

[16] K. Yamakawa, Y. Akahane, Y. Fukuda, M. Aoyama, N. Inoue, H. Ueda, and T. Utsumi. "Many-Electron Dynamics of a Xe Atom in Strong and Superstrong Laser Fields". *Phys. Rev. Lett.*, **92**:123001, 2004.

[17] F. Fabre, G. Petite, P. Agostini, and M. Clement. "Multiphoton above-threshold ionisation of xenon at 0.53 and 1.06μm". *J. Phys. B: At. Mol. Phys*, **15**:1353, 1982.

[18] G. Petite, F. Fabre, P. Agostini, M. Crance, and M. Aymar. "nonresonant multiphoton ionization of cesium in strong fields: Angular distributions and above-threshold ionization". *Phys. Rev. A*, **29**:2677–2689, 1984.

[19] B. Walker, E. Mevel, B. Yang, P. Breger, J.P. Chambaret, A. Antonetti, L.F. DiMauro, and P. Agostini. "Double Ionization in the Perturbative and Tunneling Regime". *Phys. rev. A*, **48**:894, 1993.

[20] Y. Gontier and M. Trahin. "Energetic Electron Generation by Multiphoton Absorption". *J. Phys. B*, **13**:4383, 1980.

[21] T.F. Gallagher. "Above-Threshold Ionization in Low-Frequency Limit". *Phys. Rev. Lett.*, **61** :2304, 1988.

[22] P.B. Corkum, N.H. Burnett, and F. Brunel. "Above-Threshold Ionization in the Long-Wavelength Limit". *Phys. Rev. Lett.*, **62**:1259, 1989.

[23] M. Protopapas, C.H. Keitel, and P.L. Knight. "Atomic Physics with Super-High Intensity Lasers". *Rep. Prog. Phys*, **60**:389–486, 1997.

[24] R. Shakeshaft, R.M. Potvliege, M. Dörr, and W.E. Cooke. "Multiphoton Processes in an Intense Laser Field. IV. The Static-Field Limit". *Phys. Rev. A*, **42** :1656, 1990.

[25] N.N. Delone M.V. Ammosov . "tunneling ionization and above-barrier decay of atoms under the action of pulsed laser radiation". *Laser Phys.*, **7**:79, 1997.

[26] A. M. Perelomov, V. S. Popov, and M. V. Terentév. "Ionization of Atoms in an Alternating Electric Field". *Sov. Phys. JETP*, **23**:924, 1966.

[27] N. Milosevic, V.P. Krainov, and T. Brabec. "Relativstic Theory of Tunnel Ionization". *J. Phys. B: At. Mol. Opt. Phys.*, **35** :3515, 2002.

[28] K.J. Schafer, B. Yang, L.F. DiMauro, and K.C. Kulander. "Above threshold ionization beyond the high harmonic cutoff". *Phys.Rev.Lett.*, **70**:1599, 1993.

[29] l'Huillier A., Lompre L.A., Mainfray G., and Manus C. "Multiply charged ions induced by multiphoton absorption in rare gases at $0.53\mu m$". *Phys. Rev. A*, **27**:2503, (1983).

[30] D.N Fittinghoff, P.R. Bolton , B. Chang, and K.C. Kulander. "Observation of Non-sequential Double Ionization of Helium with Optical Tunneling". *Phys. Rev. Lett.*, **69**(18):2642, 1992.

[31] K. Kondo, A. Sagisaka, T. Tamida, Y. Nabekawa, and S. Watanabe. "Wavelength Dependence of Nonsequential Double Ionization in He". *Phys. Rev. A*, **48**:R2531, 1993.

[32] S. Augst, D. Strickland, D.D Meyerhofer, S.L. Chin, and J.H. Eberly. "Tunneling Ionization of Noble Gases in High-Intensity laser Field". *Phys. Rev. Lett*, **63**:2212, 1989.

[33] H. Maeda, M. Dammasch, U. Eichmann, W. Sandner, A. Becker, and F.H.M Faisal. "Strong Field Multiple Ionization of Krypton". *Phys. Rev. A*, **62**(035402), 2000.

[34] R. Wehlitz, F. Heiser, O. Hemmers, B. Langer, A. Menzel, and B. Becker. "Electron-Energy and -Angular Distributions in the Double Photoionization of Helium". *Phys. Rev. Lett.*, **67**:3764, 1991.

[35] P. Dietrich, N.H. Burnett, M. Ivanov, and P.B. Corkum. "High-harmonic Generation and Correlated Two-electron Multiphoton Ionization with Elliptically Polarized Light". *Phys. Rev. A*, **50**:R3585, 1994.

[36] D.N. Fittinghoff , B. Chang , P.R. Bolton , and K.C. Kulander. "Polarization dependence of tunneling ionization of helium and neon by 120-fs pulses at 614 nm". *Phys. Rev. A*, **49**:2174, 1994.

[37] G.H. Wannier. "The Threshold Law for Single Ionization of Atoms or Ions by Electrons". *Phys. Rev.*, **90**:817, 1953.

[38] U. Eichmann, M. Dörr, H. Maeda, W. Becker, and W. Sandner. "Collective Multielectron Tunneling Ionization in Strong Fields". *Phys. Rev. Lett.*, **84**(3550), 2000.

[39] A. LHuillier, K.J. Schafer, and K.C. Kulander. "Higher-order harmonic generation in xenon at 1064 nm: The role of phase matching". *Phys. Rev. Lett.*, **66**:2200, 1991.

[40] B. Walker, B. Sheehy, K.C. Kulander, and L.F. DiMauro. "Elastic Rescattering in the Strong Field Tunneling Limit". *Phys. Rev. Lett.*, **77**:5031, 1996.

[41] T. Weber, H. Giessen, M. Weckenbrock, G. Urbasch, A. Staudte, L. Spielberger, O. Jagutzki, V. Mergel, M. Vollmer, and R. Dörner. "Correlated Electron Emission in Multiphoton Double Ionization". *Nature*, **405**:658, 2000.

[42] B. Feuerstein, R. Moshammer, D. Fischer, A. Dorn, C. D. Schröter, J. Deipenwisch, J.R. Crespo Lopez-Urrutia, C. Höhr, P. Neumayer, J. Ullrich, H. Rottke, C. Trump, M. Wittmann, G. Korn, K. Hoffmann, and W. Sandner. "Separation of Recollision Mechanisms in Non-sequential Strong Field Double Ionization of Ar: The Role of Excitation Tunneling". *Phys. Rev. Lett*, **87**:043003, 2001.

[43] M. Weckenbrock, M. Hattas, A. Czasch, O. Jagutzki, L. Schmidt, T. Weber, H. Roskos, T. Löffler, M. Thomson, and R. Dörner. "Experimental Evidence for Electron Repulsion in Multiphoton Double Ionization". *J. Phys. B*, **34**:L449, 2001.

[44] K. Eremina, X. Liu, H. Rottke, W. Sandner, A. Dreischuhand F. Lindner, F. Grasbon, G.G. Paulus, H. Walther, R. Moshammer, B. Feuerstein, and J. Ullrich. "Laser-induced Non-sequential Double Ionization Investigated At and Below the Threshold for Electron Impact Ionization". *Phys. Rev. Lett.*, **84**:447, 2000.

[45] J. Parker, K.T. Taylor, C.W. Clark, and S. Blodgett-Ford. "Intense-Field Multiphoton Ionization of a Two-Electron Atom ". *J. Phys. B: At. Mol. Opt. Phys.*, **29** :L33, 1996.

[46] J.B. Watson, A. Sanpera, D.G. Lappas, P.L. Knight, and K. Burnett. "Nonsequential Double Ionization of Helium". *Phys. Rev. Lett.*, **78**:1884, 1997.

[47] E.S. Smyth, J. Parker, and K.T. Taylor. "Numerical Integration of the Time-Dependent Schrï¿$\frac{1}{2}$inger Equation for Laser-Driven Helium". *Comput. Phys. Commun.*, **114** :1, 1998.

[48] P.G. Burke, P. Francken, and C.J. Joachain. "R-matrix-Floquet Theory of Multiphoton Processes". *J. Phys. B: At. Mol. Opt. Phys.*, **24** :751, 1991.

[49] M. Dörr, M. Terao-Dunseath, J. Purvis, C.J. Noble, P.G. Burke, and C.J. Joachain. "R-matrix-Floquet Theory of Multiphoton Processes. II. Solution of the Asymptotic Equations in the Velocity Gauge". *J. Phys. B: At. Mol. Opt. Phys.*, **25** :2809, 1992.

[50] D.H. Glass, P.G. Burke, H.W. van der Hart, and C.J. Noble. " R-matrix-Floquet Theory of Multiphoton Processes: VIII. A Linear Equations Method ". *J. Phys. B: At. Mol. Opt. Phys.*, **30** :3807, 1997.

[51] A. Becker and F.H.M. Faisal. "Mechanism of Laser-Induced Double Ionization of Helium ". *J. Phys. B: At. Mol. Opt. Phys.*, **29** :L197, 1996.

[52] B. Sheehy, R. Lafon, M. Widmer, B. Walker, L.F. DiMauro, P. Agostini, and K.C. Kulander. "Single- and Multiple-Electron Dynamics in the Strong-Field Tunneling Limit". *Phys. Rev. A*, **58**:3942, 1998.

[53] J.S. Parker, E. Smith, and K.T. Taylor. "Intense-field Multiphoton Ionization of Helium". *J. Phys. B*, **31**:L571, 1998.

[54] D. Dundas, K.T. Taylor, J.S. Parker, and E. Smith. "Double Ionization Dynamics of Laser-driven Helium". *J. Phys. B*, **32**:L231, 1999.

[55] K.T. Taylor, J.S. Parker, D. Dundas, E. Smith, and S. Vivirito. "Laser-Driven Helium in Fully Dimensionality". *Las. Phys.*, **9**:98, 1999.

[56] D. Bauer. "Two-dimensional, two-electron model atom in a laser pulse: Exact treatment, single-active-electron analysis, time-dependent density-functional theory, classical calculations, and nonsequential ionization". *Phys.Rev.Lett.*, **56**:3028, 1997.

[57] A. Becker and F.H.M. Faisal. "Interplay of electron correlation and intense field dynamics in the double ionization of helium". *Phys.Rev.Lett.*, **59**:R1742, 1999.

[58] A. Becker and F.H.M. Faisal. "Production of high-charge states of Xe in a femtosecond laser pulse". *Phys.Rev. A*, **59**:R3182, 1999.

[59] A. Becker and F.H.M. Faisal. "S-matrix analysis of ionization yields of noble gas atoms at the focus of Ti:sapphire laser pulses". *J. Phys. B*, **32**:L335, 1999.

[60] H.W. van der Hart and K. Burnett. "Recollision Model for Double Ionization of Atoms in Strong Laser Fields". *Phys. Rev. A*, **58**:3942, 1998.

[61] H.R. Reiss. "Dipole-approximation magnetic fields in strong laser beams". *Phys. Rev. A*, **63**:013409, 2000.

[62] T. Brabec, M.Y. Ivanov, and P.B. Corkum. "Coulomb Focusing in Intense Field Atomic Processes". *Phys. Rev. A*, **54**:R2551, 1996.

[63] V. Karpov M.P. Kalachnikov and H. Schönnagel. "100−Terawatt Titanium-Sapphire Laser System". *Laser Phys.*, **02**:368, 2002.

[64] P. Maine et al. "Generation of Ultrahigh Peak Power Pulses by Chirp Pulse Amplification". *IEEE J. Quantum Electron.*, **24**(2):398, 1988.

[65] M. F. Dammasch. *"Atomare Ionisationsdynamik in Hochintensiven Laserfeldern"*. PhD thesis, Fachbereich 4 (Physik) der Technischen Universitätï¿½ Berlin, 2001.

[66] M.M. Murnane S. Backus, C.G. Durfee III and H.C. Kapteyn. "High power ultrafast lasers". *Rev. Sci. Instr.*, **69**:1207, 1998.

[67] A.J. Langley, E.J. Divall, C.H. Hooker, M.H.R. Hutchinson, A.J-M.P. Lecot, D. Marshall, M.E. Payne, and P.F. Taday. "the development pf a multi-terawatt femtosecond laser facility-astra". Technical report, CLF Rutherford Appleton Laboratory Annual Report, 1999-2000.

[68] C.P.J Barty, T. Guo, C. Le Blanc, F. Raksi, C. Rose-Petruck, Jeff Squier, K. R. Wilson, V. V. Yakovlev, and K. Yamakawa. "Generation of 18-fs, multiterawatt pulses by regenerative pulse shaping and chirped-pulse amplification". *Optics Lett.*, **21**:668, 1996.

[69] J.P. Chambaret, C. Le Blanc, G. Cheriaux, P. Curley, G. Darpentigny, P. Rousseau, G. Hamoniaux, A. Antonetti, and F. Salin. "Generation of 25-TW, 32-fs pulses at 10 Hz". *Optics Lett.*, **21**:1921, 1996.

[70] F. Eggenstein, F. Senf, T. Zeschke, and W. Gudat. "Cleaning of contaminated XUV-optics at BESSY II". *Nucl.Instr. and Meth. A*, **467-468**:325–328, 2001.

[71] A. E. Vladàr, M.T. Postek, and R. A. Vane. "Active Monitoring and Control of Electron Beam Induced Contamination". In *Proc. SPIE*, volume 4344, page 835, 2001.

[72] *Handbook of Deposition Technologies for Films and Coatings*, chapter Surface Preparation for Films and Coatings Deposition Processes. Noyes Publications, Park Ridge, 1994.

[73] B. Chang , P.R. Bolton , and D.N. Fittinghoff . "Closed-Form Solutions for the Production of Ions in the Collisionless Ionization of Gases by Intense Lasers". *Phys. Rev. A*, **47**:4193, 1993.

[74] S.D Loch, M. S. Pindzola, C.P. Ballance, D.C. Griffin, D.M. Mitnik, N.R. Badnell, M.G. O Mullane, H.P. Summers, and A.D. Whiteford. "Electron-impact ionization of all ionization stages of krypton". *Phys. Rev. A*, **66**:052708, 2002.

[75] B. Gottlieb, A. Lohr, W. Becker, and M. Kleber. "Dynamics of Electronic Wave Packets in Field Emission and Intense-field Laser-atom Physics". *Phys. Rev. A*, **54**:R1022, 1996.

[76] W. Lotz. "Electron-Impact Ionization Cross-Section for Atmos up to $Z = 108$". *Zeit. fr Phys.*, **232**:101–107, 1970.

[77] Taïeb R., Veniard V., and Maquet A. "Photoelectron Spectra from Multiple Ionization of Atoms in Ultra-Intense Laser Pulses". *Phys. Rev. Lett.*, **87**:053002, 2001.

[78] B.H. Brandsen and C.J. Joachain. *"Physics of atoms and molecules"*. Longman Scientific and Technical, 1983.

[79] Becker T. and Rinkleff R.H. "Superfluorescent transitions between high-lying levels in an external electric field". *Phys. Rev. A*, **44**:1806?1816, (1991).

[80] Kornev A.S., Tulenko E.B., and Zon A.B. "Kinetics of Multiple Ionization of Rare-Gas Atoms in a Circularly Polarized Laser Field". *Phys. Rev. A*, **68**:043414, 2003.

[81] C.F.Fischer and M. Saparov. Hartree-fock applet. http://atoms.vuse.vanderbilt.edu/hf.html, 1997.

[82] R. D. Cowan. *"The Theory of Atomic Structure and Spectra"*. University of California Press, Berkley and Los Angeles, 1981.

Publications in the frame of this research

- E. Gubbini,U. Eichmann, M.P. Kalashnikov and W. Sandner *Core Relaxation in Atomic Ultra Strong Laser Field Ionization*
  Phys. Rev Lett. **94** 053602 (2005)

- E. Gubbini,U. Eichmann, M.P. Kalashnikov and W. Sandner *"Strong laser field ionization of Kr: First order relativistic effects defeat rescattering*
  J. Phys. B: At. Mol. Opt. Phys. **38** (2005) L87-L93

- E. Gubbini, G. Kommol, M. Schnürer, H. Schönagel, U. Eichmann, M.P. Kalashnikov, P.V. Nickles, F. Eggenstein, G. Reichardt, W. Sandner *"On-line" cleaning of optical components in a multi-TW-Ti:Sa laser system*
  Vacuum **76** (2004) 45-49

Thanks

I would like to thank Prof. Dr. W. Sandner for the possibility he gave me to perform the experiments with the high-field laser facility at the Max-Born-Institute and to participate in international conferences. Not forgetting his willingness to have in interesting and helpful discussions, not only about the specific matter of this work, but also about general physics topics.

Dr. U. Eichmann, I thank for the discussions and corrections which led to the publications of the results.

I would like to thank Prof. Dr. G. Von Oppen and Prof. Dr. E. Sedlmayr for their disposition to evaluate and to

A particular thank you goes to Dr. Schnürer and Dr. Ter-Avetisyan for their support during the development of the set-up and the copious suggestions which have strongly helped in the success of the experiment.

My colleagues, Katia Eremina and Dr. Xiaojung Liu, I would like to thank for the helpful discussions which contributed to throw light on theoretical questions concerning the interpretation of the results.

Prof. Agostini I would like to thank for his suggestions and his help in correcting this work as well as for his support before and during the conference in Palermo. I appreciate it very much.

To all the technicians working in Bereich B, in particular Gerd Kommol, Jürgen Meißner, Jens Glaesel and Rainer Hoffmann, my deep gratitude for their infinte disposition to help me in the practical work of the laboratory.

A huge thank you is directed to Stephan who has shown enormous patience in "succoring" me every time I needed help and to stand by me in mounting complicated vacuum components. Of course, I am in his debt not only for his physical but also emotional support, love and understanding.

To Stephan G. goes all my thanks for his patience in supporting me for computer problems and to Henrik for his help in the solving of several problematics connected with simulations.

Last, but not least, I would like to thank Chris, Bernd and Dr. Gerd Priebe for their moral encouragement during these four years.